Optical Second Harmonic Generation from V-Shaped Chromium Nanohole Arrays

NGO KHOA QUANG

Japan Advanced Institute of Science and Technology

Doctoral Dissertation

Optical Second Harmonic Generation from V-Shaped Chromium Nanohole Arrays

NGO KHOA QUANG

Supervisor: Professor Dr. Goro Mizutani

School of Materials Science
Japan Advanced Institute of Science and Technology

September 2014

Acknowledgements

Coming JAIST as an absolute beginner in nonlinear optics, I have been taught for three years under the supervision of Professor Goro Mizutani. He gave me the great chance to be a member of Mizutani laboratory and investigate many intriguing effects in the world of optical second harmonic generation. From him, I have learned many skills to write, explain, and convince what I think. During discussion time, my knowledge has been gained very much and many problems I did not know previously have been elucidated. Especially, my English ability is going to be better through his English course. Without his helps and advices, I could not be able to finalize my goals. Foremost, I am profoundly grateful for all unceasing supports that my supervisor has done.

I would like to thank Professor Harvey Rutt who has made a "bridge" for the collaboration between Mizutani laboratory, JAIST and research group in University of Southampton. I would like to express my gratitude for all his effort during sample fabrication process. Additionally, I would like to express my gratitude to my co-workers in University of Southampton, Dr. Charlton, Dr. Chen, and Dr. Boden because of their much effort in helping me. Without their support, most of my experiments were impossible. I have many thanks to Dr. Yoshihiro Miyauchi who has encouraged and given me valuable advices during my studying in JAIST.

I would like to thank my committee members, Professor Hiroshi Mizuta, Associate Professor Mikio Koyano, and Associate Professor Hidekazu Tsutsui. I would like to thank Professor Takeshi Inaoka for judging as my outside committee member.

In addition to all peoples mentioned above, I would like to thank Dr. Khuat Thi Thu Hien for her careful reading of the manuscript and beneficial advices. She has supported me in various ways throughout the period of last 5 months in JAIST. I would like to thank the Vietnamese Government for the 322 scholarship program. I also thank my Japanese friends in Mizutani laboratory. They kindly help me to deal with many procedures that I do not know.

Finally, I am most grateful to my parents in Vietnam for all they have done. Their support and love raise me up to build all my successes. I really appreciate my little wife who gives the encouragement when I was discouraged.

Abstract

In this thesis, analytical approach of local surface contribution (electric dipole) and nonlocal bulk contribution (magnetic dipole and electric quadrupole) of chromium metal was presented by examining the nonlinear optical response of V-shaped nanohole arrays. The optical second harmonic generation data achieved in this work would give raise to the intriguing phenomenon of metamaterial. Additionally, controlling the optical behavior of Cr nanostructures will make a significant impression for optical device application.

In the field of plasmonics, gold or silver was widely adopted as the substrate material because they are favorable for surface plasmon resonance (SPR) where the electromagnetic waves could be confined to propagate along the interface between two media. Since these metals have very poor adhesion, chromium is usually employed as a reliable adhesion layer before depositing Au or Ag thin film and shaping the structures. Nevertheless, according to my calculation, plasmon excitation of Cr is possible and more feasible compared with part of the other metals. Indeed, A. Shalabney et al. found surface plasmon resonance in Cr columnar thin film in the Kretschmann configuration. In addition, to avoid SPR's loss, a very thin and uniform film is required and Cr is the best material. Thus, Cr would be a promising material in research field of plasmonics if one optimizes the activity in plasmon excitation. Because of its importance to plasmonics it is very necessary to address the optical behavior of Cr. Within this aim, the goal of my work is considering the optical response of Cr metal in nanoscale.

There are various approaches used to reveal the optical properties of metallic nanostructure. Among these, surface second harmonic generation (SHG) method has become a potential technique, which is very sensitive to the structures lacking inversion symmetry. Thus, V-shaped Cr nanoholes should generate strong SHG intensity. The nonlinear optical response should be recognized in the obtained second order nonlinear susceptibility tensor elements. From second order optical standpoint, plasmonics has been expected to improve the nonlinear efficiency as well as shrink the nonlinear components in size. Noticeably, the recent reports researched on the second order optical effects in plasmonic structures have emphasized that metal materials give rise to a very complicated state, especially at nanoscale. Both surface (electric dipole) and bulk (magnetic dipole and electric quadrupole) contributions can appear equally in the SHG magnitude whereas the surface term is usually considered as feasible candidate. Up to now, examination of dipole and multipoles terms in the geometric nanostructrues is still the significant challenge of second order optical effects. Thus, clarifying the role of the local surface and nonlocal bulk contribution becomes particularly necessary to control and optimize the nonlinear optical behavior of the metallic nanostructures for the functional applications. Furthermore, as far as I know there is no information available on surface second harmonic generation of Cr metal. Hence, in my work, the attention was paid on the proper estimation between dipole and multipole effects in V-shaped Cr nanohole structure. The new information could contribute to well understanding of nonlinear optical effects occurring in artificial materials.

In this research, I have fabricated the arrays of V-shaped nanoholes by JEOL JBX-9300FS Electron Beam Lithography System and measured the azimuthal angle dependence of the SHG intensity. The phenomenological analysis indicated that four nonlinear susceptibility elements including $\chi^{(2)}_{313}$, $\chi^{(2)}_{322}$, $\chi^{(2)}_{311}$, and $\chi^{(2)}_{333}$ present the predominant contribution. Here 1-axis presents the bisector of the V shape passing through its apex in the sample surface plane. 2-axis is perpendicular to 1-axis and lies on the sample surface too. 3-axis is normal to the sample surface plane. As for the origins of $\chi^{(2)}_{311}$, $\chi^{(2)}_{322}$, and $\chi^{(2)}_{333}$ elements, it is impossible to distinguish between the

contribution of the V-shaped Cr nanoholes and the bare Cr substrate since these two susceptibility elements appear simultaneously under C_s (V-shaped hole) and C_∞ (bare Cr substrate) symmetries. On the other hand, the contribution of the nonlinear susceptibility element $\chi^{(2)}_{313}$ should be purely from the nanoholes because it emerges owing to the symmetry breaking in 1-axis created by the V-shaped nanoholes. For favorable material exploited for artificial nanostructures such as gold, plasmon exciation enhancing nonlinear optical effect could be accomplished. However, in the case of Cr metal plasmon was silent when I examined the physical origin of the large contribution of the $\chi^{(2)}_{313}$ element. Interestingly, the observed SHG response was attributed to the nonlocal bulk contribution of the Cr metal. Under scrutiny, there are vertical metallic sidewalls within each V-shaped hole leading to existence of air-chromium metal boundaries. This has a strong effect on the field gradient in 1-axis because of the rate of spatial change of the field at the boundary of the nanohole surface. The field gradient were thus found to induce considerable contribution of $\chi^{(2)}_{313}$. In particular, instead of local surface contribution (electric dipole effect), nonlocal bulk contribution (higher multipole effects) demonstrated predominance with respect to the SHG signal. It is fascinating insight of the V-shaped Cr nanohole arrays since local surface contribution is usually the feasible candidate. My achievement implies the fact that the nonlinear optical behavior of the metamaterials should not be merely treated by usual electric dipole approximation because it is not sufficient to provide the comprehensive description. In metal nanostructures, there is an inherent complication since the reflected SHG signal generally contains both surface and volume nonlinear contributions. The difficulty in estimating electric dipole and the precise role of higher multipole effects is the issue lasting for long time from the early stages of nonlinear optics and still under intriguing process of examination. Therefore, the proper estimation between surface and bulk effects in my work is particularly essential to improve the understanding of the nonlinear optical response of metal nanostructures and metamaterials.

In a further work, I have attempted to examine the dependence of the SHG response on the structural parameters of V-shaped chromium nanoholes. It is expected to understand the origin of the SHG in problem if we consider how the SHG intensity alters when the arm length and the apex angle are changed. Thus, three sets of the V-shaped nanoholes were fabricated and their SHG intensities in the azimuthal angle dependence were compared with each other. In particular, SHG intensity created by individual V shape increased when the arm length or the apex angle increased. A simple model calculation was presented to deduce the experimental results. It provided valuable insight that there was a systematic dependence of the SHG intensity on the designed parameters of Cr nanoholes. The clarification shows that the nonlinear optical behavior was resulted from the bulk contribution of metallic electrons. This work therefore provides the new information in adjustment of the nonlinear optical behavior of metamaterial for functional applications.

Keywords: Second harmonic generation (SHG); Cr metal; Nanoholes; V-shaped structure; bulk contribution.

TABLE OF CONTENTS

CHAPTER 1

INTRODUCTION

1.1. Background

1.1.1. Interaction between light and nanoscale objects

Nowadays, the well-developed instrumental devices allow us to observe the natural world in more detail. There are many ways to characterize the objects based on the expected application. In the optical approaches, the objects' behaviors are considered by interpretation of the effects associated with light [1]. The estimated results therefore support researchers to construct the physical laws describing the target. Most interestingly, when the objects go down to small size the attractive features appear and promote the scientists to model them [2]. From the optical point of view, we are now discussing the structures significantly smaller than the wavelength and several essential features will occur in this region. For instance, in the case of insulator the light scattering owning to the Rayleigh law proposes that the scattering intensity is inversely proportional to the wavelength (see Fig. 1.1) [3]. Therefore, the shorter the wavelength is, the much stronger of scattering intensity will be. In the case of semiconductor, the most interesting effect is

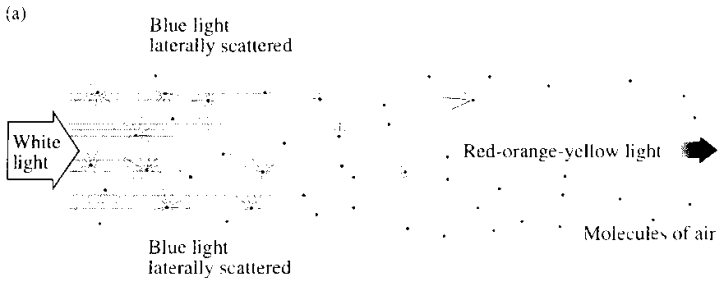

Fig. 1.1. Sunlight traversing a region of widely spaced air molecules. The light laterally scattered is mostly blue, and that is why the sky is blue. The unscattered light, which is rich in red, is viewed only when the Sun is low in the sky at sunrise and sunset [3].

the size-dependent bandgap (see Fig. 1.2). By altering the size of the semiconductor, we principally modify the emission wavelength [4,5]. The photoluminescence (PL) spectra of

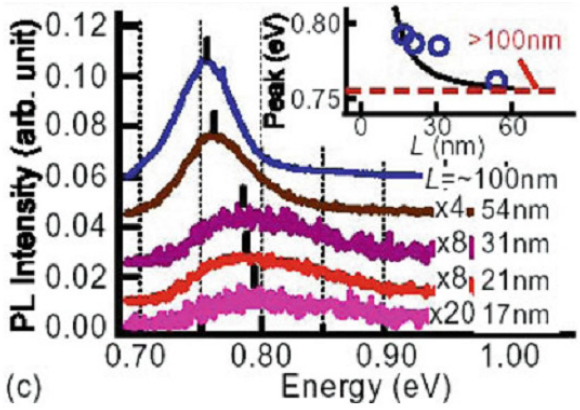

Fig. 1.2. Photoluminescence (PL) spectra of the GaSb nanodots with average nanodot radius L of 17, 21, 31, 54 nm. The inset shows the size dependence of the PL peak positions (open circles) and a theoretical curve (solid line) [5].

the nanodots were shown in Fig. 1.2. The relation between the peak position and average nanodot radius L shows the PL peak blue-shifted with the decrease of the nanodot size [5]. These are how insulator and semiconductor nanostructures fundamentally exhibit [4,6]. If we consider the metallic nanostructures, many fascinating phenomena not directly observed in nature will appear [7].

In principle, if an external light field impinges on a metallic nanostructure collective oscillations of the quasi-free conduction electrons are excited. The specific resonances associated with surface plasmon will appear and these frequencies originate from the interplay of electron density oscillations and the external electric field [8]. Once the light frequency couples with the frequency of collective oscillations of the conduction electrons, plasmon resonance occurs and results in strong electric field enhancement as shown in Fig. 1.3. This could lead to very high density of electric field lines in certain region on the metal surface, called “hot spot” [9]. Hot spots can occur at the specific zones where geometric confinement of the field lines is established. That key point could be applied in surface-enhanced Raman scattering [9,10] or nonlinear interaction processes [11].

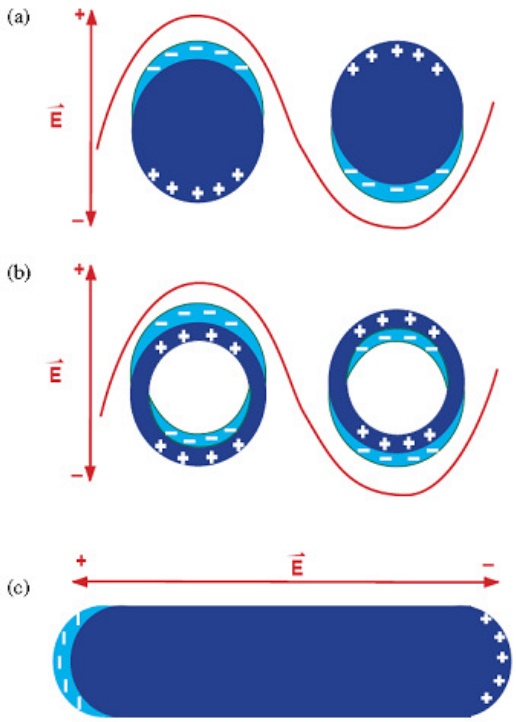

Fig. 1.3. Schematic illustration of dipolar surface plasmon resonance in spherical nanoparticles (a), core/shell structures (b), and nanorods (c) in a polarized light field. For the nanorod, only the longitudinal mode is shown. The transverse mode is essentially the same as in spherical nanoparticles. The lower the symmetry of the structure, the more nondegenerate modes there are. Both the solid spherical nanoparticles and hollow nanospheres have one resonance due to high symmetry. The nanorods with one symmetry axis have two nondegenerate modes (only one, the longitudinal mode, is shown). Complex structures such as strongly aggregated nanoparticles typically have multiple nondegenerate dipole modes, resulting in broad plasmon absorption spectra [6].

1.1.2. The inventions in nanoscience

Together with the development of the fabrication technology [12] scientists have opportunities to design as well as investigate unusual characteristics of metallic structures in nanoscale [13,14,15,16]. There are many promising applications. The localized surface

on plasmon

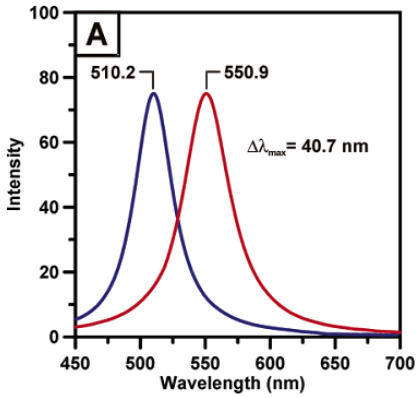

Fig. 1.4. Individual Ag nanoparticle before and after modification with 1-HDT [17].

nanoparticles can be used for chemical and biosensing applications. It was found that a fewer 1-hexadecanthiol molecules (HDT) can be detected by considering the wavelength shift of the surface plasmon resonance as shown in Fig. 1.4 [17]. More recently, pioneering work done by N. Liu et al. proved the possibility in detecting single particle level using antenna nanostructure consisting of Pd and Au [18]. Figure 1.5 presents a schematic representation of antenna-enhanced single-particle hydrogen sensing. If we could control the optical properties of the materials (negative permittivity materials), we can also make things "invisible" or create the "superlens", not limited by the diffraction condition [13,19]. With their attempts, Yu et al. [20] and Ni et al. [21] experimentally showed an unconventional effect bending the light along the wavefront by deliberately choosing an array of V-shaped gold nanostructure at different angles of apex with a periodicity of Λ as shown in Fig. 1.6. Here, the V-shaped Au arrays were fabricated on a double-sided polished silicon substrate with standard electron-beam lithography. Both experimental and theoretical results indicate that the reflection and refraction of light are both "negative" [21]. Their works could be applied to make ultrathin lenses. I can find that these works associate with "plasmonics" where light could be confined in the scale down to subwavelength [4].

The development of nanotechnology gives many advantages, but it also presses researchers to find suitable nanoscale devices, overcoming the limitations of conventional physical laws. Especially, for the computing devices with high density and speed as microprocessors, the problem becomes very crucial [22,23]. Figure 1.7 shows the operating speeds and critical dimensions of various chip-scale device technologies. With

the electronics, nowadays the devices can be downed to nanoscale and the best transistor is about 10nm [23]. Nevertheless, the electronics is limited in terms of the rate because of the delay of the interconnection and it limits the speed of digital circuit [24], roughly by GHz [25]. If we perceive the photonics it is seemingly faster, in THz [25]. Unfortunately, they are not small enough to integrate the components into electronic chips of nanometer because the size is normally required to be comparable or larger than the wavelength in order to guide the light. Therefore, the size of photonic devices is in microscale and plasmonics is the hopeful. In the side of plasmonics, we could say plasmonics as fast as photonics and as small as electronics. Plasmonics seem to be the mixture between the photonics and electronics. This is actually what the surface plasmon polariton means because it is the coherent mixture of electron excitation and photon. I could summarize that plasmonics is the solution of future expectation as it combines the advantage of characterizations of electronic and photonic devices [25].

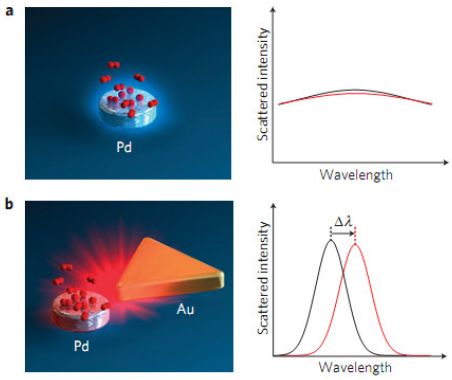

Fig. 1.5. Schematic representation of antenna-enhanced single-particle hydrogen sensing. a, Hydrogen sensing with a single palladium nanoparticle. Hydrogen molecules and adsorbed hydrogen atoms are shown in red. The palladium nanoparticle scatters weakly, showing an extremely damped and broad spectrum. The palladium particle alone causes a barely detectable change on hydrogen exposure. b, Hydrogen sensing using a resonant antenna-enhanced scheme. The same palladium nanoparticle is placed at the nanofocus of a gold antenna, which scatters much more strongly. Hydrogen absorption on the palladium particle changes its complex dielectric function, which causes a resonance shift ($\Delta\lambda$) of the gold antenna that can be optically detected [18].

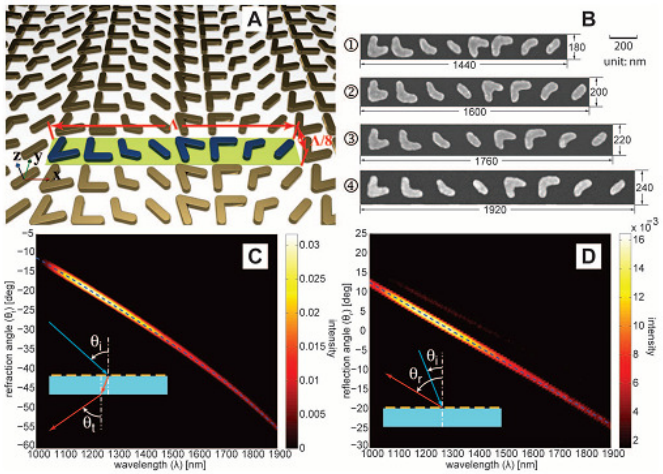

Fig. 1.6. (A) Schematic view of a representative antenna array. The unit cell of the plasmonic interface (in blue) consists of eight gold V-antennas of 40-nm arm width and 30-nm thickness, repeated with a periodicity of L in the x direction and Λ/8 in the y direction. The phase delay for cross-polarized light increases along the x axis from right to left. (B) Scanning electron microscope images of the unit cells of four antenna arrays with different periodicities fabricated on a single silicon wafer. (C and D) The false-color maps indicate the experimentally measured relative intensity profiles for the antenna array labeled ① [in (B), Λ=1440nm] with x-polarized excitation. The dashed line shows the theoretical prediction of the peak position using the generalized Snell's law. (C) Refraction angle θ_t versus wavelength λ for cross-polarized light with 30° incidence angle θ_i. (D) Reflection angle θ_r versus wavelength for cross-polarized light with 65° incidence angle [21].

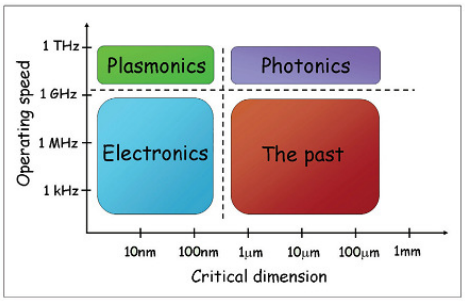

Fig. 1.7. Operating speeds and critical dimensions of various chip-scale device technologies, highlighting the strengths of the different technologies [25].

1.2. Objective of this thesis

As regarded so far, with the advantaged fabrication technology, one can design the deliberated geometries to utilize the surprising behaviors of metamaterial to create expected effects such as negative refractive index [26], local field enhancement [27], or plasmon excitation [28]. For the plasmon excitation, Au and Ag are two well-known plasmonic materials [29,30]. Chromium is usually employed as an adhesion layer before depositing a gold or silver thin film and shaping the structures. However, my consideration shows that the damping of the surface plasmon wave propagating along air-Cr metal interface is negligible for wavelengths from 400 nm to 1200 nm, meaning that Cr is also supposed to exhibit surface plasmon resonance. Indeed, Shalabney et al. found surface plasmon resonance in Cr columnar thin film in the Kretschmann configuration [31]. It is noted that Cr metal has good adhesion to the substrate [32]. To avoid SPR's loss, a very thin and uniform film is required and Cr is the best material. Thus, Cr would be a promising material in research field of plasmonics if one improves the activity in plasmon excitation. Because of its importance to plasmonics it is very necessary to address the optical behavior of Cr. Within this aim, the goal of my work is considering the nonlinear optical response of Cr metal in nanoscale.

There are various approaches used to reveal the optical properties of metallic nanostructure. Among these, surface second harmonic generation (SHG) method has become a potential technique, which is very sensitive to the structures lacking inversion symmetry. Thus, V-shaped Cr nanoholes should generate strong SHG intensity. The nonlinear optical response should be recognized in the obtained second order nonlinear susceptibility tensor elements. From second order optical standpoint, plasmonics has been expected to improve the nonlinear efficiency as well as shrink the nonlinear components in size. Noticeably, the recent reports studied about the second order optical effects in plasmonic structures have emphasized that metal materials give rise to a very complicated state, especially at nanoscale. Both surface (electric dipole) and bulk (magnetic dipole and electric quadrupole) contributions can appear equally in the SHG magnitude whereas the surface term is usually considered as feasible candidate. Up to now, examination of dipole and multipole terms in the geometric nanostructrues is still the significant challenge of second order optical effects. Thus, clarifying the role of the local surface and nonlocal bulk

contribution becomes particularly necessary to control and optimize the nonlinear optical behavior of the metallic nanostructures for the functional applications. Furthermore, as far as I know there is no information available on surface second harmonic generation of Cr metal. Hence, in my work, the attention was paid on the proper estimation between dipole and multipole effects in V-shaped Cr nanohole structure. The new information could contribute to well understanding of nonlinear optical effects occurring in artificial materials.

In my study, I investigated the nonlinear susceptibility properties of V-shaped subwavelength slits formed into a 15 nm thick chromium film fabricated by electron beam lithography. I measured the azimuthal angular dependence of the SHG signal from the sample for different input and output polarization combinations. Surface and volume nonlinear contributions will be argued based on the decomposed nonlinear susceptibility element $\chi_{313}^{(2)}$. Here 1-axis presents the bisector of the V shape passing through its apex in the sample surface plane. 2-axis is perpendicular to 1-axis and lies on the sample surface too. 3-axis is normal to the sample surface plane. I will discuss whether the SHG signal reflects the electric dipole or the precise role of higher multipole effects by examining all possible original candidates.

1.3. Outline of the thesis

Six chapters in the thesis are organized as follows,

Chapter 1 figures out how I was approaching the problem in this study. Here, I briefly introduce the advantage of the plasmonic structures, the objective and the outline of the research.

Chapter 2 summarizes the concepts about plasmon excitation as well as the way used to excite plasmon resonance. Furthermore, I present the classical model, free electron gas, described the nonlinear effects when shining the metal by strong incoming electric field. The origin of the nonlinearity sources is also discussed based on the responsible mechanism between surface and bulk contributions. SHG method used to probe metal surface is presented in detail. I further show how individual nonlinear susceptibility element would be extracted in order to investigate the role of dipole and multipole effects.

Chapter 3 reviews the pioneering works in nonlinear plasmonics done by the other groups after the preliminary theories concerning SHG was introduced in Chapter 2. Here, a list of shapes of metallic nanostructures, including nanoparticles and nanoapertures are considered. Local field enhancement, symmetry concept, size structure etc. were investigated to deduce the origin of nonlinear response in these studies. A short overview about electron beam lithography and Atomic Force Microscope (AFM) measurement are included since these techniques were used to make and observe the metallic structures in our study.

Chapter 4 mainly describes how sample was fabricated by electron beam lithography method. I explain the built-steps of experimental setup when azimuthal angle measurement was performed.

Chapter 5 shows the sample morphology via AFM observation. The results of surface SHG measurement are discussed owing to the theoretical analysis. A phenomenological model is used to solve the SHG response from V-shaped Cr nanohole arrays. To consider how the SHG intensity alters when the arm length and apex angle are changed, a simple model calculation is presented to deduce the experimental results.

Chapter 6 summaries the main achievement of the research and predicted the future plan when changing the studied systems.

CHAPTER 2

THEORETICAL BACKGROUND

2.1. Maxwell's equations

I begin this chapter by reviewing the Maxwell's equations. These equations briefly present how light and matters interact to each other. They are very important with electromagnetic theory. Following four equations could be used to figure out how the real physic phenomena actually occur [33],

$$\nabla \times \vec{E} + \frac{\partial \vec{B}}{\partial t} = 0 \tag{1}$$

$$\nabla \times \vec{H} - \frac{\partial \vec{D}}{\partial t} = \vec{j} \tag{2}$$

$$\nabla . \vec{D} = \rho \tag{3}$$

$$\nabla . \vec{B} = 0 \tag{4}$$

where $\vec{E}$ and $\vec{B}$ are the electric vector and magnetic induction, respectively. $\vec{D}$ and $\vec{H}$ are the electric displacement and magnetic vector. ρ and $\vec{j}$ are the free electric charge and current density, respectively. For general use, the electric displacement is defined as follows,

$$\vec{D} = \varepsilon_0 \vec{E} + \vec{P} \tag{5}$$

where, ε_0 is the permittivity of the vacuum and $\vec{P}$ is the induced polarization (electric dipole moment per unit volume). In the case of the small values of electric field, we have a linear relation between $\vec{P}$ and $\vec{E}$,

$$\vec{P} = \varepsilon_0 \chi \vec{E} \tag{6}$$

Equation (5) can be written as follows,

$$\vec{D} = \varepsilon_0 \vec{E} + \vec{P} = \varepsilon_0 \vec{E} + \varepsilon_0 \chi \vec{E} = (1 + \chi)\varepsilon_0 \vec{E} = \varepsilon \varepsilon_0 \vec{E} \tag{7}$$

Here, χ is known as the linear susceptibility and related to the index of refraction by [4],

$$\chi = n^2 - 1$$

χ is expressed as a tensor to account for the variation in polarization response for different directions of the applied field. Especially, for larger power of the optical electric field, the

relationship between the applied electric field and material's response should not be treated as linearity. The induced polarization can be described by a series expansion as,

$$\vec{P} = \varepsilon_0 \chi^{(1)} \vec{E} + \varepsilon_0 \chi^{(2)} \vec{E}\vec{E} + \varepsilon_0 \chi^{(3)} \vec{E}\vec{E}\vec{E} + \cdots \quad (8)$$

Equation (8) indicates that the polarization makes a significant contribution to the nonlinear optical process. Here, $\chi^{(2)}$ acts as the second order nonlinear susceptibility element and it will be considered later in section 2.3.3.

2.2. Concept of plasmonics

2.2.1. Drude model

When we emphasize plasmonic optics, the most important in this consideration is the response of the free electrons under light excitation. In metal, the electrons are nearly free and the collective oscillations of free electrons in metal are called plasmon [8]. This type of excitation or movement is particular important for plasmonic material, especially at the scale down to nanometer. Let us consider very classical model usually used to present the dielectric function of metal owning to free electron gas, Drude model. Although it is very simple approach, the Drude model, however, allow us roughly know how the metal responses under electric field excitation [4].

Let us assume that a classical gas of non-interacting electrons is acted by the time harmonic incident electric field $\vec{E} = \overrightarrow{E_0} e^{-i\omega t}$. The equation expressing the movement of the electron is as following [8],

$$\ddot{x} + \Gamma \dot{x} = -\frac{e}{m} \overrightarrow{E_0} e^{-i\omega t} \quad (9)$$

where x, m, and e are the electron displacement, mass, and charge, respectively. Γ is the damping coefficient due to the electron collision rate. For low intensities of the electromagnetic wave, the electron vibrates with the same frequency as the oscillating electric field. I will therefore assume that the time dependence of the electron motion will be similar to that of the field, so that $\vec{x} = \vec{x}_0 e^{-i\omega t}$. Introducing this term into equation (9) gives,

$$(-i\omega)^2 \overrightarrow{x_0} e^{-i\omega t} + \Gamma(-i\omega) \overrightarrow{x_0} e^{-i\omega t} = -\frac{e}{m} \overrightarrow{E_0} e^{-i\omega t} \quad (10)$$

$$\therefore \overrightarrow{x_0} = \frac{e\overrightarrow{E_0}}{m(\omega^2 + i\Gamma\omega)} \tag{11}$$

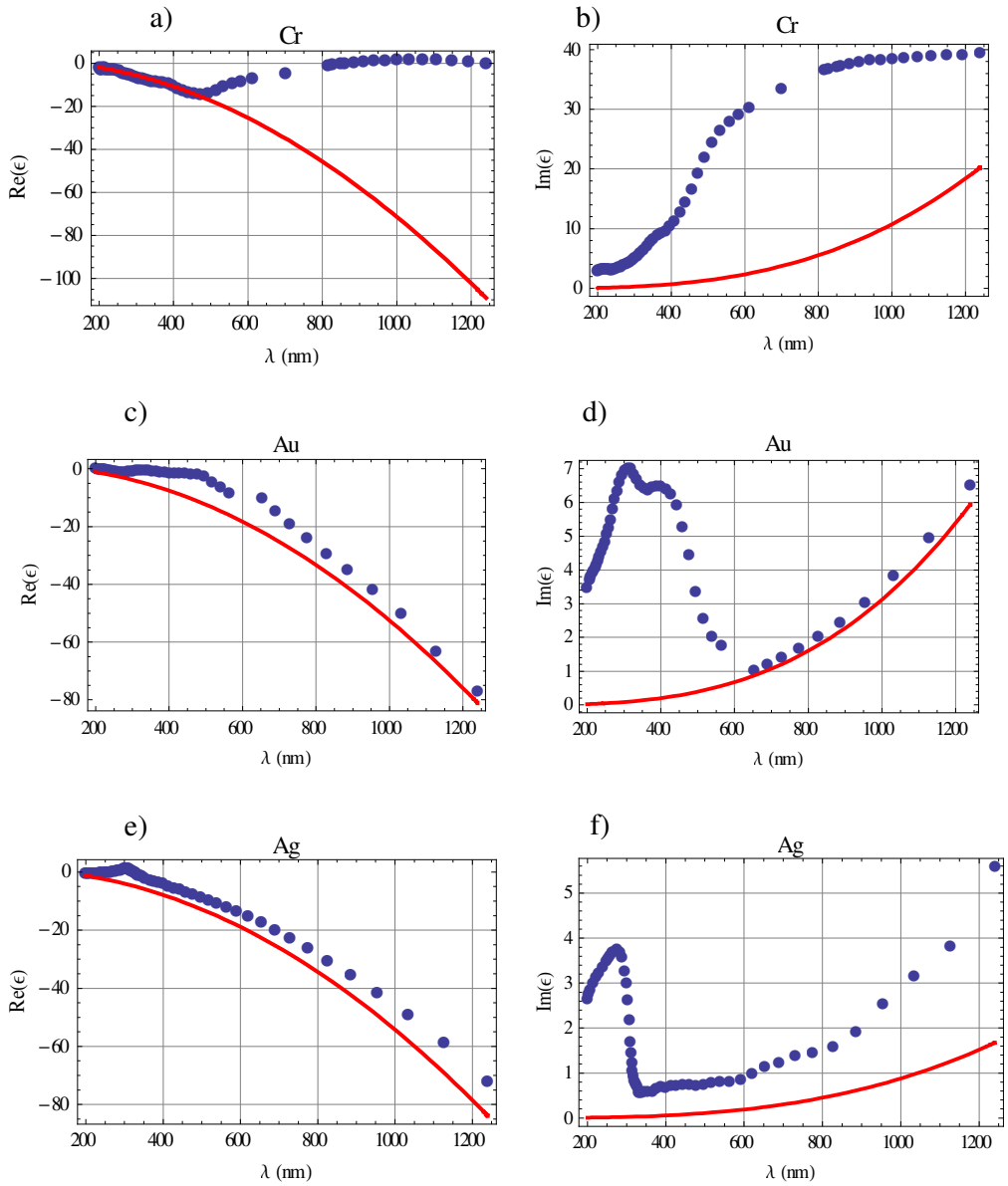

Fig. 2.1. Real and imaginary parts of the dielectric function for chromium (a-b), gold (c-d), and silver (e-f). The theoretical prediction (solid lines) were shown together with the experimental data (dotted line) taken from Parlik's handbook [35].

From the macroscopic point of view, the polarization $\vec{\mathrm{P}}$ can be expressed as,

$$\vec{\mathrm{P}} = -Ne\vec{x} = -Ne\left(\vec{x}_0 e^{-i\omega t}\right) = -Ne\frac{e\overrightarrow{E_0}}{m(\omega^2 + i\Gamma\omega)}e^{-i\omega t} = \frac{-Ne^2}{m(\omega^2 + i\Gamma\omega)}\vec{E} \qquad (12)$$

Here N is the number of charges displaced per unit volume. Together with equation (7) I have,

$$\varepsilon_0\vec{\mathrm{E}} + \frac{-Ne^2}{m(\omega^2 + i\Gamma\omega)}\vec{\mathrm{E}} = \varepsilon\varepsilon_0\vec{\mathrm{E}} \qquad (13)$$

$$\therefore \varepsilon = 1 - \left(\frac{Ne^2}{m\varepsilon_0}\right)\frac{1}{(\omega^2 + i\Gamma\omega)} = 1 - \frac{{\omega_p}^2}{(\omega^2 + i\Gamma\omega)}$$

with $\omega_p = \sqrt{\frac{Ne^2}{m\varepsilon_0}}$, called bulk plasma frequency.

The dielectric function can be separated into its real and imaginary components as follow,

$$\varepsilon = 1 - \frac{{\varpi_p}^2}{(\varpi^2 + i\Gamma\varpi)} = 1 - \frac{{\varpi_p}^2}{(\varpi^2 + \Gamma^2)} + i\frac{{\varpi_p}^2\Gamma}{\varpi(\varpi^2 + \Gamma^2)} = \varepsilon' + i\varepsilon'' \qquad (14)$$

where $\varepsilon' = 1 - \frac{{\varpi_p}^2}{(\varpi^2+\Gamma^2)}$ is the real part and $\varepsilon'' = \frac{{\varpi_p}^2\Gamma}{\varpi(\varpi^2+\Gamma^2)}$ is the imaginary part of the dielectric function.

The damping constant and the plasma frequency of Cr, Au and Ag are shown in Table 1.1. Here the damping constant of chromium metal was calculated through the Fermi velocity and electron mean free path [34]. In Fig. 2.1, I show the calculated dielectric function of several metals using Eq. (14) and the experimental data quoted from the Parlik's handbook [35].

Table 1.1. Damping constant and plasma frequency of several metals [34].

Metal	$\boldsymbol{\varpi_p}$ (s^{-1})	$\boldsymbol{\Gamma}$(s^{-1})
Chromium	1.62×10^{16}	0.28×10^{15}
Gold	1.38×10^{16}	0.11×10^{15}
Silver	1.40×10^{16}	0.03×10^{15}

2.2.2. Surface plasmon at metal-dielectric interfaces

The surface plasmon resonance (SPR) is defined as oscillation of the electron that occurs at the boundary between two media. The coupling of the electron oscillation with an electromagnetic field results in the optical wave confined at the surface. In this section, I

will consider the propagation of the electric field localized at the interface between metal and air. Visually, if a wave propagates along the interface, there must necessarily be a component of the electric field normal to the surface. Hence, S-polarized surface oscillations (the electric field E is parallel to the interface) do not exist. The solution therefore only exists for the case of P-polarized electric field [8].

I consider a P-polarized electric field at the interface of medium 1 (air) and medium 2 (metal) as depicted in Fig. 2. 2. P-polarized electric field in both half-spaces can be expressed as follows,

$$\vec{E}_i = \begin{pmatrix} E_{jx} \\ 0 \\ E_{jz} \end{pmatrix} e^{i(k_{jx}x - \varpi t)} e^{ik_{jz}z}, i = 1,2; \tag{15}$$

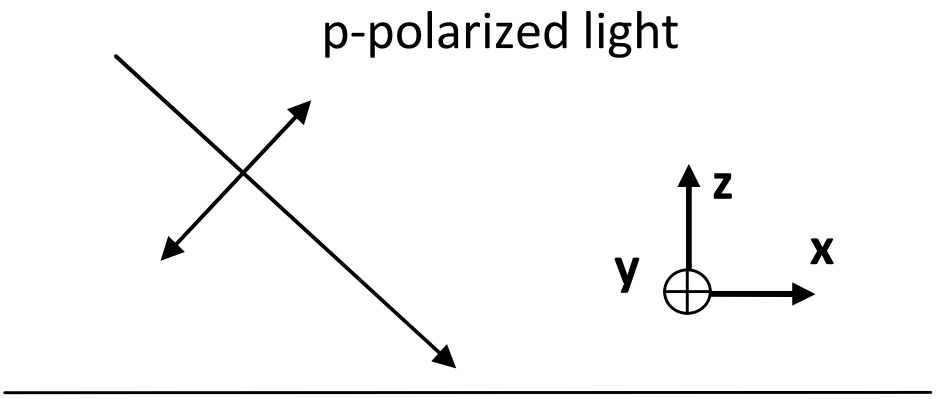

Fig. 2. 2. A P-polarized light impinges on the interface.

Boundary conditions requires that the tangential components of electric field and the normal component of the electric displacement on either side are continuous across a boundary, on other words,

$$E_{1x} = E_{2x}$$
$$\varepsilon_1 E_{1z} = \varepsilon_2 E_{2z} \tag{16}$$

In each half space, the conservation of the wave vector parallel to the interface [36] gives us,

$$k_{1x} = k_{2x}$$

$$k_i = \sqrt{\varepsilon_i}\frac{\omega}{c} \Longrightarrow {k_i}^2 = \varepsilon_i\left(\frac{\omega}{c}\right)^2 = {k_{ix}}^2 + {k_{iz}}^2 \tag{17}$$

$$\Longrightarrow {k_x}^2 + {k_{iz}}^2 = \varepsilon_i\left(\frac{\omega}{c}\right)^2 = \varepsilon_i k^2 \tag{18}$$

Together with Gauss' law shown in Eq. (3), I obtain the following relations for the wave vector k

$$\nabla.\vec{D} = 0$$

$$\Leftrightarrow \nabla.\left[\begin{pmatrix} E_{jx} \\ 0 \\ E_{jz} \end{pmatrix} e^{i(k_{jx}x-\omega t)} e^{ik_{jz}z}\right] = 0$$

$$\Leftrightarrow \left(ik_{jx}E_{jx} + ik_{jz}E_{jz}\right) e^{i(k_{jx}x-\omega t)} e^{ik_{jz}z} = 0$$

$$\Leftrightarrow k_x E_{ix} + k_{iz}E_{iz} = 0 \tag{19}$$

From now, I have a system of linear equations as,

$$\begin{cases} E_{1x} - E_{2x} + 0E_{1z} - 0E_{2z} = 0 \\ 0E_{1x} - 0E_{2x} + \varepsilon_1 E_{1z} - \varepsilon_2 E_{2z} = 0 \\ k_x E_{1x} + 0E_{2x} + k_{1z}E_{1z} + 0E_{2z} = 0 \\ 0E_{1x} + k_x E_{2x} + 0E_{1z} + k_{2z}E_{2z} = 0 \end{cases} \tag{20}$$

The existence of a solution for the system of linear equations mean that the determinant vanishes or

$$\begin{vmatrix} 1 & -1 & 0 & 0 \\ 0 & 0 & \varepsilon_1 & -\varepsilon_2 \\ k_x & 0 & k_{1z} & 0 \\ 0 & k_x & 0 & k_{2z} \end{vmatrix} = 0 \tag{21}$$

$$\Longrightarrow (\varepsilon_2 k_{1z} - \varepsilon_1 k_{2z})k_x = 0 \tag{22}$$

if $k_x = 0$ then there is no wave propagating along the interface, or

$$\varepsilon_2 k_{1z} - \varepsilon_1 k_{2z} = 0 \tag{23}$$

Together with equation (18) I have,

$$\begin{cases} {k_x}^2 + {k_{1z}}^2 = \varepsilon_1\left(\frac{\omega}{c}\right)^2 \\ {k_x}^2 + {k_{2z}}^2 = \varepsilon_2\left(\frac{\omega}{c}\right)^2 \\ {\varepsilon_2}^2{k_{1z}}^2 = {\varepsilon_1}^2{k_{2z}}^2 \end{cases}$$

$$\Longrightarrow {\varepsilon_2}^2\left[\varepsilon_1\left(\frac{\omega}{c}\right)^2 - {k_x}^2\right] = {\varepsilon_1}^2\left[\varepsilon_2\left(\frac{\omega}{c}\right)^2 - {k_x}^2\right]$$

$$\Rightarrow {k_x}^2 = \frac{{\varepsilon_1}^2\varepsilon_2\left(\frac{\omega}{c}\right)^2 - {\varepsilon_2}^2\varepsilon_1\left(\frac{\omega}{c}\right)^2}{{\varepsilon_1}^2 - {\varepsilon_2}^2} = \frac{\varepsilon_1\varepsilon_2}{\varepsilon_1 + \varepsilon_2}\left(\frac{\omega}{c}\right)^2 \quad (24)$$

I can evaluate the normal component of the wave vector

$${k_{iz}}^2 = \frac{{\varepsilon_i}^2}{\varepsilon_1 + \varepsilon_2}\left(\frac{\omega}{c}\right)^2 \quad (25)$$

I am going to discuss the existence of the surface plasmonic wave at the interface between air and metal. As pointed out in Eq. (14), in general, dielectric function of metal include the real part and imaginary part, or,

$$\varepsilon_2 = {\varepsilon_2}' + i{\varepsilon_2}'' \quad (26)$$

The parallel wavevector can be obtained as a complex number,

$$k_x = \left(\frac{\omega}{c}\right)\sqrt{\frac{\varepsilon_1\varepsilon_2}{\varepsilon_1 + \varepsilon_2}} = {k_x}' + i{k_x}'' \quad (27)$$

Introducing the result into Eq. (15) gives,

$$\vec{E_i} = \begin{pmatrix} E_{ix} \\ 0 \\ E_{iz} \end{pmatrix} e^{i[({k_x}' + i{k_x}'')x - \varpi t]} e^{ik_{iz}z} = \begin{pmatrix} E_{ix} \\ 0 \\ E_{iz} \end{pmatrix} e^{[(i{k_x}' x - {k_x}'')x - i\varpi t]} e^{ik_{iz}z} \quad (28)$$

Clearly, the real part ${k_x}'$ describes the surface plasmon wave while the imaginary ${k_x}''$ show the damping of the surface plasmon wave propagating along the x direction. To maintain the plasmon wave, the imaginary part ${k_x}''$ of materials supporting plasmon resonance should have small value and it was described by a so-called "observability function". According to the criterion given by Sambles et al. [37] and D. Sarid and W. A. Challener [33], observability function is

$$f = \frac{{k_x}''}{k_0} = \mathrm{Im}\left(\sqrt{\frac{\varepsilon_1\varepsilon_2}{\varepsilon_1 + \varepsilon_2}}\right) < 0.1 \quad (29)$$

This condition usually occurs in the favorable material considered as a good plasmonic material. Figure 2.3 show the observability function f plotted as a function of wavelength for Cr, Au, and Ag. One can see that f has a very small value for Au and Ag for wavelength from 600 to 1200 nm. The experimental results as well as the theoretical calculation indicated the observation of the plasmon resonance peaks around this zone for a given Au and Ag nanostructures [28,38,39]. The observability function for Cr metal is somewhat larger than Au or Ag however, it is still smaller than 0.1 in the wavelength from

400 to 1200 nm. Cr is therefore supposed to exhibit surface plasmon resonance. Indeed, A. Shalabney et al. found surface plasmon resonance in Cr columnar thin films in the Kretschmann configuration [31].

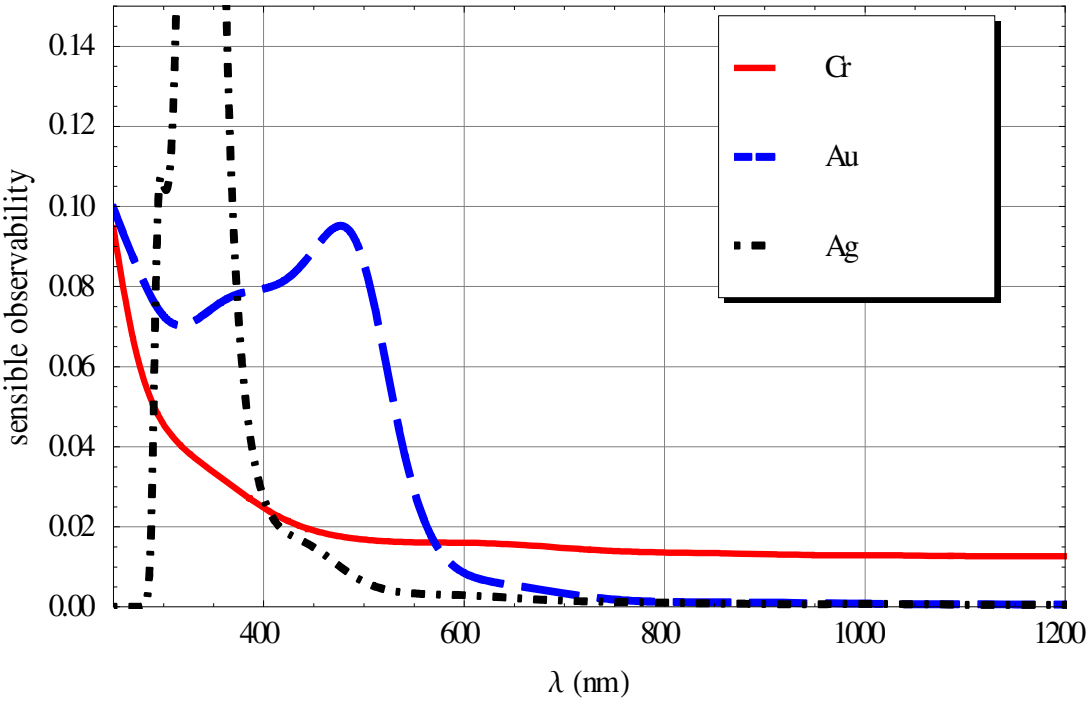

Fig. 2.3. The observability function f is plotted as a function of wavelength for Cr, Au, and Ag.

2.2.3. Prism coupler

Generally, the wave vector of a surface plasmon at the interface between metal and dielectric does not match with that of the external coming light. Therefore, surface plasmon excitation could not be active if one simply hits the metal surface by incoming light. In order match these two wave vector components for surface plasmon resonance, we have to exploit some special methods [40]. Normally, prism or grating coupler is employed to achieve the phase matching between the surface plasmon wave and excitation wave.

Let us consider the first method used to excite plasmon wave. An excitation wave propagates in air and impinges on the metallic surface with an incidence angle θ as shown in Fig.2.4 (a). The component of the wave vector parallel to the interface is

$$k_x = \frac{\omega}{c}\sin\theta \tag{30}$$

On the other hand, the angular frequency will be,

$$\omega = \frac{k_x c}{\sin\theta} \tag{31}$$

If another medium having optical index n>1 replaces air (see Fig. 2.4(b)). The equation (31) will be,

$$\omega = \frac{k_x c}{n\sin\theta} \tag{32}$$

Together with Eq. (27), the angular frequency of the surface plasmon wave at the interface between air and metal will be,

$$\varpi = k_x c\sqrt{\frac{\varepsilon_1 + \varepsilon_2}{\varepsilon_1 \varepsilon_2}} \tag{33}$$

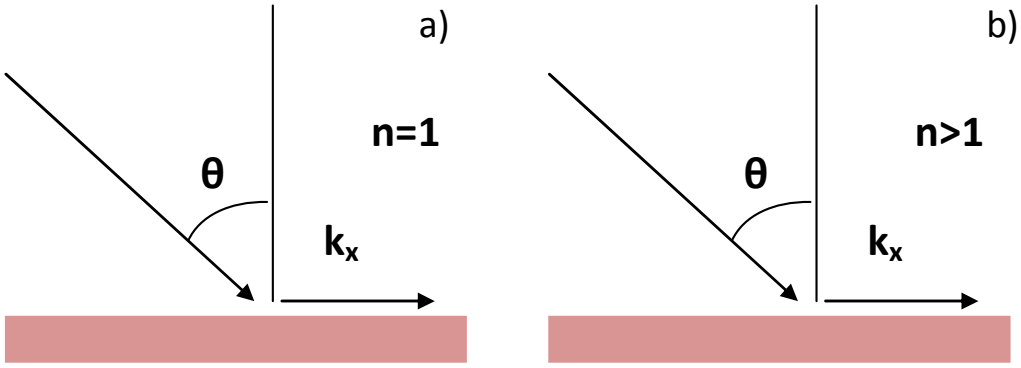

Fig. 2.4. Excitation of the surface plasmon wave: An external wave impinges on the metallic surface after propagating (a) in air or (b) glass.

The plot of the angular frequency ω as a function of the wave vector shown in Fig. 2.5 is the best way to visualize how the phase matching condition will be fulfilled [41]. Figure 2.5 shows the angular frequency ω as a function of the wave vector at the Cr metal-air

interface. Green line indicates the angular frequency of the wave vector in air (Eq. (31)). The dashed and blue lines indicate the angular frequency of the surface wave when I combine Eqs. (14) and (33). The red line plots the experiment data quoted from Palik's handbook [35]. One can see that plasmon excitation will occur if the free wave (green line) couple (cut) with the surface wave. If the external wave propagates in a medium with n > 1, a factor of n will be introduced as shown in Eq. (32). Therefore, the slope of the light line will be lower and cut the other lines. The coupling is then possible between incident light and plasmon wave. By introducing the prism, one can shift the wave vector of coming photon –"light line" toward that of the surface plasmon wave. This method is called Kretschmann configuration.

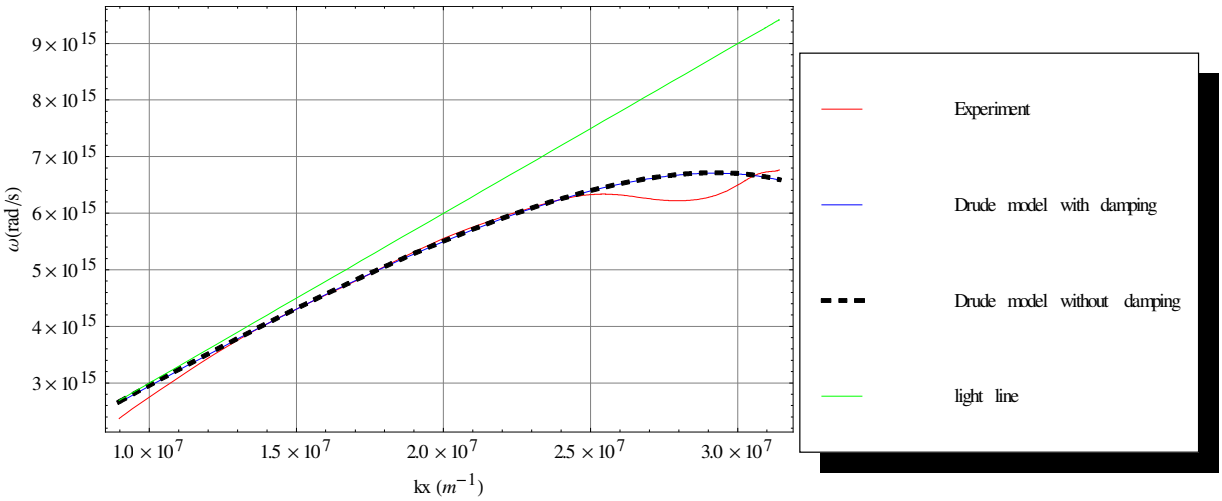

Fig. 2.5. The plot of angular frequency as a function of the wave vector. Green line indicates the angular frequency of a wave vector in air. The dashed and blue lines indicate the angular frequency of the surface plasmon wave by using equation (14) and (33). The red line plot the experiment data quoted from Palik's handbook [35].

2.2.4. Grating coupler

Grating coupler is another way to match the wave vector of the incident photon to that of the surface plasmon wave. As mentioned above, on a smooth metallic surface,

surface plasmon wave could not be directly excited by light owning to the momentum mismatch. To achieve this goal, one can also reconstruct the metallic surface. In the simplest case, a grating is suitable as illustrated in Fig. 2.6. By making the grooves lying along x direction, we expect to supply the necessary momentum to an incident photon when exciting a surface plasmon wave.

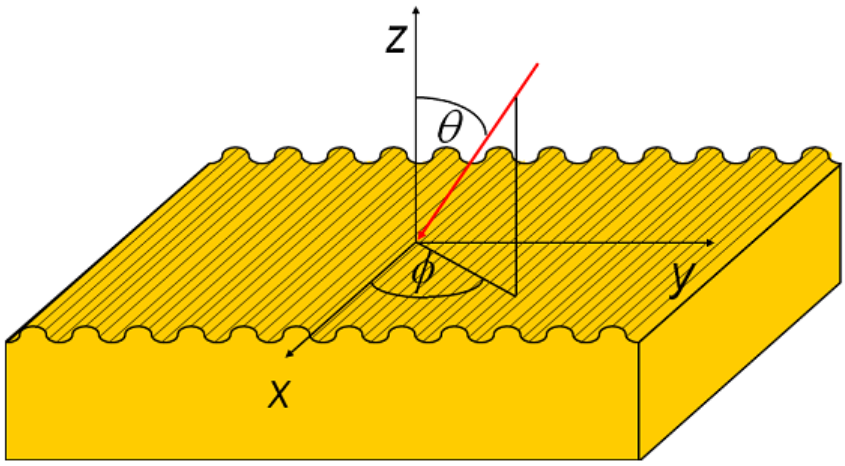

Fig. 2.6. A plane wave is incident onto a diffraction grating at a polar angle θ and an azimuthal angle ϕ with respect to the coordinate system. The grooves are parallel to the x-direction [33].

Here, I follow the calculation as in Ref. [33]. The grating vector is

$$\vec{K} = \frac{2\pi}{d}\vec{y} \tag{34}$$

Where d is the period of the grating and y is the unit vector. Conservation of momentum is obtained by setting the surface wave vector in Eq. (33) equal to the summation of the k vector's component of the incident photon lying on the surface plane and an integral multiple of the grating vector,

$$\begin{aligned}\left(\frac{\omega}{c}\right)\sqrt{\frac{\varepsilon_1\varepsilon_2}{\varepsilon_1+\varepsilon_2}}\vec{k}_{SP} &= \vec{k}_{incidence} + m\vec{K} \\ &= n_1\left(\frac{\omega}{c}\right)[(\sin\theta\cos\phi)\vec{x} + (\sin\theta\sin\phi)\vec{y}] + \frac{2\pi m}{d}\vec{y}\end{aligned} \tag{35}$$

$$\therefore n_1\left(\frac{\varpi}{c}\right)(\sin\theta\cos\phi)\vec{x}+\left[n_1\left(\frac{\varpi}{c}\right)(\sin\theta\sin\phi)+\frac{2\pi m}{d}\right]\vec{y}=\left(\frac{\varpi}{c}\right)\sqrt{\frac{\varepsilon_1\varepsilon_2}{\varepsilon_1+\varepsilon_2}}\vec{k}_{SP} \tag{36}$$

Where n_1 is the refractive index of the dielectric medium above the grating, ε_2 is the dielectric function of the metal, and m is an arbitrary integer. By talking the magnitude of both sides Eq. (36), I have,

$$\left[n_1\left(\frac{\varpi}{c}\right)(\sin\theta\cos\phi)\right]^2+\left[n_1\left(\frac{\varpi}{c}\right)(\sin\theta\sin\phi)\right]^2+2n_1\left(\frac{\varpi}{c}\right)(\sin\theta\sin\phi)\frac{2\pi m}{d}+\left(\frac{2\pi m}{d}\right)^2=\left(\frac{\varpi}{c}\right)^2\frac{\varepsilon_1\varepsilon_2}{\varepsilon_1+\varepsilon_2} \tag{37}$$

$$\therefore(n_1\sin\theta)^2+\frac{2n_1m\lambda_0\sin\theta\sin\phi}{d}+\left(\frac{\lambda_0 m}{d}\right)^2=\frac{\varepsilon_1\varepsilon_2}{\varepsilon_1+\varepsilon_2} \tag{38}$$

Here,

$$k_0=\frac{\varpi}{c}=\frac{2\pi}{\lambda_0} \tag{39}$$

Let us consider two interesting cases of Eq. (38). If the plan of the incident plane is perpendicular to the grooves of the grating, then $\phi=0$. I can easily obtain two solutions as follow,

$$\sin\theta=-\frac{m\lambda}{n_1 d}\pm\sqrt{\frac{\varepsilon'_2}{\varepsilon_1+\varepsilon'_2}} \tag{40}$$

For a sinusoidal grating, only m=1 generates a strong resonance effect. In another case, the incident plane is parallel to the groove $\phi=90^o$. Equation (38) becomes,

$$\sin\theta=\sqrt{\left(\frac{\varepsilon'_2}{\varepsilon_1+\varepsilon'_2}\right)-\left(\frac{m\lambda}{n_1 d}\right)^2} \tag{41}$$

Base on Eq. (40) and (41), I can roughly estimate the periodicity where the resonance will occur. Figure 2.7 (a) and (b) show the periodicity d as a function of the incident angle θ when I set $\lambda=532nm$

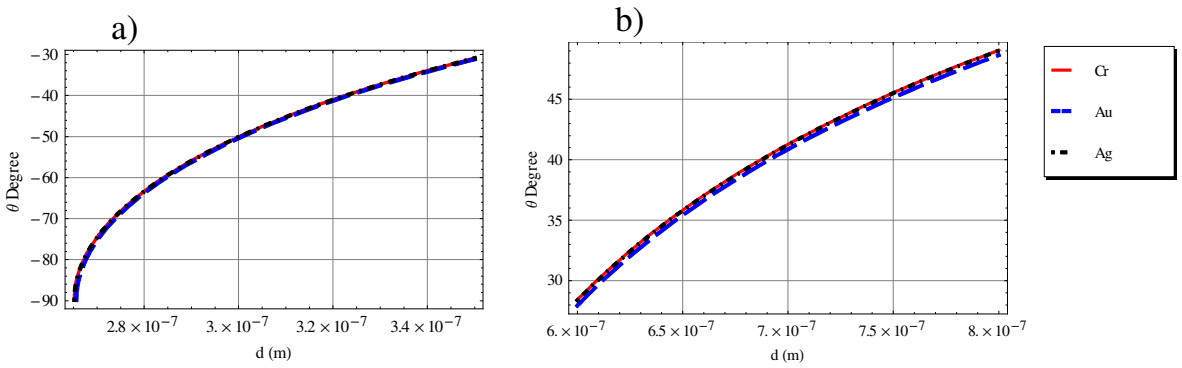

Fig. 2.7. The calculation of the incident angle as a function of periodicity. At the incident angle of 45°, the periodicities are 310.47nm and 743.05nm for the left and the right figures, respectively.

2.3. Nonlinear optics of plasmonic materials

2.3.1. Classical anharmonic oscillator model

Based on what has been interpreted so far, the response of material depends linearly on the applied electric field. However, when the field becomes strong enough the response will be nonlinear. To describe that effect from the classical point of view, let us expand the Drude model. The motion of an anharmonic oscillator can be modeled by following equation [42]

$$\ddot{x} + \Gamma\dot{x} + {\omega_0}^2 x + ax^2 = -\frac{e}{m}\left(\vec{E}_{01}e^{-i\omega_1 t} + \vec{E}_{02}e^{-i\omega_2 t}\right) \quad (42)$$

where ω_0 is the oscillation frequency of the electron, ax^2 acts as the nonlinear term with nonlinear coefficient a. To make it simpler, I assume that the movement of electron is driven by the optical electric field including only two frequencies ω_1 and ω_2. The solution of equation (42) can be obtained via the perturbation technique [42]. First, equation (42) will be solved by setting the nonlinear coefficient equal to zero,

$$\ddot{x} + \Gamma\dot{x} + {\omega_0}^2 x = -\frac{e}{m}\left(\vec{E}_{01}e^{-i\omega_1 t} + \vec{E}_{02}e^{-i\omega_2 t}\right) \quad (43)$$

The solution of equation (43) is called the zero-order approximate solution. Second, the zero-order solution is substituted into the nonlinear term of equation (42) to find the first-order term.

To obtain the zero-order term, I will find the solution of equation (43) as,

$$\vec{x}^0 = \vec{x}_{01}^0 e^{-i\omega_1 t} + \vec{x}_{02}^0 e^{-i\omega_2 t}$$

Substituting this equation and its derivatives into Eq.(43) I have,

$$[(-i\omega_1)^2 + \Gamma(-i\omega_1) + {\omega_0}^2]\vec{x}_{01} e^{-i\omega_1 t} + [(-i\omega_2)^2 + \Gamma(-i\omega_2) + {\omega_0}^2]\vec{x}_{02} e^{-i\varpi\omega_2 t} = -\frac{e}{m}\left(\vec{E}_{01} e^{-i\omega_1 t} + \vec{E}_{02} e^{-i\omega_2 t}\right) \quad (44)$$

Equating the coefficients on both sides of (44), I get,

$$\vec{x}_{01}^0 = -\frac{e\vec{E}_{01}}{m({\omega_0}^2 - {\omega_1}^2 - i\omega_1\Gamma)}$$

and

$$\vec{x}_{02}^0 = -\frac{e\vec{E}_{02}}{m({\omega_0}^2 - {\omega_2}^2 - i\omega_2\Gamma)}$$

Putting

$$\frac{1}{({\omega_0}^2 - {\omega_1}^2 - i\omega_1\Gamma)} = \alpha_1$$

and

$$\frac{1}{({\omega_0}^2 - {\omega_2}^2 - i\omega_2\Gamma)} = \alpha_2$$

I obtain the zero-order term as

$$\vec{x}^0 = -\frac{e}{m}\left(\alpha_1\vec{E}_{01} e^{-i\omega_1 t} + \alpha_2\vec{E}_{02} e^{-i\omega_2 t}\right) \quad (45)$$

Substituting (45) into equation (42) I get,

$$\ddot{x} + \Gamma\dot{x} + {\omega_0}^2 x = -\frac{e}{m}\left(\vec{E}_{01} e^{-i\omega_1 t} + \vec{E}_{02} e^{-i\omega_2 t}\right) - ax^2 \quad (46)$$

$$\leftrightarrow \ddot{x} + \Gamma\dot{x} + {\omega_0}^2 x = -\frac{e}{m}\left(\vec{E}_{01} e^{-i\omega_1 t} + \vec{E}_{02} e^{-i\omega_2 t}\right) - a\left(\frac{e}{m}\right)^2\left(\alpha_1\vec{E}_{01} e^{-i\omega_1 t} + \alpha_2\vec{E}_{02} e^{-i\omega_2 t}\right)^2 \quad (47)$$

$$\leftrightarrow \ddot{x} + \Gamma\dot{x} + {\omega_0}^2 x = -\frac{e}{m}\left(\vec{E}_{01} e^{-i\omega_1 t} + \vec{E}_{02} e^{-i\omega_2 t}\right) - a\left(\frac{e}{m}\right)^2\left[\left(\alpha_1\vec{E}_{01}\right)^2 e^{-i2\omega_1 t} + \left(\alpha_2\vec{E}_{02}\right)^2 e^{-i2\omega_2 t} + 2\alpha_1\vec{E}_{01}\alpha_2\vec{E}_{02} e^{-i(\omega_1+\omega_2)t}\right] \quad (48)$$

Similarly, the solution of the first order term is assumed to have the form as,

$$\vec{x}^1 = \vec{x}^1_{01}e^{-i\varpi_1 t} + \vec{x}^1_{02}e^{-i\varpi_2 t} + \vec{x}^1_{03}e^{-i2\varpi_1 t} + \vec{x}^1_{04}e^{-i2\varpi_2 t} + \vec{x}^0_{05}e^{-i(\varpi_1+\varpi_2)t}$$

Introducing this and its derivatives into Eq. (48), I obtain

$$\begin{aligned}
&\vec{x}^1_{01}e^{-i\omega_1 t}({\omega_0}^2-{\omega_1}^2 - i\omega_1\Gamma) + \vec{x}^1_{02}e^{-i\omega_2 t}({\omega_0}^2-{\omega_2}^2 - i\omega_2\Gamma)\\
&\quad + \vec{x}^1_{03}e^{-i2\omega_1 t}[{\omega_0}^2-(2\omega_1)^2 - i2\omega_1\Gamma]\\
&\quad + \vec{x}^1_{04}e^{-i2\omega_2 t}[{\omega_0}^2-(2\omega_2)^2 - i2\omega_2\Gamma]\\
&\quad + \vec{x}^0_{05}e^{-i(\omega_1+\omega_2)t}[{\omega_0}^2-(\omega_1+\omega_2)^2 - i(\omega_1+\omega_2)\Gamma]\\
&\quad = -\frac{e}{m}\left(\vec{E}_{01}e^{-i\omega_1 t} + \vec{E}_{02}e^{-i\omega_2 t}\right)\\
&\quad - a\left(\frac{e}{m}\right)^2\left[\left(\alpha_1\vec{E}_{01}\right)^2 e^{-i2\omega_1 t} + \left(\alpha_2\vec{E}_{02}\right)^2 e^{-i2\omega_2 t}\right.\\
&\quad \left. + 2\alpha_1\vec{E}_{01}\alpha_2\vec{E}_{02}e^{-i(\omega_1+\omega_2)t}\right]
\end{aligned} \tag{49}$$

Equating the coefficients on both sides of (49), I obtain

$$\vec{x}^1_{01} = -\frac{e}{m}\frac{\vec{E}_{01}}{({\omega_0}^2-{\omega_1}^2 - i\omega_1\Gamma)} \tag{50}$$

$$\vec{x}^1_{02} = -\frac{e}{m}\frac{\vec{E}_{02}}{({\omega_0}^2-{\omega_2}^2 - i\omega_2\Gamma)} \tag{51}$$

$$\vec{x}^1_{03} = -a\left(\frac{e}{m}\right)^2\frac{{\vec{E}_{01}}^2}{({\omega_0}^2-{\omega_1}^2 - i\omega_1\Gamma)^2[{\omega_0}^2-(2\omega_1)^2 - i2\omega_1\Gamma]} \tag{52}$$

$$\vec{x}^1_{04} = -a\left(\frac{e}{m}\right)^2\frac{{\vec{E}_{02}}^2}{({\omega_0}^2-{\omega_2}^2 - i\omega_2\Gamma)^2[{\omega_0}^2-(2\omega_2)^2 - i2\omega_2\Gamma]} \tag{53}$$

$$\begin{aligned}
&\vec{x}^1_{05}\\
&= -\frac{a\left(\frac{e}{m}\right)^2 2\vec{E}_{01}\vec{E}_{02}}{({\omega_0}^2-{\omega_1}^2 - i\omega_1\Gamma)({\omega_0}^2-{\omega_2}^2 - i\omega_2\Gamma)[{\omega_0}^2-(\omega_1+\omega_2)^2 - i(\omega_1+\omega_2)\Gamma]}
\end{aligned} \tag{54}$$

Here, the expression for $\vec{x}^1$ contains the frequencies, ω_1, ω_2, $2\omega_1$, $2\omega_2$, and $\omega_1 + \omega_2$.

Look at the first term $\varepsilon_0\chi^{(1)}\vec{E}$ in equation (8) where the linear susceptibility is defined as

$$\vec{P}(\omega_1) = \varepsilon_0\chi^{(1)}\vec{E}(\omega_1) \tag{55}$$

Since the linear polarization is given by

$$\vec{P} = -Ne\vec{x} = -Ne\vec{x}^1_{01} \tag{56}$$

using three Eqs. (50), (55), and (56) I have

$$\chi^{(1)}(\omega_1) = \frac{Ne}{\varepsilon_0}\frac{e}{m}\frac{1}{({\omega_0}^2-{\omega_1}^2 - i\omega_1\Gamma)} \tag{57}$$

More importantly, the nonlinear susceptibility $\chi^{(2)}$ then can be calculated in the same way where nonlinear polarization at frequency $2\omega_1$ are as given below

$$\vec{P} = -Ne\vec{x}_{03}^{1} = \varepsilon_0\chi^{(2)}\vec{E}\vec{E}$$

$$\chi^{(2)} = a\frac{Ne}{\varepsilon_0}\left(\frac{e}{m}\right)^2 \frac{1}{(\omega_0{}^2-\omega_1{}^2 - i\omega_1\Gamma)^2[\omega_0{}^2-(2\omega_1)^2 - i2\omega_1\Gamma]} \quad (58)$$

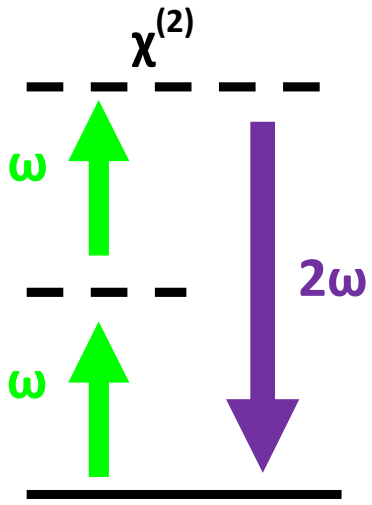

Fig. 2.8. Energy level description of the SHG process.

Interestingly, this simple model allows us to reveal the basic characteristic of SHG process. In principle, when an intense laser beam with frequency ω hits on the sample having a nonzero value of $\chi^{(2)}$, the laser beam emerging from the sample then contains the frequencies ω and 2ω. This process can be considered from the energy diagram as shown in Fig. 2.8. It shows that two photons of the fundamental frequency ω combine to produce a photon 2ω. The energy levels $\hbar\omega$ and $2\hbar\omega$ shown in dashed lines are known as virtual levels since they are not eigenstates of the material in which the second harmonic radiation is generated [43]. Equation (58) indicates that in the material with negligible damping Γ constant, the process of SHG can be enhanced when fundamental photon ω_1 or doubled frequency photon $2\omega_1$ coincides with the oscillation frequency of the electron ω_0.

2.3.2. Non-linear optical effects in plasmonic structures

The optical properties of metallic nanostructures are dictated by the collective oscillations of conduction electrons [44]. The oscillations produce plasmon resonances and

these resonance peaks depend on various parameters such as size, shape, dielectric function or surrounding media [45,46,47]. The resonances can lead to strong enhancement of the local electric fields near the vicinity of nanostructure and result in the enhancement of the optical responses of the structure. Especially the nonlinear case, the effect will emerge clearly caused by the proportion to high power of the local field [48].

For the nonlinear optical processes, especially second order nonlinear optics, the plasmonic structures can effect on the SHG signal in two main ways. First, by designing the specific metallic nanostructures one can add the local field factor into the local electric field near the metal-dielectric interface [49,50]. The major contribution to the enhancement of local field factor is surface plasmon resonance [50]. Second, the SHG signal could result from the sensitivity of dielectric properties of nanostructures with respect to the plasmonic excitation parameters including the excitation wavelength, shape or the mutual arrangement of the metallic nanostructures. In the nonlinear optics, we can exploit such sensitivity to modify the refractive indices of metallic nanostructures and therefore shift the peak of plasmonic resonance [48].

In general, the origin of the nonlinearity might vary when we modify the studied systems. One or two processes might occur simultaneously. To understand the origin of SHG in metallic nanostructures, let us consider the basic concept reported by H. Sano et al. [51] and Valev et al. [9]. Second order nonlinear polarization in nanostructure can be expressed as a generalized polarization [52],

$$\mathbf{P}(2\omega) = \mathbf{P} - \nabla.\mathbf{Q} + \frac{\mu_0}{i\omega}\nabla \times \mathbf{M} + \cdots \tag{59}$$

On the right hand side, **P**, **Q**, and **M** present the electric dipole, electric quadrupole, and magnetic dipole, respectively. μ_0 is the permeability of the vacuum and ω is the angular frequency of the incident laser. In other words, nonlinear polarization is related to the incident electric fields as follows,

$$P_i(2\omega) \propto P_i^D(2\omega) + P_i^Q(2\omega) \propto \chi_{ijk}^{(2)} : E_j E_k + \Gamma_{ijkl} \vdots E_j(\omega)\nabla_k E_l(\omega) \tag{60}$$

The first part,

$$P_i^D(2\omega) = \chi_{ijk}^{(2)} : E_j E_k \tag{61}$$

expresses the second-order term of nonlinear polarization as a function of two applied electric fields E_j and E_k . This first term is the electric dipole allowed nonlinear optical response. The second part,

$$P_i^Q(2\omega) = \Gamma_{ijkl} \vdots E_j(\omega)\nabla_k E_l(\omega) \quad (62)$$

results from the nonlocal response of the system and is expressed as a function of the gradient of the electric field. Such nanoscale gradient in the local material properties and fields creates the contribution from higher multipole including electric quadrupole and magnetic dipole contributions [53]. In particular, if we perceive Eqs. (59) and (62), the quadrupolar term essentially contains the spatial derivatives of fields and it results in the second order optical response. From a different point of view, Fig 2.9 shows the simple schematic of the radiative properties of an electric dipole (p), magnetic dipole (m), and quadrupole (Q). The direction of the electric field is shown together with the electric field E of electric dipole (p), magnetic dipole (m), and quadrupole (Q).

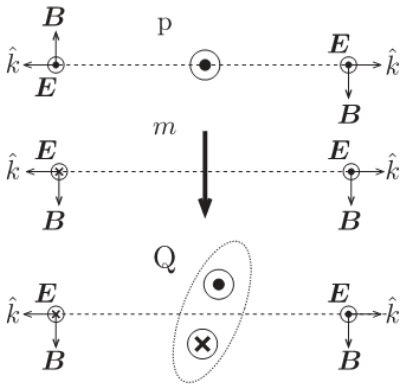

Fig 2.9. Simple schematic of the radiative properties of an electric dipole (p), magnetic dipole (m), and quadrupole (Q) [53].

Here χ_{ijk} and Γ_{ijkl} are second and third rank susceptibility tensors, respectively. i, j, k, and l indicated 1, 2 and 3 indexes forming a orthogonal coordinate system. Here, 1 and 2 coordinates are in sample plane and perpendicular to each other whereas 3 perpendicular to the sample substrate. Considering the electric dipole contribution, generally, nonlinear susceptibility tensor χ_{ijk} will contain 27 elements. Nevertheless, I can reduce the number of elements by investigating the symmetry of the surface. In the simplest case, an isotropic

surface belonging to $C_{\infty v}$ symmetry as deduce below, the susceptibility tensor χ_{ijk} has only three independent components, $\chi_{311}^{(2)}$, $\chi_{113}^{(2)}$, and $\chi_{333}^{(2)}$. For each specific shape of metallic nanostructure, one can phenomenologically consider the macroscopic symmetry of the artificial structure and thus add a suitable amount of nonlinear susceptibility elements for calculation. Such kind of this process will be applied in our fitting process during interpreting the experimental data. The detail will be presented in Section 5.3.1 of Chapter 5.

The second part in Eq.(60) contains the bulk-specific electric quadrupole and magnetic dipole contributions. It should be noted that the operator in front of magnetic dipole in Eq. (59) shows the spatial derivation, the magnetic dipole contribution therefore belongs to nonlocal response. Within electric-dipole approximation, the SHG signal is forbidden in the bulk materials possessing inversion centrosymmetry. However, if we go beyond the limitation of electric-dipole approximation, the higher multipole contributions (electric quadrupole and magnetic dipole) should be taken into account in the SHG signal [54]. Especially, at the interface between two media, the amplitude of the component of electric field normal to the boundary will drastically change. This could lead to a large gradient in the fundamental electric field normal to the boundary [55]. Such gradients, as denoted by ∇_k operator, may result in the higher multipole interactions and generate a noticeable SHG from bulk contribution. As imaginatively depicted in Fig. 2.9, one can see that the reflected SHG signal in the centrosymmetric materials receives two contributions. The first one causes by the zone close to the surface (a few Å) where the electrons "feel" the broken symmetry. The other part results from the volume nonlinear contribution caused by the longer spatial interaction within the bulk [56].

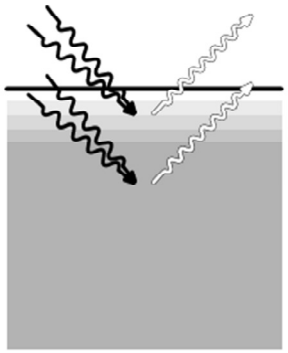

Fig. 2.10. SHG is produced close to the surface and at the bulk [59].

Because of the third rank tensor, nonlinear susceptibility element Γ_{ijkl} is different from zero even if within media with inversion centrosymmetry. Generally, the third rank tensor Γ_{ijkl} contains a huge quality consisting of 81 elements. Again, one can extract the necessary components based on the specific case owning to the symmetry of material. For instance, in the case of the m3m symmetry (isotropic medium), there are only four independent tensor components, Γ_{1111}, Γ_{1221}, Γ_{1122}, and Γ_{1212} [57,58, 59].

Again, let us look at Eq. (60), the electric field in this equation relates specifically to the electric field vectors at the surface (local electric field), not to those propagating through space. If I assume $E_{local}(\varpi) = L(\varpi).E(\varpi)$, I obtain [16,50],

$$\begin{aligned} P_{i\,local}(2\omega) &\propto \chi^{(2)}_{ijk}\vdots E_{j\,local}\,E_{k\,local} + \Gamma_{ijkl} \vdots E_{j\,local}(\omega)\nabla_k E_{l\,local}\,(\omega) \\ &\propto L(2\varpi)\chi^{(2)}_{ijk}\vdots L(\varpi)E_j\,L(\varpi)E_k + L(2\varpi)\Gamma_{ijkl} \\ &\vdots L(\varpi)E_j\,(\omega)\nabla_k L(\varpi)E_l\,(\omega) \\ &\propto L(2\varpi)|L(\varpi)|^2\left(\chi^{(2)}_{ijk}\vdots E_j\,E_k + \Gamma_{ijkl}\vdots E_j\,(\omega)\nabla_k E_l\,(\omega)\right) \end{aligned} \tag{63}$$

where $L(\varpi)$ and $L(2\varpi)$ represent the local field factors for the fundamental and the second harmonic frequency. These terms include the Fresnel factors [50,60]. Thus, the intensity at the second harmonic can be expressed as:

$$I(2\omega) \propto \left|L(\omega)^2.L(2\omega).\chi^{(2),eff}_{ijk}.I(\omega)\right|^2 \tag{64}$$

where $\chi^{(2),eff}_{ijk}$ is the effective nonlinear susceptibility incorporating the surface and bulk contributions. It will be defined comprehensively in the following paragraph. The relationship shown in Eq. (64) implies that, in metallic nanostructures, any changes in local field factor or fundamental light intensity could be obviously resolved from the second order nonlinear optical standpoint. This key will be exploited in Section 5.2 of Chapter 5 to argue whether plasmon exciation occurs in the case of the V-shaped Cr nanhole arrays.

At the surface of the metallic nanostructures with low symmetry, surface second harmonic generation is the favorable technique used to investigate the nonlinear optical response [61]. Since it is sensitive with respect to the symmetry, the SHG process always occurs at the surface where the broken symmetry condition is always fulfilled. However, the difficult issue is to estimate as well as separate the local surface and nonlocal bulk contribution with respect to the total SHG signal [62,63,64,65] since each term of Eq.(60)

consists of both surface and bulk contributions [51]. In the case of metallic nanomaterials, the problem becomes more complicated [50,66]. According to H. Sano's report [51], the bulk contribution of the first term $\chi_b^{(2)}$ in Eq. (60) vanishes in the centrosymmetric materials whereas the surface contribution of the first term $\chi_s^{(2)}$ is predominant since at the surface the broken symmetry always maintains. Generally, in non-centrosymmetric materials the bulk quadrupole contribution Γ_b of the second term is quite small compared with the bulk contribution $\chi_b^{(2)}$of the first term, and its amplitude is of the order of that with $\chi_s^{(2)}$. However, in the surface region the surface contribution Γ_s of the second term is expected to be essential because the amplitude of the electric field normal to the surface significantly changes. It should be noted that it is difficult to separate the contribution of $\chi_s^{(2)}$and Γ_s, therefore surface nonlinear polarization P_s^{NL} is often expressed by using effective surface nonlinear susceptibility $\chi_{\mathrm{S}}^{(2),\mathrm{eff}}$ [51,63],

$$\mathrm{P}_S^{NL}(2\omega) = \chi_{\mathrm{S,ijk}}^{(2),\mathrm{eff}} : \mathrm{E_j}\,\mathrm{E_k} \tag{65}$$

as regarded in Eq. (64). From now on, $\chi_s^{(2)}$and Γ_s are implicatively incorporated into $\chi_{\mathrm{S,ijk}}^{(2),\mathrm{eff}}$ and I will omit superscript "eff" in the following expressions for simplification.

2.4. Azimuthal angle dependence of optical second harmonic intensity

2.4.1. Second harmonic generation

In the azimuthal measurement, with the knowledge of the relationships between the dependence of the second order polarization $P(2\varpi)$ and the second-order susceptibility elements $\chi_{\mathrm{ijk}}^{(2)}$, I can obtain a various combination of the nonlinear susceptibility elements. A simultaneous equation of the tensor components can be generated from different configuration combination. The advantage of azimuthal angle dependence of optical second harmonic intensity is the fact that all nonlinear susceptibility elements can be extracted and evaluated within the mutual relation. Here, I report the comprehensive

concept presenting how each nonlinear susceptibility element could be estimated by this measurement.

It is known that in MKS units the output intensity of the reflected SHG beam is given by [67]

$$I(2\omega) = \frac{2\omega^2}{\varepsilon_0 c^3 Cos\theta^2} \left| e(2\varpi).\chi^{(2)}: e(\varpi)e(\varpi) \right|^2 \mathrm{I}(\omega)^2 \tag{66}$$

In Eq. (66), I(ω) is the intensity of incoming light, θ is the incident angle. c and ε_0 are the speed of light in vacuum and permittivity of the vacuum, respectively. $e(\varpi)$ and $e(2\varpi)$ present the local fundamental and SHG electric fields. In general, $e(\varpi)$ can be expressed as a function of the local field correction or Fresnel factors $L(\varpi)_{ii}$ and the unit optical field vector $e(\varpi)_{unit}$ as follows (see Fig. 2.11) [67,68],

$$e(\varpi) = L(\varpi)_{ii}.e(\varpi)_{unit} = \begin{pmatrix} L(\varpi)_{xx} & 0 & 0 \\ 0 & L(\varpi)_{yy} & 0 \\ 0 & 0 & L(\varpi)_{zz} \end{pmatrix}.\begin{pmatrix} -cos\alpha cos\theta \\ sin\alpha \\ cos\alpha sin\theta \end{pmatrix} \tag{67}$$

In analogy with the fundamental light, the local SHG electric field $e(2\varpi)$ with the output unit optical electric field vector $e(2\varpi)_{unit}$ can be expressed as

$$e(2\varpi) = L(2\varpi)_{ii}.e(2\varpi)_{unit} = \begin{pmatrix} L(2\varpi)_{xx} & 0 & 0 \\ 0 & L(2\varpi)_{yy} & 0 \\ 0 & 0 & L(2\varpi)_{zz} \end{pmatrix}.\begin{pmatrix} cos\alpha cos\theta \\ sin\alpha \\ cos\alpha sin\theta \end{pmatrix} \tag{68}$$

With the combination of polarizer and analyzer, I am able to specifically decide the input and output electric fields. For instance, with Pin/Pout, the $e(\varpi)_{unit}$ and $e(2\varpi)_{unit}$ will be

$$e(\varpi)_{unit} = \begin{pmatrix} -cos\theta \\ 0 \\ sin\theta \end{pmatrix} \tag{69}$$

$$e(2\varpi)_{unit} = \begin{pmatrix} cos\theta \\ 0 \\ sin\theta \end{pmatrix} \tag{70}$$

While in the case of Sin/Sout, these will be expressed as,

$$e(\varpi)_{unit} = \begin{pmatrix} 0 \\ 1 \\ 0 \end{pmatrix} \tag{71}$$

$$e(2\varpi)_{unit} = \begin{pmatrix} 0 \\ 1 \\ 0 \end{pmatrix} \tag{72}$$

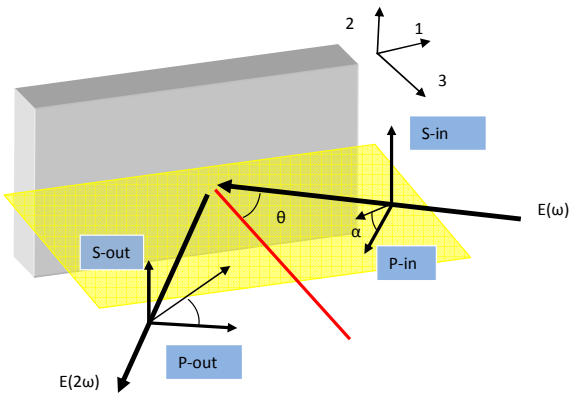

Fig. 2.11. Geometry of the unit optical field vectors $e(\varpi)_{unit}$ and $e(2\varpi)_{unit}$ in SHG.

From now, I can roughly calculate the term $\left|e(2\varpi).\chi^{(2)}:e(\varpi)e(\varpi)\right|^2$. However, it can be simpler if I know the surface symmetry. The number of the nonlinear susceptibility elements $\chi^{(2)}$can be reduced significantly. It should be noted that in azimuthal measurement, sample will be rotated about surface normal, $\chi^{(2)}$ therefore has to be converted from sample-fixed axis system to laboratory-fixed axes.

2.4.2. Nonlinear susceptibility element and symmetric consideration

First, let us consider the symmetric property of $\chi_{ijk}^{(2)}$. So far, I have discussed that the $\chi_{ijk}^{(2)}$ is a second rank tensor describing the second-order nonlinear optical susceptibility elements and it includes 27 elements. The inherent property of the material decides the symmetry and therefore the number of $\chi_{ijk}^{(2)}$ element. For the particular metallic nanostructures, I can estimate the surface symmetry based on their shape and greatly reduce the $\chi^{(2)}$ elements. For instance, with a media processing inversion centrosymmetry, all directions are the same and the value of $\chi_{ijk}^{(2)}$ for two opposing directions must be identical [60]

$$\chi_{ijk}^{(2)} = \chi_{-i-j-k}^{(2)} \tag{73}$$

Furthermore, from the physical point of view as the coordinates are reversed, the physical phenomenon must also change the sign or,

$$\chi_{ijk}^{(2)} = \chi_{-i-j-k}^{(2)} = -\chi_{i-j-k}^{(2)} = \chi_{ij-k}^{(2)} = -\chi_{ijk}^{(2)} \tag{74}$$

The result shows that in a centrosymmetric medium SHG is forbidden. However, at the surface or interface, the broken symmetry always remains and therefore SHG is active. In

order to obtain the number of nonlinear susceptibility element, one can examine the symmetry of the nanostructure material lying on the planar surfaces. Concerning the V-shaped structure studied in this work, I can intuitively find out its C_s symmetry since V shape has a plane reflection σ_1 containing the bisector passing V shape's tip as show in Fig. 2.12.

Here, direction 3 is defined as the normal to the surface while 1 and 2 directions are on the sample surface. 1 indicates the direction of the bisector of the V passing through its apex in the substrate plane. It should be note that (1,2,3) forms the sample–fixed axes and that definition is very important when I transfer the $\chi^{(2)}_{ijk}$ elements from the sample-fixed axes to the laboratory-fixed axes in azimuthal angle dependence of optical second harmonic measurement. With a surface owing C_s symmetry, I have "3≠-3" and "1≠-1" but "2=-2". I can apply the rule deduced in Eq. (74) to assign the number of nonlinear susceptibility element. The result is shown in Table 2.2.

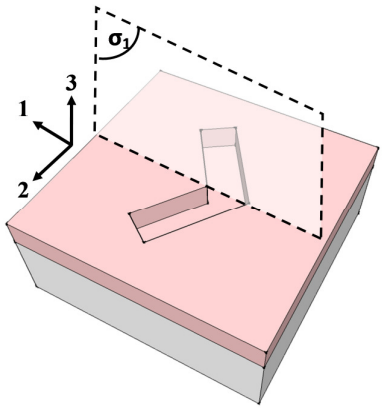

Fig.2.12. Plane reflection σ_1 contains the bisector passing V shape's tip.

Moreover, the intrinsic permutation symmetry of $\chi^{(2)}_{ijk}$ makes the $\chi^{(2)}_{ijk} = \chi^{(2)}_{ikj}$ because the response of the medium cannot "recognize" on the mathematical ordering of the fields. Thus I have ten independent nonlinear susceptibility elements, $\chi^{(2)}_{223} = \chi^{(2)}_{232}$, $\chi^{(2)}_{113} = \chi^{(2)}_{131}$, $\chi^{(2)}_{212} = \chi^{(2)}_{221}$, $\chi^{(2)}_{122}$, $\chi^{(2)}_{111}$, $\chi^{(2)}_{133}$, $\chi^{(2)}_{313} = \chi^{(2)}_{331}$, $\chi^{(2)}_{322}$, $\chi^{(2)}_{311}$, and $\chi^{(2)}_{333}$ in the case of C_s symmetry.

By doing in the same manner, the $C_{\infty v}$ surface will give only three independent tensor components. For instance, in the case of an isotropic surface such as an amorphous continuous metal three independent nonlinear susceptibility element

$\chi^{(2)}_{223} = \chi^{(2)}_{232} = \chi^{(2)}_{113} = \chi^{(2)}_{131}$, $\chi^{(2)}_{322} = \chi^{(2)}_{311}$, and $\chi^{(2)}_{333}$ are permitted as regarded previously. The result is shown in Table 2.3. Here, since the surface is isotropic, another σ_2 plane will be able to effect on coordinate 1.

Table 2.2. Assignment of the number of $\chi^{(2)}_{ijk}$ element in the case of C_s symmetry.

$\boldsymbol{\chi^{(2)}_{ijk}}$	**Apply σ_1 plane**	**Contribution**
$\chi^{(2)}_{222}$	$\boldsymbol{\chi^{(2)}_{222} = \chi^{(2)}_{-2-2-2} = -\chi^{(2)}_{222}}$	No
$\chi^{(2)}_{221}$	$\boldsymbol{\chi^{(2)}_{221} = \chi^{(2)}_{-2-21} = \chi^{(2)}_{221}}$	Yes
$\chi^{(2)}_{223}$	$\boldsymbol{\chi^{(2)}_{223} = \chi^{(2)}_{-2-23} = \chi^{(2)}_{223}}$	Yes
$\chi^{(2)}_{212}$	$\boldsymbol{\chi^{(2)}_{212} = \chi^{(2)}_{-21-2} = \chi^{(2)}_{212}}$	Yes
$\chi^{(2)}_{211}$	$\boldsymbol{\chi^{(2)}_{211} = \chi^{(2)}_{-211} = -\chi^{(2)}_{211}}$	No
$\chi^{(2)}_{213}$	$\boldsymbol{\chi^{(2)}_{213} = \chi^{(2)}_{-213} = -\chi^{(2)}_{213}}$	No
$\chi^{(2)}_{232}$	$\boldsymbol{\chi^{(2)}_{232} = \chi^{(2)}_{-23-2} = \chi^{(2)}_{232}}$	Yes
$\chi^{(2)}_{231}$	$\boldsymbol{\chi^{(2)}_{231} = \chi^{(2)}_{-231} = -\chi^{(2)}_{231}}$	No
$\chi^{(2)}_{233}$	$\boldsymbol{\chi^{(2)}_{233} = \chi^{(2)}_{-233} = -\chi^{(2)}_{233}}$	No
$\chi^{(2)}_{122}$	$\boldsymbol{\chi^{(2)}_{122} = \chi^{(2)}_{1-2-2} = \chi^{(2)}_{122}}$	Yes
$\chi^{(2)}_{121}$	$\boldsymbol{\chi^{(2)}_{121} = \chi^{(2)}_{1-21} = -\chi^{(2)}_{121}}$	No
$\chi^{(2)}_{123}$	$\boldsymbol{\chi^{(2)}_{123} = \chi^{(2)}_{1-23} = -\chi^{(2)}_{123}}$	No
$\chi^{(2)}_{112}$	$\boldsymbol{\chi^{(2)}_{112} = \chi^{(2)}_{11-2} = -\chi^{(2)}_{112}}$	No
$\chi^{(2)}_{111}$	no effect	Yes
$\chi^{(2)}_{113}$	no effect	Yes
$\chi^{(2)}_{132}$	$\boldsymbol{\chi^{(2)}_{132} = \chi^{(2)}_{13-2} = -\chi^{(2)}_{132}}$	No
$\chi^{(2)}_{131}$	no effect	Yes
$\chi^{(2)}_{133}$	no effect	Yes
$\chi^{(2)}_{322}$	$\boldsymbol{\chi^{(2)}_{322} = \chi^{(2)}_{3-2-2} = \chi^{(2)}_{322}}$	Yes
$\chi^{(2)}_{321}$	$\boldsymbol{\chi^{(2)}_{321} = \chi^{(2)}_{3-21} = -\chi^{(2)}_{321}}$	No
$\chi^{(2)}_{323}$	$\boldsymbol{\chi^{(2)}_{323} = \chi^{(2)}_{3-23} = -\chi^{(2)}_{323}}$	No
$\chi^{(2)}_{312}$	$\boldsymbol{\chi^{(2)}_{312} = \chi^{(2)}_{31-2} = -\chi^{(2)}_{312}}$	No
$\chi^{(2)}_{311}$	no effect	Yes
$\chi^{(2)}_{313}$	no effect	Yes
$\chi^{(2)}_{332}$	$\boldsymbol{\chi^{(2)}_{332} = \chi^{(2)}_{33-2} = -\chi^{(2)}_{332}}$	No
$\chi^{(2)}_{331}$	no effect	Yes
$\chi^{(2)}_{333}$	no effect	Yes

Table 2.3. Assignment of the number of $\chi^{(2)}_{ijk}$ element in the case of $C_{\infty v}$ symmetry.

$\boldsymbol{\chi^{(2)}_{ijk}}$	**Apply σ_1 plane**	**Apply σ_2 plane**	**Contribution**
$\chi^{(2)}_{222}$	$\boldsymbol{\chi^{(2)}_{222} = \chi^{(2)}_{-2-2-2} = -\chi^{(2)}_{222}}$		No
$\chi^{(2)}_{221}$		$\boldsymbol{\chi^{(2)}_{221} = \chi^{(2)}_{221} = -\chi^{(2)}_{221}}$	No
$\chi^{(2)}_{223}$	$\boldsymbol{\chi^{(2)}_{223} = \chi^{(2)}_{-2-23} = \chi^{(2)}_{223}}$		Yes
$\chi^{(2)}_{212}$		$\boldsymbol{\chi^{(2)}_{212} = \chi^{(2)}_{2-12} = -\chi^{(2)}_{212}}$	No
$\chi^{(2)}_{211}$	$\boldsymbol{\chi^{(2)}_{211} = \chi^{(2)}_{-211} = -\chi^{(2)}_{211}}$		No
$\chi^{(2)}_{213}$	$\boldsymbol{\chi^{(2)}_{213} = \chi^{(2)}_{-213} = -\chi^{(2)}_{213}}$		No
$\chi^{(2)}_{232}$	$\boldsymbol{\chi^{(2)}_{232} = \chi^{(2)}_{-23-2} = \chi^{(2)}_{232}}$		Yes
$\chi^{(2)}_{231}$	$\boldsymbol{\chi^{(2)}_{231} = \chi^{(2)}_{-231} = -\chi^{(2)}_{231}}$		No
$\chi^{(2)}_{233}$	$\boldsymbol{\chi^{(2)}_{233} = \chi^{(2)}_{-233} = -\chi^{(2)}_{233}}$		No
$\chi^{(2)}_{122}$		$\boldsymbol{\chi^{(2)}_{122} = \chi^{(2)}_{-122} = -\chi^{(2)}_{122}}$	No
$\chi^{(2)}_{121}$	$\boldsymbol{\chi^{(2)}_{121} = \chi^{(2)}_{1-21} = -\chi^{(2)}_{121}}$		No
$\chi^{(2)}_{123}$	$\boldsymbol{\chi^{(2)}_{123} = \chi^{(2)}_{1-23} = -\chi^{(2)}_{123}}$		No
$\chi^{(2)}_{112}$	$\boldsymbol{\chi^{(2)}_{112} = \chi^{(2)}_{11-2} = -\chi^{(2)}_{112}}$		No
$\chi^{(2)}_{111}$		$\boldsymbol{\chi^{(2)}_{111} = \chi^{(2)}_{-1-1-1} = -\chi^{(2)}_{111}}$	No
$\chi^{(2)}_{113}$		$\boldsymbol{\chi^{(2)}_{113} = \chi^{(2)}_{-1-13} = \chi^{(2)}_{113}}$	Yes
$\chi^{(2)}_{132}$	$\boldsymbol{\chi^{(2)}_{132} = \chi^{(2)}_{13-2} = -\chi^{(2)}_{132}}$		No
$\chi^{(2)}_{131}$		$\boldsymbol{\chi^{(2)}_{131} = \chi^{(2)}_{-13-1} = \chi^{(2)}_{131}}$	Yes
$\chi^{(2)}_{133}$		$\boldsymbol{\chi^{(2)}_{133} = \chi^{(2)}_{-133} = -\chi^{(2)}_{133}}$	No
$\chi^{(2)}_{322}$	$\boldsymbol{\chi^{(2)}_{322} = \chi^{(2)}_{3-2-2} = \chi^{(2)}_{322}}$		Yes
$\chi^{(2)}_{321}$	$\boldsymbol{\chi^{(2)}_{321} = \chi^{(2)}_{3-21} = -\chi^{(2)}_{321}}$		No
$\chi^{(2)}_{323}$	$\boldsymbol{\chi^{(2)}_{323} = \chi^{(2)}_{3-23} = -\chi^{(2)}_{323}}$		No
$\chi^{(2)}_{312}$	$\boldsymbol{\chi^{(2)}_{312} = \chi^{(2)}_{31-2} = -\chi^{(2)}_{312}}$		No
$\chi^{(2)}_{311}$		$\boldsymbol{\chi^{(2)}_{311} = \chi^{(2)}_{3-1-1} = \chi^{(2)}_{311}}$	Yes
$\chi^{(2)}_{313}$		$\boldsymbol{\chi^{(2)}_{313} = \chi^{(2)}_{3-13} = -\chi^{(2)}_{313}}$	No
$\chi^{(2)}_{332}$	$\boldsymbol{\chi^{(2)}_{332} = \chi^{(2)}_{33-2} = -\chi^{(2)}_{332}}$		No
$\chi^{(2)}_{331}$		$\boldsymbol{\chi^{(2)}_{331} = \chi^{(2)}_{33-1} = -\chi^{(2)}_{331}}$	No
$\chi^{(2)}_{333}$	no effect	no effect	Yes

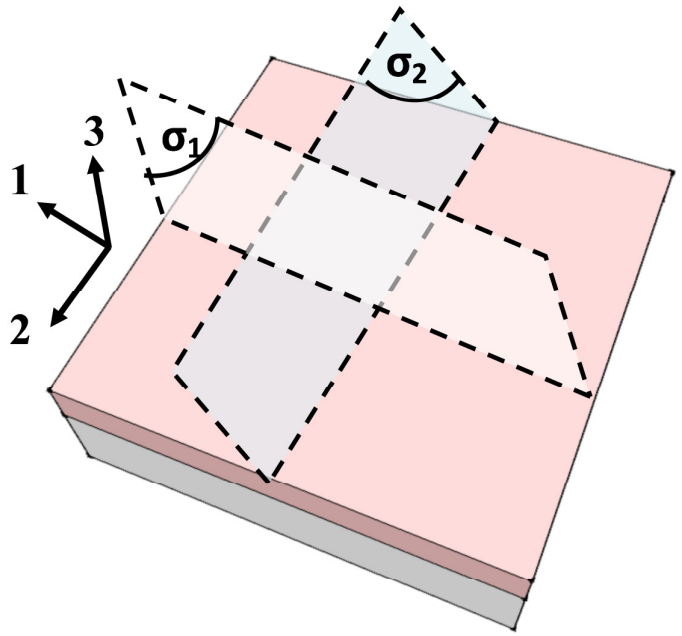

Fig. 2.13. Two reflection planes σ_1, σ_2 in the case of isotropic surface.

As noticed above, these tensor components are obviously associated with the sample-fixed axis system. In the azimuthal measurement, as the sample rotate the second order nonlinear polarizations are analyzed with respect to the input and output electric fields within the laboratory-fixed axes. Thus, before applying Eq. (65) to obtain SHG intensity as a function of the azimuthal angle φ, I have to transfer all the $\chi_{ijk}^{(2)}$ elements from the sample-fixed coordinate to the laboratory-fixed coordinate. Here $\chi_{ijk}^{(2)}$ third-rank tensor in laboratory-fixed coordinate is related to $\chi_{ijk}^{(2)}$ third-rank tensor in the sample-fixed coordinate through the Euler transformations as follow [69,70],

$$R = \begin{pmatrix} \cos\psi & \sin\psi & 0 \\ -\sin\psi & \cos\psi & 0 \\ 0 & 0 & 1 \end{pmatrix} . \begin{pmatrix} \cos\Xi & 0 & -\sin\Xi \\ 0 & 1 & 0 \\ \sin\Xi & 0 & \cos\Xi \end{pmatrix} . \begin{pmatrix} \cos\varphi & \sin\varphi & 0 \\ -\sin\varphi & \cos\varphi & 0 \\ 0 & 0 & 1 \end{pmatrix} \quad (75)$$

In azimuthal measurement, since the sample only rotate around the surface normal I only use rotation matrix around 3 axis,

$$\mathrm{R_{il}} = \begin{pmatrix} \cos\varphi & \sin\varphi & 0 \\ -\sin\varphi & \cos\varphi & 0 \\ 0 & 0 & 1 \end{pmatrix} \quad (76)$$

R_{il} is the element of the rotation matrix containing the directional cosines between the laboratory-fixed and crystal-fixed axes. $\chi_{ijk}^{(2)}$ therefore can be transferred into laboratory-fixed axes as follow,

$$\chi_{ijk}^{(2)}\text{lab} = R_{il}R_{jm}R_{kn}\chi_{lmn}^{(2)} \tag{77}$$

For the following discussion, φ is understood as the angle between the 1 axis and incident plane. The schematic illustration is depicted in Fig. 2.14. To calculate Eq. (77), the multiplication was converted to Mathematica code in order to avoid errors. The obtained $\chi_{ijk}^{(2)}$ second-rank tensor of C_s surface in the laboratory-fixed coordinate as follows,

$$\chi_{111}^{(2)}\text{lab} = \cos\varphi^3\chi_{111}^{(2)} + \cos\varphi\sin\varphi^2\chi_{122}^{(2)} + 2\cos\varphi\sin\varphi^2\chi_{221}^{(2)} \tag{78}$$

$$\chi_{112}^{(2)}\text{lab} = -\cos\varphi^2\sin\varphi\chi_{111}^{(2)} + \cos\varphi^2\sin\varphi\chi_{122}^{(2)} + \cos\varphi^2\sin\varphi\chi_{221}^{(2)} - \sin\varphi^3\chi_{221}^{(2)} \tag{79}$$

$$\chi_{113}^{(2)}\text{lab} = \cos\varphi^2\chi_{131}^{(2)}\text{lab} + \sin\varphi^2\chi_{232}^{(2)}\text{lab} \tag{80}$$

$$\chi_{121}^{(2)}\text{lab} = -\cos\varphi^2\sin\varphi\chi_{111}^{(2)} + \cos\varphi^2\sin\varphi\chi_{122}^{(2)} + \cos\varphi^2\sin\varphi\chi_{221}^{(2)} - \sin\varphi^3\chi_{221}^{(2)} \tag{81}$$

$$\chi_{122}^{(2)}\text{lab} = \cos\varphi\sin\varphi^2\chi_{111}^{(2)} + \cos\varphi^3\chi_{122}^{(2)} - 2\cos\varphi\sin\varphi^2\chi_{221}^{(2)} \tag{82}$$

$$\chi_{123}^{(2)}\text{lab} = -\cos\varphi\sin\varphi\chi_{131}^{(2)} + \cos\varphi\sin\varphi\chi_{232}^{(2)} \tag{83}$$

$$\chi_{131}^{(2)}\text{lab} = \cos\varphi^2\chi_{131}^{(2)} + \sin\varphi^2\chi_{232}^{(2)} \tag{84}$$

$$\chi_{132}^{(2)}\text{lab} = -\cos\varphi\sin\varphi\chi_{131}^{(2)} + \cos\varphi\sin\varphi\chi_{232}^{(2)} \tag{85}$$

$$\chi_{133}^{(2)}\text{lab} = \cos\varphi\chi_{133}^{(2)} \tag{86}$$

$$\chi_{211}^{(2)}\text{lab} = -\cos\varphi^2\sin\varphi\chi_{111}^{(2)} - \sin\varphi^3\chi_{122}^{(2)} + 2\cos\varphi^2\sin\varphi\chi_{221}^{(2)} \tag{87}$$

$$\chi_{212}^{(2)}\text{lab} = \cos\varphi\sin\varphi^2\sin\varphi\chi_{111}^{(2)} - \cos\varphi\sin\varphi^2\sin\varphi\chi_{122}^{(2)} + \cos\varphi^3\sin\varphi\chi_{221}^{(2)} - \cos\varphi\sin\varphi^2\sin\varphi\chi_{221}^{(2)} \tag{88}$$

$$\chi_{213}^{(2)}\text{lab} = -\cos\varphi\sin\varphi\chi_{131}^{(2)} + \cos\varphi\sin\varphi\chi_{232}^{(2)} \tag{89}$$

$$\chi_{221}^{(2)}\text{lab} = \cos\varphi\sin\varphi^2\chi_{111}^{(2)} - \cos\varphi\sin\varphi^2\chi_{122}^{(2)} + \cos\varphi^3\chi_{221}^{(2)} - \cos\varphi\sin\varphi^2\chi_{221}^{(2)} \tag{90}$$

$$\chi_{222}^{(2)}\text{lab} = -\sin\varphi^3\chi_{111}^{(2)} - \cos\varphi^2\sin\varphi\chi_{122}^{(2)} - 2\cos\varphi^2\sin\varphi\chi_{221}^{(2)} \tag{91}$$

$$\chi_{223}^{(2)}\text{lab} = \sin\varphi^2\chi_{131}^{(2)} + \cos\varphi^2\chi_{132}^{(2)} \tag{92}$$

$$\chi_{231}^{(2)}\text{lab} = -\cos\varphi\sin\varphi\chi_{131}^{(2)} + \cos\varphi\sin\varphi\chi_{232}^{(2)} \tag{93}$$

$$\chi_{232}^{(2)}\text{lab} = \sin\varphi^2\chi_{131}^{(2)} + \cos\varphi^2\chi_{232}^{(2)} \tag{94}$$

$$\chi_{233}^{(2)}\text{lab} = -\sin\varphi\chi_{133}^{(2)} \tag{95}$$

$$\chi_{311}^{(2)}\,\text{lab} \quad = \cos\varphi^2\chi_{311}^{(2)} + \sin\varphi^2\chi_{322}^{(2)} \tag{96}$$

$$\chi_{312}^{(2)}\,\text{lab} = -\cos\varphi\sin\varphi\chi_{311}^{(2)} + \cos\varphi\sin\varphi\chi_{322}^{(2)} \tag{97}$$

$$\chi_{313}^{(2)}\,\text{lab} = \cos\varphi\sin\varphi\chi_{331}^{(2)} \tag{98}$$

$$\chi_{321}^{(2)}\,\text{lab} = -\cos\varphi\sin\varphi\chi_{311}^{(2)} + \cos\varphi\sin\varphi\chi_{322}^{(2)} \tag{99}$$

$$\chi_{322}^{(2)}\,\text{lab} = \sin\varphi^2\chi_{311}^{(2)} + \cos\varphi^2\chi_{322}^{(2)} \tag{100}$$

$$\chi_{323}^{(2)}\,\text{lab} = -\sin\varphi\chi_{331}^{(2)} \tag{101}$$

$$\chi_{331}^{(2)}\,\text{lab} = \cos\varphi\chi_{331}^{(2)} \tag{102}$$

$$\chi_{332}^{(2)}\,\text{lab} = -\sin\varphi\chi_{331}^{(2)} \tag{103}$$

$$\chi_{333}^{(2)}\,\text{lab} = \chi_{333}^{(2)} \tag{104}$$

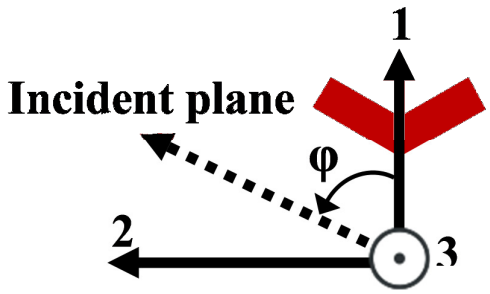

Fig. 2.14. The relative position between the incident plane and the coordinate through the azimuthal angle φ.

2.4.3. Polarization combinations

Up to now, I can definitely calculate $\left|e(2\varpi).\chi^{(2)}\!:e(\varpi)e(\varpi)\right|^2$ as a function of azimuth angle φ and the nonlinear susceptibility element. At the first glance, Eq. (66) seems to be complicated when I include Eqs. (67) and (68). However, I can simplify by different combinations of the input fundamental and output SHG electric fields. The individual elements of nonlinear susceptibility elements then can be determined. Normally, I combine Pin/Pout, Pin/Sout, Sin/Pout, and Sin/Sout to build a simultaneous equation with the unknown tensor components. I again used the Mathematica to handle this multiplication. The results are shown as follows,

$$\left|e(2\varpi).\chi^{(2)}\!:e(\varpi)e(\varpi)\right|^2_{Pin/Pout} = \left|\mathrm{L}(2\omega)_{xx}\cos\theta\{\mathrm{L}(\omega)_{zz}{}^2\sin\theta^2\cos\varphi\chi_{133} + \mathrm{L}(\omega)_{xx}{}^2\cos\theta^2[\cos\varphi^3\chi_{111} + \cos\varphi\sin\varphi^2\chi_{122} + 2\cos\varphi\sin\varphi^2\chi_{221}] - 2\mathrm{L}(\omega)_{xx}\mathrm{L}(\omega)_{zz}\cos\theta sin\theta[\cos\varphi^2\chi_{131} + \sin\varphi^2\chi_{232}]\} + \mathrm{L}(2\omega)_{zz}\sin\theta\{\mathrm{L}(\omega)_{xx}{}^2\cos\theta^2[\cos\varphi^2\chi_{311} + \sin\varphi^2\chi_{322}] - 2\mathrm{L}(\omega)_{xx}\mathrm{L}(\omega)_{zz}\cos\theta\cos\varphi\sin\theta\chi_{331} + \mathrm{L}(\omega)_{zz}{}^2\sin\theta^2\chi_{333}\}\right|^2 \quad (105)$$

$$\left|e(2\varpi).\chi^{(2)}\!:e(\varpi)e(\varpi)\right|^2_{Pin/Sout} = \left|\mathrm{L}(2\omega)_{yy}\{-\mathrm{L}\omega zz^2 sin\theta^2\sin\varphi\chi_{133} + \mathrm{L}(\omega)_{xx}{}^2\cos\theta^2[-\cos\varphi^2\sin\varphi\chi_{111} - \sin\varphi^3\chi_{122} + 2\cos\varphi^2\sin\varphi\chi_{221}] - 2\mathrm{L}(\omega)_{xx}\mathrm{L}(\omega)_{zz}\cos\theta\sin\theta[-\cos\varphi\sin\varphi\chi_{131} + \cos\varphi\sin\varphi\chi_{232}]\}\right|^2 \quad (106)$$

$$\left|e(2\varpi).\chi^{(2)}\!:e(\varpi)e(\varpi)\right|^2_{Sin/Pout} = \left|\mathrm{L}(2\omega)_{xx}\mathrm{L}(\omega)_{yy}{}^2\cos\theta[\cos\varphi\sin\varphi^2\chi_{111} + \cos\varphi^3\chi_{122} - 2\cos\varphi\sin\varphi^2\chi_{221}] + \mathrm{L}(2\omega)_{zz}\mathrm{L}(\omega)_{yy}{}^2\sin\theta[\sin\varphi^2\chi_{311} + \cos\varphi^2\chi_{322}]\right|^2 \quad (107)$$

$$\left|e(2\varpi).\chi^{(2)}\!:e(\varpi)e(\varpi)\right|^2_{Sin/Sout} = \left|\mathrm{L}(2\omega)_{yy}\mathrm{L}(\omega)_{yy}{}^2[-\sin\varphi^3\chi_{111} - \cos\varphi^2\sin\varphi\chi_{122} - 2\cos\varphi^2\sin\varphi\chi_{221}]\right|^2 \quad (108)$$

By doing in the same manner, I obtained the $\chi^{(2)}_{ijk}$ second-rank tensor of $C_{\infty V}$ surface in the laboratory-fixed coordinate as follows,

$$\chi^{(2)}_{111}\mathrm{lab} = 0 \quad (109)$$

$$\chi^{(2)}_{112}\mathrm{lab} = 0 \quad (110)$$

$$\chi^{(2)}_{113}\mathrm{lab} = \cos\varphi^2\chi^{(2)}_{131}\mathrm{lab} + \sin\varphi^2\chi^{(2)}_{232}\mathrm{lab} \quad (111)$$

$$\chi^{(2)}_{121}\mathrm{lab}\ \ 0 \quad (112)$$

$$\chi^{(2)}_{122}\mathrm{lab} = 0 \quad (113)$$

$$\chi^{(2)}_{123}\mathrm{lab} = 0 \quad (114)$$

$$\chi^{(2)}_{131}\mathrm{lab} = \cos\varphi^2\chi^{(2)}_{131} + \sin\varphi^2\chi^{(2)}_{232} \quad (115)$$

$$\chi^{(2)}_{132}\,\mathrm{lab} = 0 \quad (116)$$

$$\chi^{(2)}_{133}\,\mathrm{lab} = 0 \tag{117}$$

$$\chi^{(2)}_{211}\,\mathrm{lab} = 0 \tag{118}$$

$$\chi^{(2)}_{212}\,\mathrm{lab} = 0 \tag{119}$$

$$\chi^{(2)}_{213}\,\mathrm{lab} = 0 \tag{120}$$

$$\chi^{(2)}_{221}\,\mathrm{lab} = 0 \tag{121}$$

$$\chi^{(2)}_{222}\,\mathrm{lab} = 0 \tag{122}$$

$$\chi^{(2)}_{223}\,\mathrm{lab} = \sin\varphi^2\chi^{(2)}_{232} + \cos\varphi^2\chi^{(2)}_{232} \tag{123}$$

$$\chi^{(2)}_{231}\,\mathrm{lab} = 0 \tag{124}$$

$$\chi^{(2)}_{232}\,\mathrm{lab} = \sin\varphi^2\chi^{(2)}_{232} + \cos\varphi^2\chi^{(2)}_{232} \tag{125}$$

$$\chi^{(2)}_{233}\,\mathrm{lab} = 0 \tag{126}$$

$$\chi^{(2)}_{311}\,\mathrm{lab} = \cos\varphi^2\chi^{(2)}_{322} + \sin\varphi^2\chi^{(2)}_{322} \tag{127}$$

$$\chi^{(2)}_{312}\,\mathrm{lab} = 0 \tag{128}$$

$$\chi^{(2)}_{313}\,\mathrm{lab} = 0 \tag{129}$$

$$\chi^{(2)}_{321}\,\mathrm{lab} = 0 \tag{130}$$

$$\chi^{(2)}_{322}\,\mathrm{lab} = \sin\varphi^2\chi^{(2)}_{322} + \cos\varphi^2\chi^{(2)}_{322} \tag{131}$$

$$\chi^{(2)}_{323}\,\mathrm{lab} = 0 \tag{132}$$

$$\chi^{(2)}_{331}\,\mathrm{lab} = 0 \tag{133}$$

$$\chi^{(2)}_{332}\,\mathrm{lab} = 0 \tag{134}$$

$$\chi^{(2)}_{333}\,\mathrm{lab} = \chi^{(2)}_{333} \tag{135}$$

$$\begin{aligned}\left|e(2\varpi).\chi^{(2)}\!:e(\varpi)e(\varpi)\right|^2_{Pin/Pout} &= \Big|-2\mathrm{L}(2\omega)_{xx}\mathrm{L}(\omega)_{xx}\mathrm{L}(\omega)_{zz}\cos\theta^2\sin\theta\Big[\cos\varphi^2\chi^{(2)}_{232} + \sin\varphi^2\chi^{(2)}_{232}\Big] \\ &+ \mathrm{L}(2\omega)_{zz}\sin\theta\,\Big\{\mathrm{L}(\omega)_{xx}{}^2\cos\theta^2\Big[\cos\varphi^2\chi^{(2)}_{322} + \sin\varphi^2\chi^{(2)}_{322}\Big] \\ &+ \mathrm{L}(\omega)_{zz}{}^2\sin\theta^2\chi^{(2)}_{333}\Big\}\Big|^2\end{aligned} \tag{136}$$

$$\left|e(2\varpi).\chi^{(2)}\!:e(\varpi)e(\varpi)\right|^2_{Pin/Sout} = |0|^2 \tag{137}$$

$$\left|e(2\varpi).\chi^{(2)}:e(\varpi)e(\varpi)\right|^2_{Sin/Pout} = \left|\mathrm{L}(2\omega)_{zz}\mathrm{L}(\omega)_{yy}{}^2\sin\theta\left[\sin\varphi^2\chi^{(2)}_{322} + \cos\varphi^2\chi^{(2)}_{322}\right]\right|^2 \quad (138)$$

$$\left|e(2\varpi).\chi^{(2)}:e(\varpi)e(\varpi)\right|^2_{Sin/Sout} = |0|^2 \quad (139)$$

The $\left|e(2\varpi).\chi^{(2)}:e(\varpi)e(\varpi)\right|^2$ terms of $C_{\infty V}$ surface therefore can be expressed as shown in Eqs. (136) - (139).

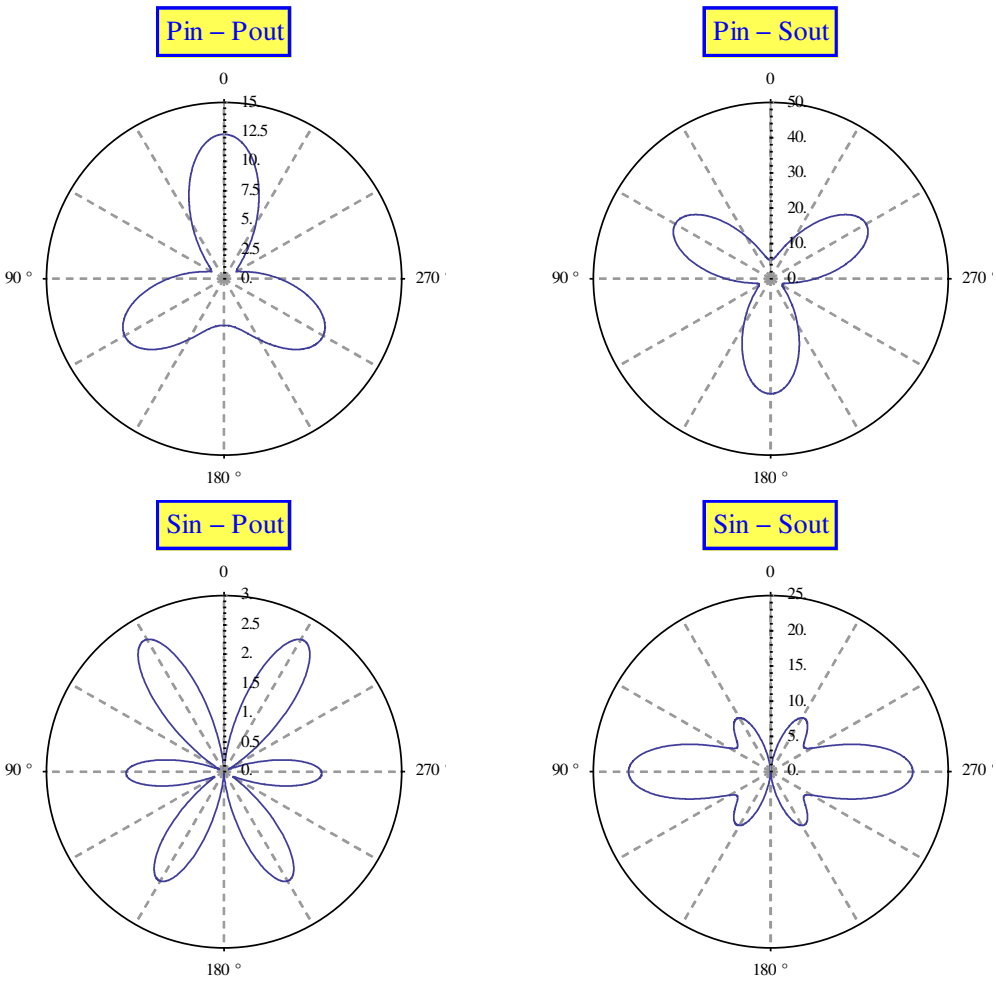

Fig. 2.15. Polar plots of $\left|\chi^{(2),\mathrm{eff}}\right|^2$ versus azimuthal angle φ for C_s surface at incident angle of 45°. The relative scale is an arbitrary unit. At zero degrees, the incident beam lies on the plane formed by directions 1 and 3 as shown in Fig. 2.11.

In order to visualize how $\left|e(2\varpi).\chi^{(2)}:e(\varpi)e(\varpi)\right|^2$ behaviors in azimuthal measurement, let us roughly perform a simple calculation to make it more transparent. Figure 2.15 illustrates $\left|e(2\varpi).\chi^{(2)}:e(\varpi)e(\varpi)\right|^2$ of C_s surface as a function of azimuth angle φ . The square of the absolute value of $e(2\varpi).\chi^{(2)}:e(\varpi)e(\varpi)$ was plotted in Pin/Pout, Pin/Sout, Sin/Pout, and Sin/Sout configurations. Here, I arbitrarily selected each $\chi_{ijk}^{(2)}$ element at a specific value. All local field factors were set equal to 1 and incident angle $\theta = 45^{o}$.

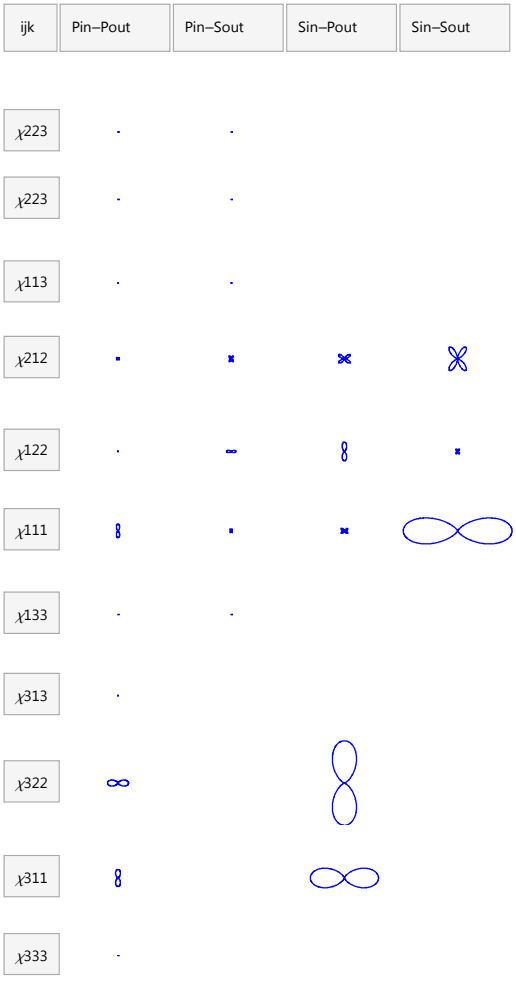

Fig. 2.16. Decomposition of $\left|e(2\varpi).\chi^{(2)}:e(\varpi)e(\varpi)\right|^2$ shown in Fig. 2.15 when one of the nonlinear susceptibility elements $\chi_{ijk}^{(2)}$ is set equal to a specific value and all the other elements are set equal to zero. The unit is arbitrary but on a common scale. ijk are the suffices of the nonlinear susceptibility elements.

Fig. 2.16 presents the decomposition of $\left|e(2\varpi).\chi^{(2)}\!:e(\varpi)e(\varpi)\right|^2$ shown Fig. 2.15 when one of the nonlinear susceptibility elements $\chi^{(2)}_{ijk}$ is set equal to a specific value and all the other elements are set equal to zero. The unit is arbitrary but on a common scale.

Generally, once I get the experimental data, the contribution of each nonlinear susceptibility elements could be estimated by adapting the observed data to the theoretical model over the fitting range of each data set. During this process, I attempted to minimize the total sum of the goodness of the fit parameter by a least-squares fitting program. That process will be dealt in Chapter 5. It should be aware that I expected to fit multiples measured curves (4 measured curves in Pin/Pout, Pin/Sout, Sin/Pout and Sin/Sout) simultaneously to the modeled functions with unknown nonlinear susceptibility elements are the shared parameters. Marquardt-Method [71] is the fast way to minimize the total sum of the goodness of the fit parameter. The measured curves in Pin/Pout, Pin/Sout, Sin/Pout, and Sin/Sout therefore can be fitted the model, respectively.

We should also visualize the strength of the surface SHG signal. To do that, I briefly estimated the number of SHG photon radiated per second [72],

$$S(2\omega) = \frac{\omega^2}{\varepsilon_0 \hbar c^3 cos\theta^2} \frac{P_{av}^2(\omega)}{t_p R_{rep} A_s} \left|e(2\varpi).\chi^{(2)}\!:e(\varpi)e(\varpi)\right|^2 \quad (140)$$

Where $P_{av}(\omega)$ is the average power in the incident beam, t_p is the pulse duration, R_{rep} is the repetition rate, and A_s is the irradiated area of the sample. By assuming the parameters as similar as the experimental condition used in Chapter 4, $P_{av}(\omega) = 30\,\mu W$, $t_p = 30\,ps$, $A_s = 0.785\,mm^2$, at the wavelength of 532 nm, the number of SHG photon is around 3302 photons per pulse. Here, all Fresnel factors were set equal to 1 and $\chi^{(2)}$ was set equal to that of quartz [73]. The rough result indicated the possibility in detecting SHG signal with photomultiplier.

CHAPTER 3

LITERATURE REVIEW

3.1. Electron beam lithography

In this section, I aim to summarize the general steps of nanofabrication using electron beam lithography as regarded in Refs. [74] and [75]. As I have known, electron beam lithography (EBL) is considered as a standard method to fabricate the nanostructure materials [12]. It is a flexible technique and can be used to tailor 2D structures with a resolution down to 10nm [74]. This is the process of manipulating an electron beam through a resist layer and making the desired patterns. Normally, it follows several steps as shown in Fig. 3.1.

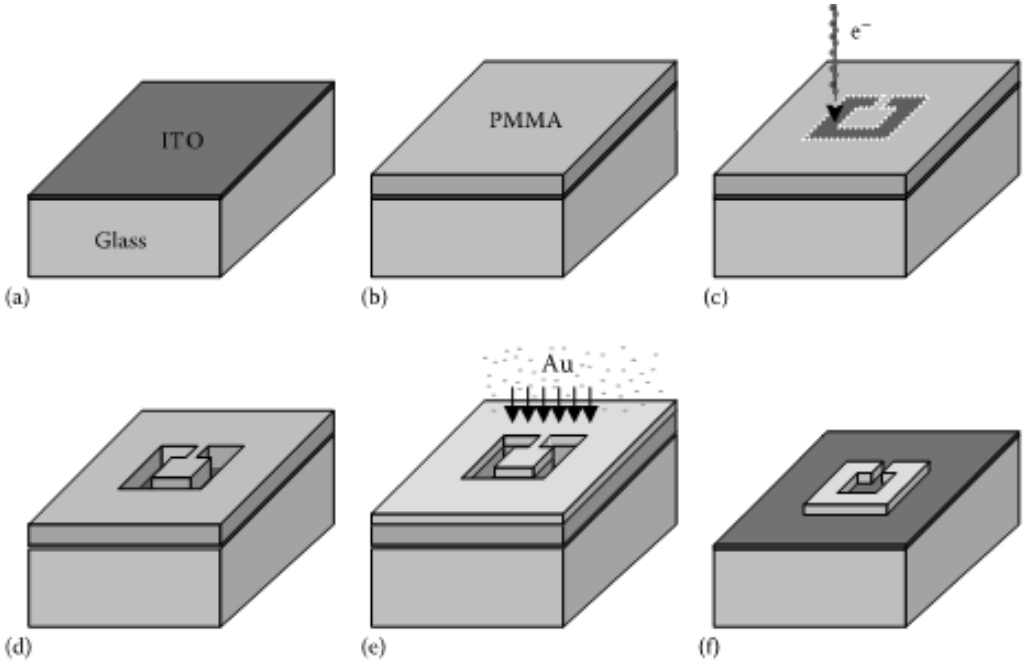

Fig. 3.1. Steps of a typical EBL run: (a) Deposition of ITO, (b) spin coating of PMMA, (c) electron-beam writing of the desired structure, (d) development, (e) evaporation of metal (e.g., gold), and (f) liftoff [74].

At first, the substrate is covered by a thin film of indium tin oxide (ITO) to avoid charging effect. In the next step, a resist layer, generally polymer organic materials (poly methyl methacrylate-PMMA) is spin coated onto the substrate. Following the spin coating process, a beam of electron is used to generate expected patterns into the resist. The parameters of e-beam energy are essential in making a high-resolution nanostructure. Here, a computer will control the e-beam to scan over the surface under an acceleration voltage. Since the beam width is approximately nanometers, a high resolution up to subwavelength is possible with this method. After that, the exposed resist will be removed by immersing the sample in a specific organic solvent. This is for positive resist. In the case of negative resist, instead of exposed region, non-exposed region will be dissolved. A mark therefore is formed after the exposed resist is removed. Then the metal evaporation will proceed for the subsequent process. Finally, the unexposed resist as well as the metal on the top of it is removed by chemical solution (acetone). Since final patterns will be strongly affected by the choice of resist, the exposure, and development process, the methodology of all processes have to be optimized [75].

Table 3.1. Summary of main charactersistics of electron beam lithography [75].

	Resists	Tone	Composition	Mw	Dose	Resolution	Thickness	Contrast
a-)	PMMA	Positive	Polymethyl-methacrilate	495 K–950 K	0,1 C/cm^2 at 25 kV	10 nm	30 nm	>4
b-)	ZEP-520	Positive		55000	30 μC/cm^2 at 20 kV	15 nm	120 nm	>4
c-)	Calixarene	Negative	MC6AOAc	972	7 mC/cm^2 at 50 kV	7 nm	30 nm	2.5
			CMC6AOMe	–	700 μC/cm^2 at 50 kV	–	30 nm	–
d-)	HSQ	Negative	Hydrogen Silsesquioxane	11000	5519 C/cm^2 at 50 KV	6 nm	20 nm	–
					300 μC/cm^2 at 70 kV	7 nm	100 nm	–

3.2. AFM measurement

Atomic force microscopy (AFM) is one of the methods of surface analysis. It can be used to probe the insulating surface as well as conducting samples. In principle, the AFM can map the sample surface by scanning a sharp tip over the surface of the sample. When the tip approaches close to the sample surface, the tip will interacts with the sample surface. Because the interaction between the tip and the surface changes by time, the cantilever feels some forces from the sample surface. Thus, deflections are formed in the cantilever. These deflections will be then detected by a laser beam and the optical signal from the back of the cantilever will be reflected onto a photodetector. The signal is used to map the image of the surface [76,77].

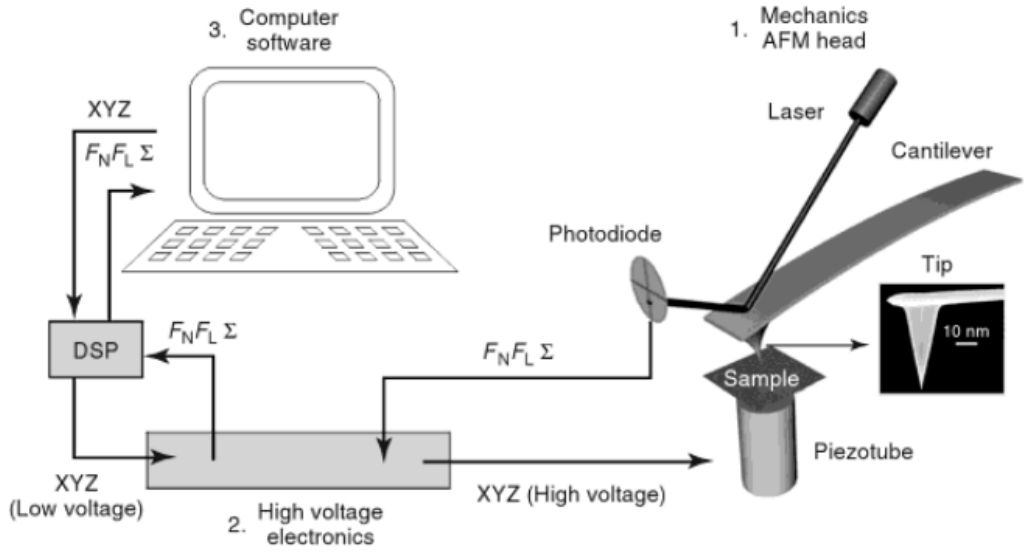

Fig. 3.2. Schematic diagram of atomic force microscopy [77].

Normally, the interaction forces between the tip and sample surface consist of Coulombic and van der Waals forces [77]. Roughly, one can schematize the forces between AFM tip and sample surface as Lennard–Jones potential [78] shown in Fig. 3.3. As the tip moves towards the sample surface, van der Waals forces results in the attraction. If the tip goes further and nearly touch the sample surface, the repulsive Coulombic forces

will enhance and cause the bending of the cantilever. There are also other interactions than Coulombic and van der Waals forces [76, 78].

In general, the AFM can operate under three main modes, contact, tapping, and non-contact modes. In the contact mode, during measurement, the cantilever can be vertical motion along the direction perpendicular to the sample surface or torsional motion. It is considered as the simple way to observe the topographic image. In the tapping and noncontact mode, the cantilever will oscillate close to its resonant frequency. However in the tapping mode the tip lightly touches the sample surface at the bottom of its swing while it truly does not tap the sample surface in non-contact mode [77,76,78,79].

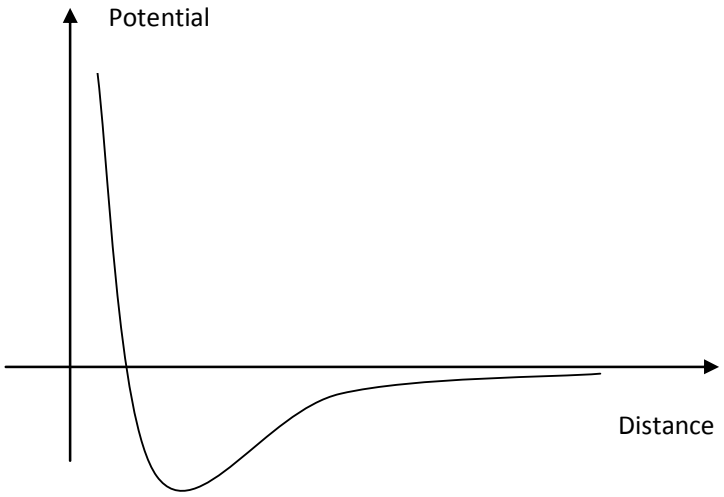

Fig. 3.3. The Lennard–Jones pair potential [77].

3.3. Non-plasmonic materials

Here I briefly give recent results reporting the advantage of plasmonic materials compared with non-plasmonic materials. In the effort of producing plasmonic nanolasers, W. Zhou et al. [80] found that the extinction peaks for Au and Ag (plasmonic material)

nanoparticals (NPs) array are much stronger than that for Ti and TiO_2 (non-plasmonic material) NP. Figure 3.4 show the 3D structure of nanaocavity array laser.

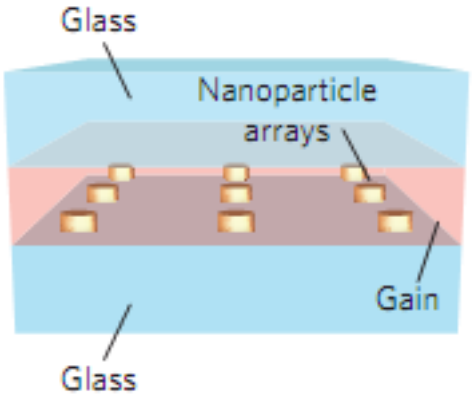

Fig.3.4. The nanocavity array laser. Here, two-dimensional arrays of nanoparticles could be Au or Ag (plasmonic material) and Ti or TiO_2 (non-plasmonic material). The NP was patterned on a glass substrate and then covered by a polymer gain layer composed of polyurethane and IR-140 dye [80].

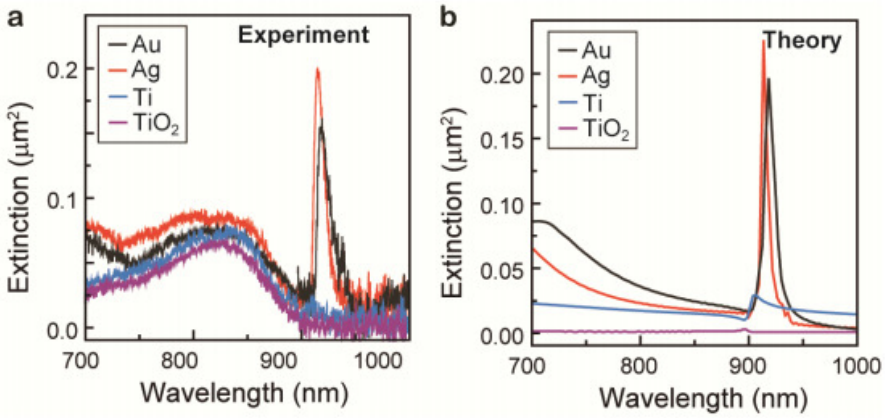

Fig. 3.5. a) Measured normal-incidence extinction spectra for 2D NP arrays of different materials (Au, Ag, Ti, TiO_2) surrounded by gain media. The broad peak around 820 nm in all samples corresponds to the absorption of IR-140 molecules. b) FDTD-calculated normal-incidence extinction spectra for 2D NP arrays of different materials (Au, Ag, Ti, TiO_2) without gain media [80].

We can see that the calculated extinction spectra for NP arrays of different materials were in good agreement with experiment as shown in Fig.3.5. Figure 3.6 shows the measured emission spectra of two-dimensional nanoparticle arrays of plasmonic and non-plasmonic materials (Au, Ag, Ti, TiO_2) with gain media at a pump pulse energy of 0.43 mJ cm^{-2} and measured output emission intensity as a function of input pump pulse energy. Obviously, the Au and Ag NP arrays emerge with narrow emission peaks as well as directional lasing emission at specific threshold pumps, while Ti and TiO_2 NP arrays only present a broad spontaneous emission even if a strong pump was introduced.

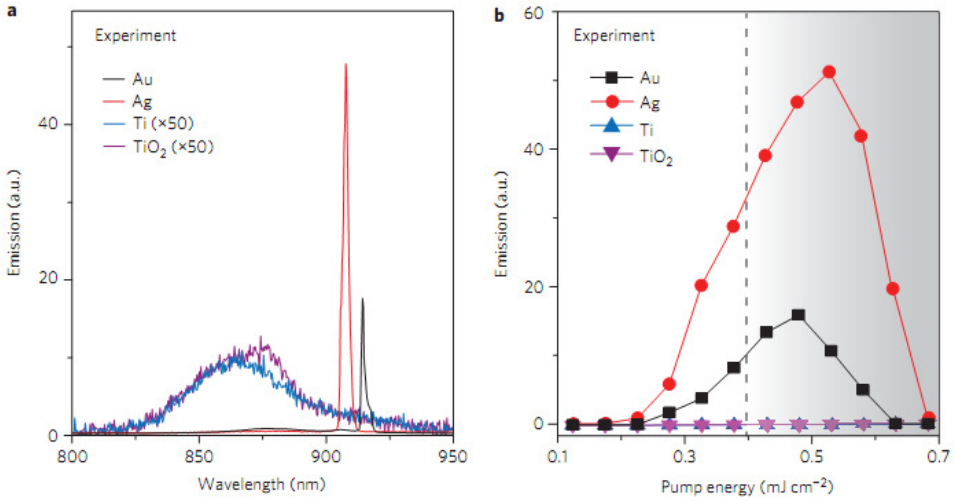

Fig. 3.6. a) Measured normal-incidence extinction spectra for 2D NP arrays of different materials (Au, Ag, Ti, TiO_2) surrounded by gain media. The broad peak around 820 nm in all samples corresponds to the absorption of IR-140 molecules. b) FDTD-calculated normal-incidence extinction spectra for 2D NP arrays of different materials (Au, Ag, Ti, TiO_2) without gain media [80].

In another work performed by J. Stadler [81], they found the strong enhancement of the signal in tip-enhanced Raman spectroscopy (TERS). Experimentally, Thiophenol was covered on several metal substrate and Ag tip was used to detect the TERS signal. The result was shown in Fig. 3.7. We can clearly observe the enlargement of TERS on Ag substrate whereas Ni and Al substrate did not give a strong signal. Another substrate including nonplasmonic material was used to investigate the TERS signal. The results

indicate that TERS signal intensity decreases by a factor of 10 with nonplasmonic substrates [81,82].

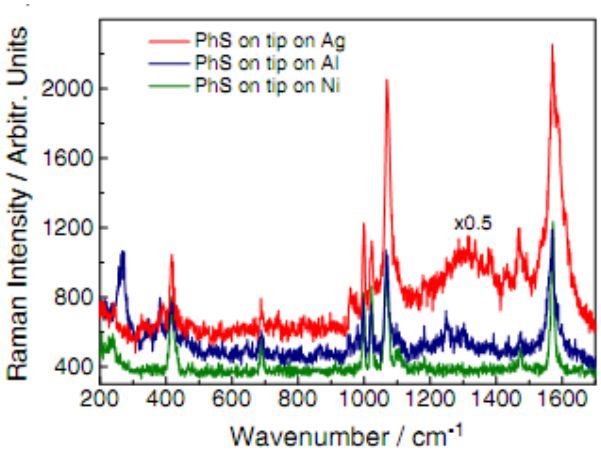

Fig. 3.7. Tip on Ag (red), Ni (green), and Al (blue), all showing clear signatures of Thiophenol (PhS) from the self-assembled monolayers on the tip. Intensities differ due to different enhancements of the tips in use for the respective experiment [81].

3.4. Nonlinear plasmonic of metamaterials

As mentioned in Chapter 1, although photonics itself has many advantages in solving the issues of high-speed performance of integrated circuits, the appearance of plasmonics has further unified the advantages of photonics and electronics. One of the main features of plasmonics is the fact that it could locally enhance the intensity of electromagnetic fields and therefore it creates many associated effects. Once the incoming electric field energy concentrates into subwavelength scales, the local electric field strength can thus be larger than the incoming field strength by orders of magnitude [50]. This would lead to a fascinating effect, nonlinear optical response. These nonlinear optical effects in plasmonic structures consisting of arrays of NP or nano-apertures will be reviewed in this section.

SHG resulting from the interaction between metallic structures and strong electric field is particularly interesting since it is sensitive to the changes of the metallic surface properties down to nanoscale. The first example of a designed surface is the plasmonic G-shaped structures shown in Fig. 3.8(a). Figures 3.8 (b) and (c) show the geometry of the G-

shaped and mirror-G-shaped nanostructures, respectively. The substrate consists of a single crystalline Si layer covered by a 100-nm-thick SiO_2 layer. 3-nm-thick Ti film was firstly deposited as an adhesion layer before the Au structures having a thickness of 25 nm are grown on top of the substrate. For more details, one can refer to Ref. [9,50]. SHG microscopy images are collected with a confocal laser-scanning microscope with a fundamental excitation wavelength of 800 nm.

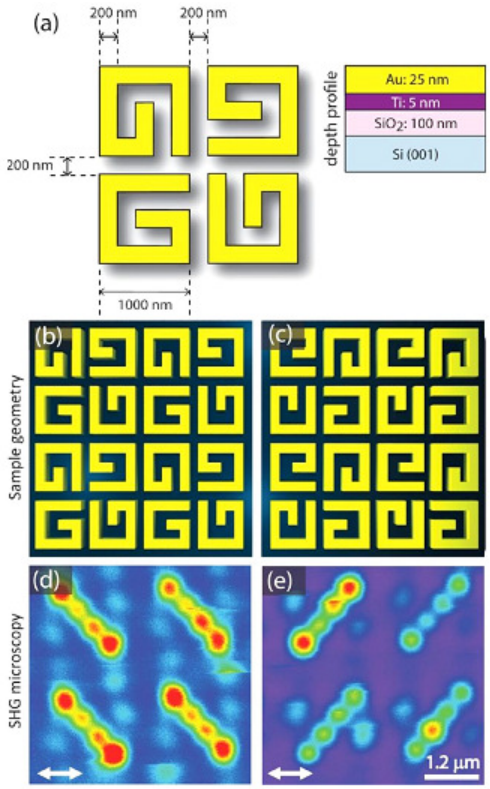

Fig. 3.8. Rather than showing a G-shaped signal, the SHG microscopy reveals a pattern of clearly defined hot spots. (a) The dimensions and depth profile of the nanostructures are presented. The four G-shaped nanostructures are arranged into a unit cell. Schematic diagrams of the (b) G-shaped and (c) mirror-G-shaped periodic arrays. The corresponding SHG microscopy images are shown in (d) and (e), respectively. The white arrows indicate the direction of the linear polarization. The color-coded intensities increase from purple, following the rainbow order of colors [9].

Figure 3.8(d) shows the SHG microscopy resulting from the array of G-shaped nanostructures. The polarization of incident light is shown with a white arrow. We can see that there are four regions of highly intense second harmonic sources, or "hot spots", along the main diagonal of the unit cells. Interestingly, this pattern of hot spots is mirrored owing to the array of mirror-G-shaped nanostructures (see Fig. 3.8(e)). The four hot spots are quite large and difficult to distinguish their location on the sample. The numerical simulations were therefore performed.

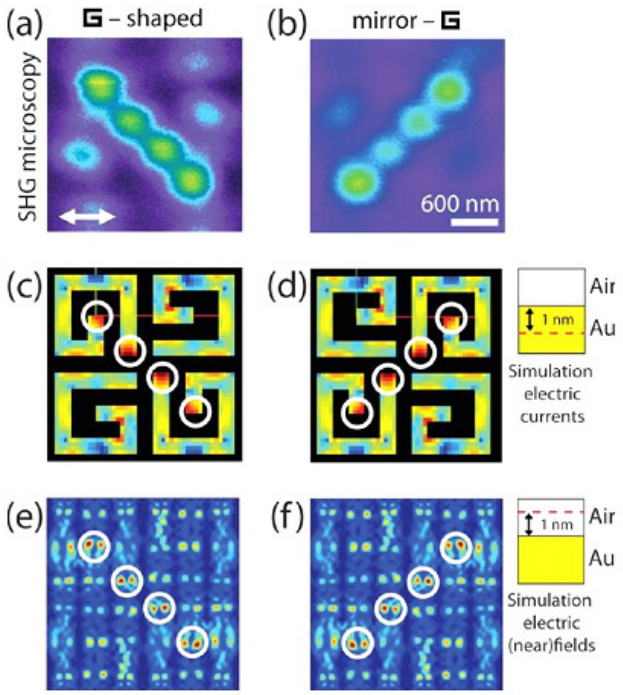

Fig. 3.9. The pattern of experimentally recorded second harmonic hot spots matches the pattern of numerically simulated local field enhancements at the fundamental frequency. (a,b) SHG microscopy (400 nm) from a unit cell of G-shaped and mirror-G-shaped nanostructures, respectively. The direction of light polarization is indicated with a white arrow. (c, d) Corresponding numerical simulations of the electric currents at the fundamental frequency (800 nm), recorded 1 nm below the air/gold interface. (e, f) Numerical simulations of the electric (near-) fields at the fundamental frequency (800 nm) recorded 1 nm above the air/gold interface. The color-coded intensities in all panels follow the rainbow order. In the numerical simulations, the regions of highest intensity have been highlighted with white circles [9].

Figure 3.9 (a) and (b) show the SHG microscopy images for the unit cells of G-shaped and mirror-G-shaped gold nanostructures, respectively. Figure 3.9 (c) and 3.9(d) show the electric current in the nanostructures calculated at 1 nm below the air/gold interface. The electric near-field was calculated at 1 nm above the air/gold interface (Figure 3.9 (e)-(f)). The result shows that the pattern of second harmonic hot spots matches the pattern of local electric current and electric near field enhancements at the fundamental wavelength. The physical mechanism of the origin of SHG hot spots in near field enhancements was attributed to the plasmonic hot spots. Both the surface (electric dipoles) and the bulk contributions (magnetic dipoles, electric quadrupoles, etc.) conduce to the SHG intensity [50].

Another pioneering work was done by Canfiled et al. [83] with L-shaped NPs structure. They performed detailed in-plane polarization dependence of the SHG response. A completed NP consists of a Cr adhesion layer 2 nm and 20 nm of gold. The NP arrays lie on a glass substrate. The NPs are then covered by a protective glass layer of 20 nm. In this work, they created many arrays with different sized particles, grating spacings, or even particle orientations as shown in Table 3.2.

Table 3.2. Sample parameters for nanoparticle arrays [83].

Sample	Orientation	Constant (nm)	Variable	Variations (nm)
S1	Standard	Spacing (400)	Size	170, 190, 220, 240, 260, 300
S2	Standard	Size (200)	Spacing	300, 400, 500
S3	Standard	Size (200)	Spacing	350, 450, 550, 650, 750
S4	Rotated	Size (200)	Spacing	350, 450, 550, 650, 750

Figure 3.10(a) illustrates a sample array with ‘standard’ lattice orientation, while Fig. 3.10(b) shows how the sample was rotated by 45^{o} with respect to the array lattice points. Figure 3.10(c) shows a scanning electron micrograph (SEM) image of standard orientation gold nanoparticles. The SHG response emerged several interesting behaviors of the symmetry of the L-shaped particles.

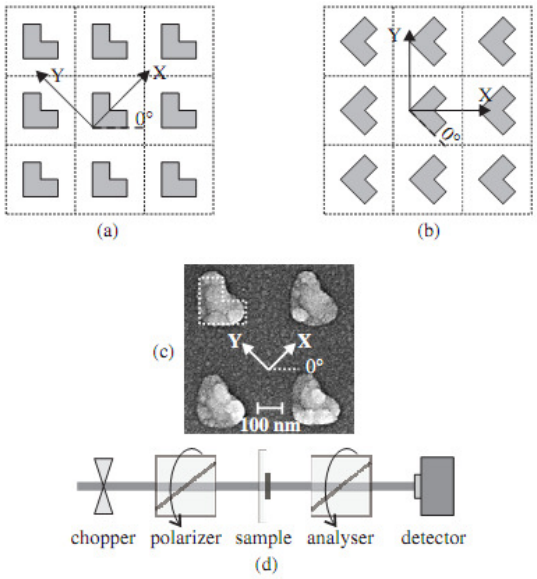

Fig. 3.10. The structure of samples: (a) a standard orientation NP sample; (b) a rotated orientation sample; (c) an SEM image of nanoparticles; (d) the core of the experimental apparatus [83].

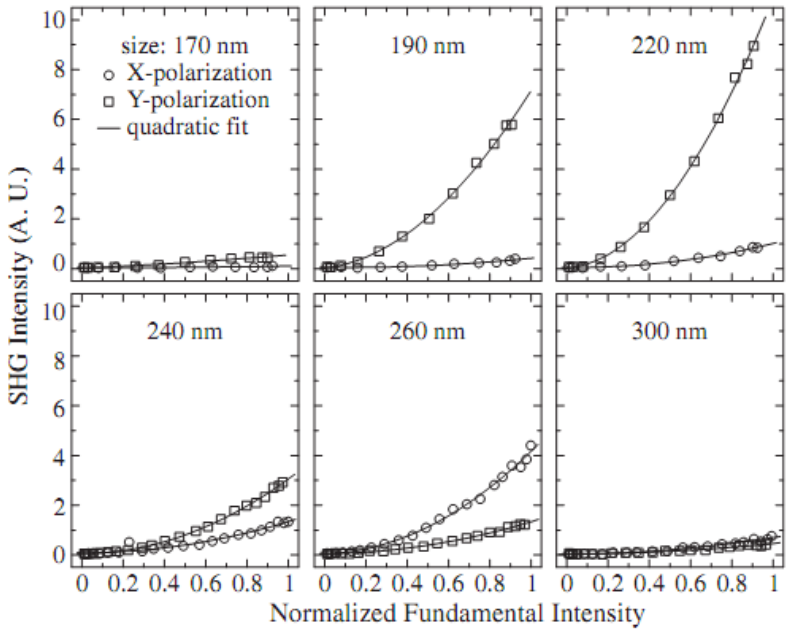

Fig. 3.11. SHG signal polarization responses and quadratic fit curves for the arrays of sample S1 [83].

They investigated the SHG response without the analyzer in Fig. 3.10(d) and the fundamental wavelength was set equal to 1060 nm. The results for all six arrays of sample S1 are shown in Fig. 3.11. One can see that the SHG responses appear to reflect the extinction resonance locations in Table 3.3. The arrays with 260 and 220 nm-size have the resonance peaks at 1045 nm and 1070 nm, respectively. We can see that these peaks are close to the laser line, therefore we can observe the enhancement of the SHG intensity while it decreased for other sizes.

Table 3.3. Approximate (±5nm) wavelengths of maximum extinction for arrays from sample S1 [83].

Size (nm)	*X* peak (nm)	*Y* peak (nm)
170	805	980
190	855	1030
220	920	1070
240	960	1100
260	1045	—[a]
300	1085	—[a]

[a] Beyond the spectrometer range.

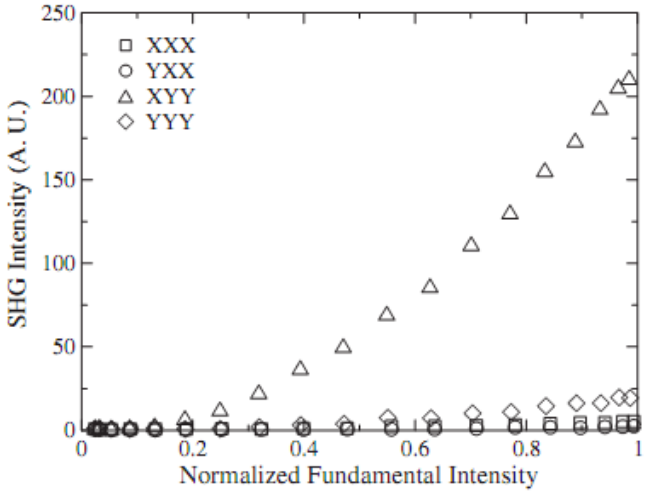

Fig. 3.12. The polarization dependence of the SHG for the 190 nm-size particle array [83].

One of the most interesting is the investigation of in-plane nonlinear susceptibility elements. They obtained the SHG response of the sample with 190-nm-size of the sample S1. The nonlinear responses are shown in Fig. 3.12. The most impressive result is that the YYY combination is not only non-zero, but also comparable to the allowed XXX combination. In general, it should be zero under broken symmetry condition for the ideal case. The 'forbidden' YYY component is large (about 10% of the allowed, resonant XYY signal) and is a good indication of symmetry breaking due to the smallest imperfection of the nanostructure.

Among artificial nanostructures, nanohole arrays also exhibit many interesting features in terms of nonlinear optics [10,27,40,49,84,85]. The main result of Airola and co-workers [84] are shown in Figs. 3.13 and 3.14. They showed an enhancement of the transmitted second harmonic generation (SHG) signal in a periodic circular nanohole array owing to the enhanced transmission of the incident light. They considered two possible sources for the SHG signal. The first is direct from the apertures. Here, the apertures serve as a coherent array of point sources for second harmonic emission. The second contribution to the observed second harmonic could be resulted from a surface plasmon wave at the second harmonic frequency.

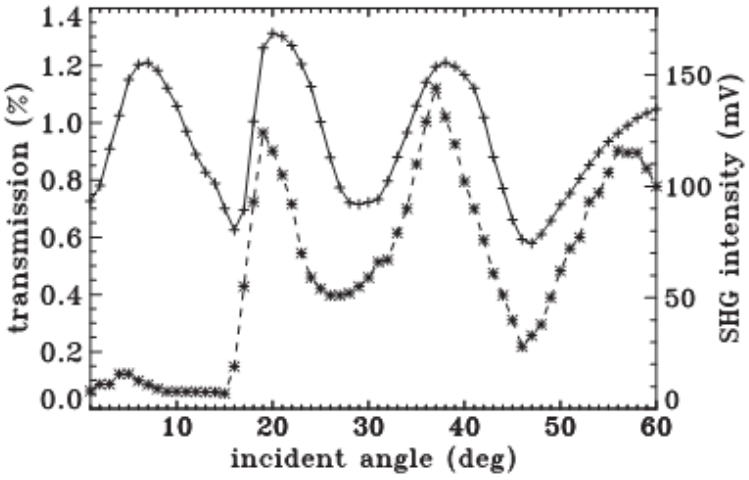

Fig. 3.13. The generated second-harmonic signal in transmission (data points indicated by '∗') and transmission of the fundamental (data points indicated by '+') through a periodic array of circular apertures with 225 nm diameter and 1.1 μm spacing [84].

They also found an enhanced SHG signal from disordered circular gold nanohole arrays compared with periodic arrays. The explanation is that the disorder induces a large macroscopic $\chi^{(2)}$, where the increase in the overall second order susceptibility is more than compensation for the reduction in driving field.

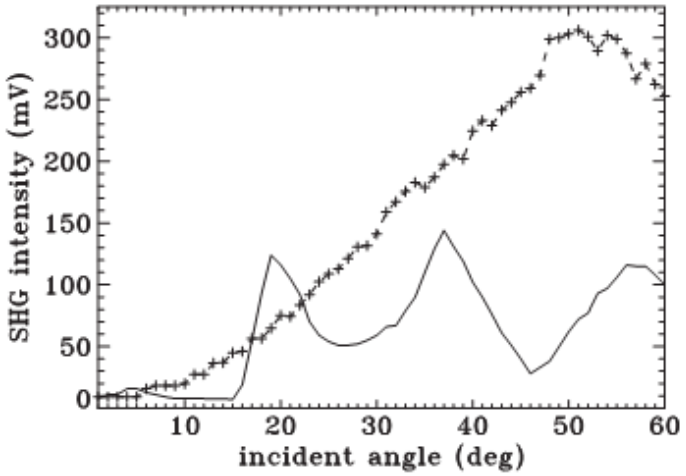

Fig. 3.14. The second-harmonic output for the disordered (data points indicated by '+') and periodic (data indicated by a continuous curve) arrays [84].

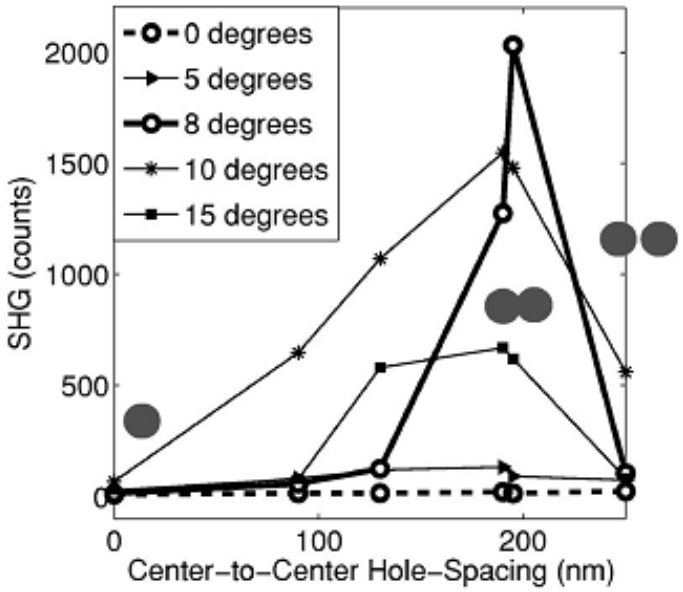

Fig. 3.15. Angle-dependent SHG measurements as a function of center-to-center hole spacing. d=0 nm corresponds to a circular shape while the d=250 nm consists in two holes separated by a gap of 50 nm. The array periodicity was 750 nm [27].

More recently, it has been found that the overlapping of two circular holes induced an enhancement of SHG by as much as 14 times compared with circular holes owing to a strong local field at the sharp apexes inside the overlapping holes [27,86]. Here, array of double-holes was milled by a focused ion beam through a 100 nm thick gold layer with a 5 nm Cr adhesion layer on a glass substrate.

Figure 3.15 shows the angular dependent SHG measurements versus the center-to-center hole spacing. The general trend of this figure is that when the holes are nearly overlapping with sharp apexes, they produce the greatest SHG signal. The SHG signal was maximized for an angle of 8°. In the FDTD calculations shown in Fig. 3.16, the y polarization gives the strong field enhancement for both the fundamental and second harmonic wavelengths, whereas the x polarization gives no enhancement.

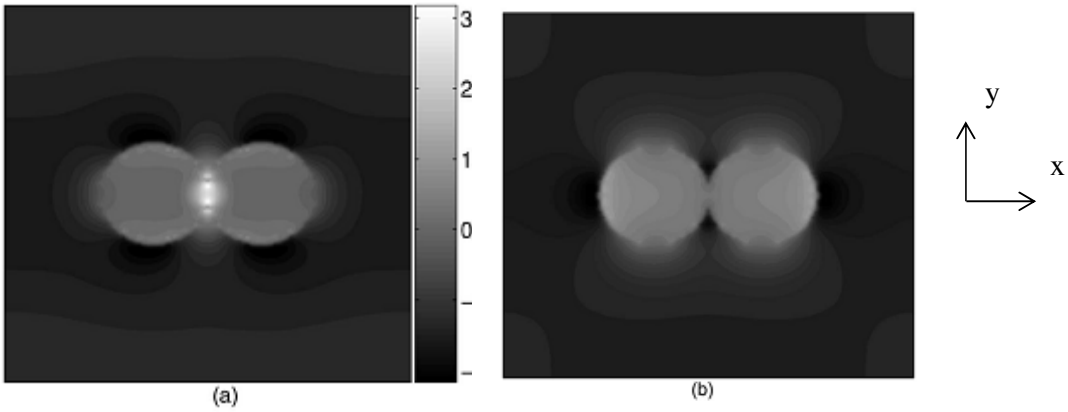

Fig. 3.16. FDTD calculation of natural logarithm of electric field from double-hole structure with apexes for a 750 nm periodicity with an incident beam polarized along (a) the y direction and (b) the x direction. The colormap is the same for both figures [27].

An exception is the work on rectangular apertures done by Nieuwstadt et al. [10]. Here, the holes are milled in an optically thick Au film (thickness 160 nm) on a glass substrate (see Fig. 3.17). By investigating arrays with different hole shapes, they found that a ‘‘hot’’ hole shape exhibit the SHG enhancement by more than 1 order of magnitude for

one particular aspect ratio. The result is shown in Fig. 3.18. This enhancement was attributed to slow propagation of the fundamental wavelength through the holes.

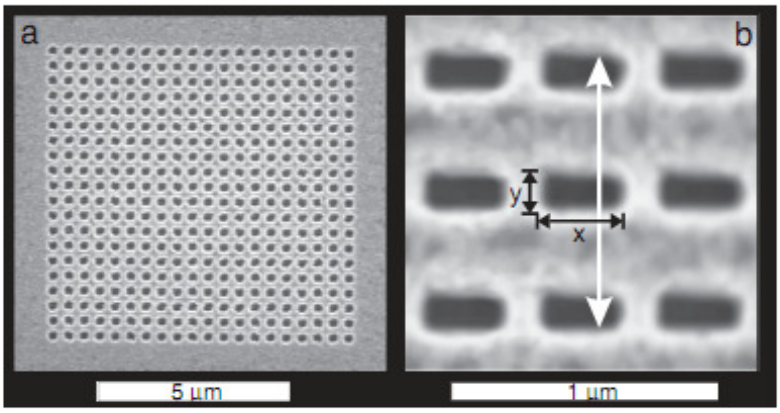

Fig. 3.17. (a) Scanning electron microscope (SEM) micrograph of an array of square holes. (b) SEM micrograph of an array with aspect ration (AR)= x/y = 2.0, where x and y (black arrows) are defined as the hole dimensions perpendicular and parallel to the polarization of the incident light (white arrow), respectively.

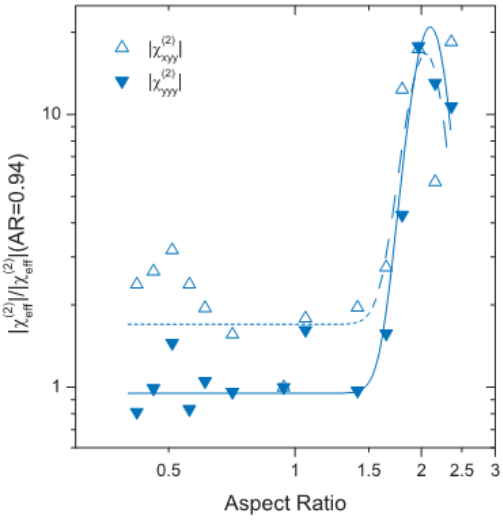

Fig. 3.18. Double-log plot of the normalized effective nonlinear susceptibility $\left|\chi^{(2)}_{ijk}\right|$ as a function of the aspect ratio. $\left|\chi^{(2)}_{yyy}\right|$ (solid triangles) and $\left|\chi^{(2)}_{xyy}\right|$ (open triangles) correspond to SHG with y and x polarization, respectively, both with the fundamental polarized along y. The lines are guides to the eye [10].

It should be noted that in these studies role of the local surface and nonlocal bulk contribution was incorporated into the total SHG signal since in the case of metallic nanomaterials, the separation would be more complicated [50, 87]. Obviously, the origin of the nonlinearity might vary when changing the studied systems. Additionally, the SHG response strongly depends on the designed nanostructure.

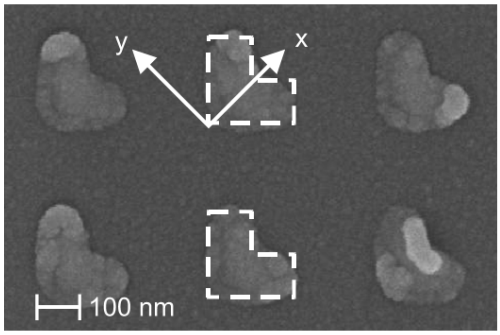

Fig. 3.19. Scanning electron micrograph of the sample with the principal axes marked [88].

The recent achievement done by M. Zdanowicz and his coworkers has proved the evidence of the significant contribution of higher multipole effects [88]. Their sample consisted of an array of L-shaped gold nanoparticles as shown in Fig. 3.19. The active area of the sample is as much as 1mm^2. By extending the macroscopic nonlinear response tensor approach, they accounted for the electric dipole and higher multipole effects.

Table 3.4. Determined values of nonlinear susceptibility tensor components [88].

NRT element	Value	Magnitude
A_{xxx}^{eee}	1	1
A_{xxy}^{eem}	$-0.239+0.408\text{i}$	0.473
A_{yxx}^{mee}	$0.034+0.041\text{i}$	0.054
A_{xyy}^{eee}	$0.794+0.063\text{i}$	0.797
A_{xyx}^{eem}	$0.233-0.315\text{i}$	0.392
A_{yyy}^{mee}	$0.012-0.033\text{i}$	0.035
A_{xxy}^{eee}	$0.199-0.086\text{i}$	0.217
$(A_{xyy}^{eem}-A_{xxx}^{eem})$	$0.438+0.137\text{i}$	0.459
A_{yxy}^{mee}	$0.003+0.007\text{i}$	0.007

The solution of nonlinear susceptibility tensors is shown in Table 3.3 where the values have been normalized to the electric-dipole-allowed component A_{xxx}^{eee}. Here A_{ijk}^{eee}, A_{ijk}^{mee} and A_{ijk}^{eem} tensors account for the electric dipole, magnetic dipole and electric quadrupole, respectively. It should be noted that in their calculation, the electric quadrupole effects were included in the magnetic tensors A_{ijk}^{mee} and A_{ijk}^{eem}. One can see that the nonlinear susceptibility tensors indicated the higher-multipole contribution were up to 50% in magnitude compared to the electric-dipole one [89].

CHAPTER 4

V-SHAPED NANOHOLE ARRAYS' FABRICATION TECHNOLOGY AND MEASUREMENT METHOD

4.1. V-shaped nanohole arrays' fabrication process

The silica substrate was first coated with 15 nm Cr by evaporation and then cut into small pieces of 12 x 12mm^2 . The sample was then spin-coated with a 40 nm e-beam resist and patterned by e-beam lithography using a 100 keV acceleration voltage, a 200 pA beam current, and a dose of 150 μC/cm^2. After resist development, the patterns were then transferred to Cr using dry etch processes before removing the resist completely. In the flowchart illustrated in Fig. 4.1 and 4.2, the basic steps of V-shaped nanohole structure fabricated by electron beam lithography are shown.

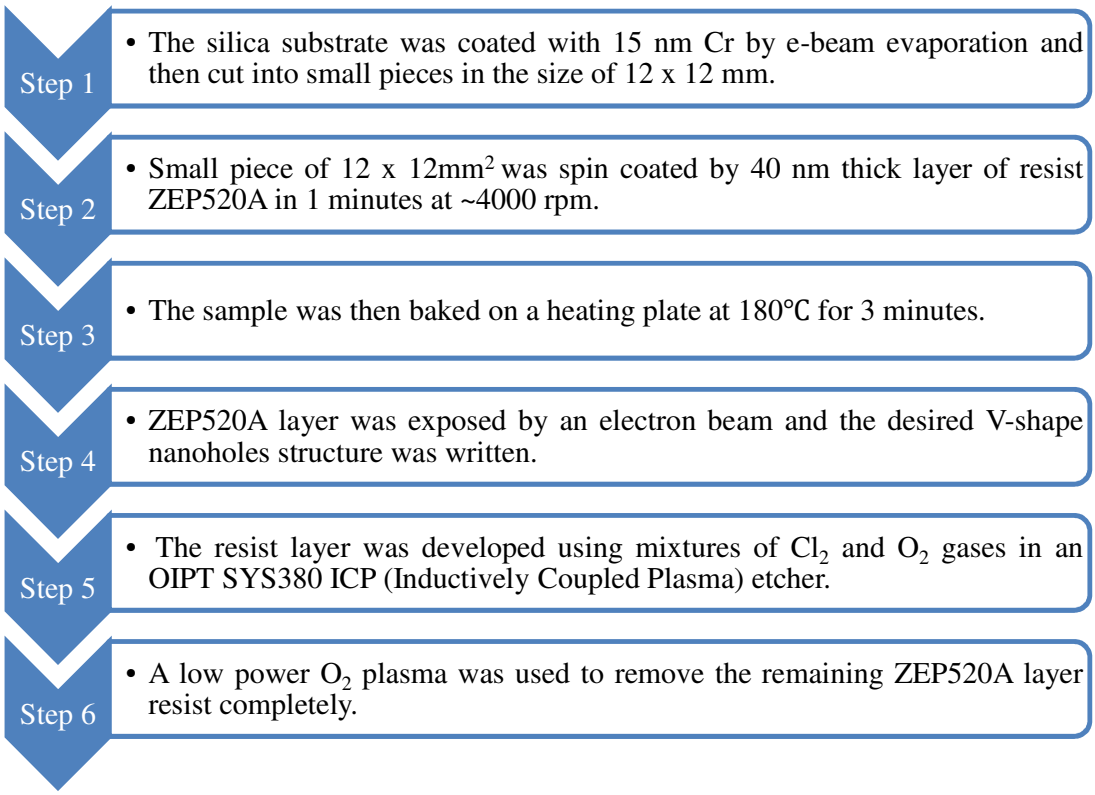

Fig. 4.1. Flowchart of fabircation process.

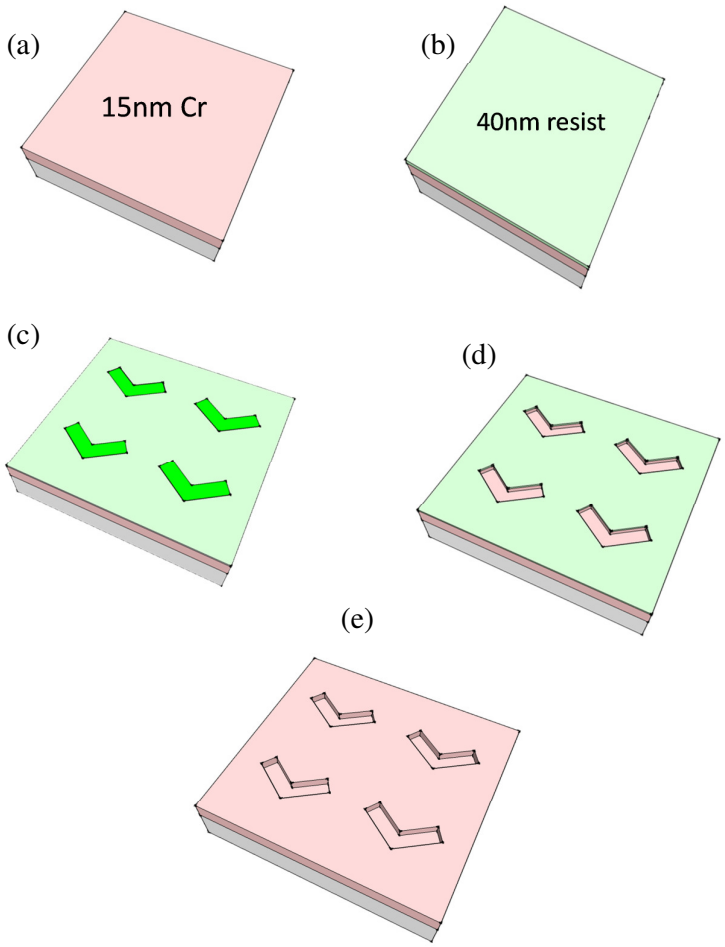

Fig. 4.2. Fabrication steps of electron beam lithography: (a) evaporation of 15 nm Cr on silica substrate, (b) spin-coating with a 40 nm ZEP520A e-beam resist, (c) pattern V shape by e-beam lithography (JEOL JBX-9300FS) using the condition of 100 keV acceleration voltage, 200 pA beam current, and dose of 150 $\mu C/cm^2$, (d) transfer V-shape pattern into Cr by dry etch processes using mixtures of Cl_2 and O_2 gases in an OIPT SYS380 ICP (Inductively Coupled Plasma) etcher, and (e) e-beam resist is completely removed by low power O_2 plasma.

It shoud be noted that the samples were fabricated in collaboration with University of Southampton, UK. This work was dealt by one of my co-worker, Dr. Ruiqi Chen. Without my co-workers' support, most of my experiments were impossible.

4.2. Surface second harmonic generation

As the excitation source of the SHG signal from the sample, I used the second harmonic denoted ω of a mode-locked Nd:YAG picosecond laser. Its output pulse width was 30 ps and the repetition rate was 10Hz. For measuring the azimuthal angle dependence of the SHG, the sample was mounted on an automatic rotation stage. The incident polarized light at the photon energy of 2.33 eV illuminated the V-shaped area at an angle of 45° with respect to the surface normal. Direction 3 is defined as the direction normal to the surface while directions 1 and 2 are on the sample surface. 1 indicates the direction of the bisector of the V passing through its apex in the substrate plane. Azimuthal angle φ is defined as the angle between the incident plane and direction 1. At 0^{o}, the fundamental light first illuminates the nanohole arrays at the valley between the two arms of the V-shaped structure. The inset at the center of Fig. 5.4 illustrates the relative position between the incident plane and direction 1.

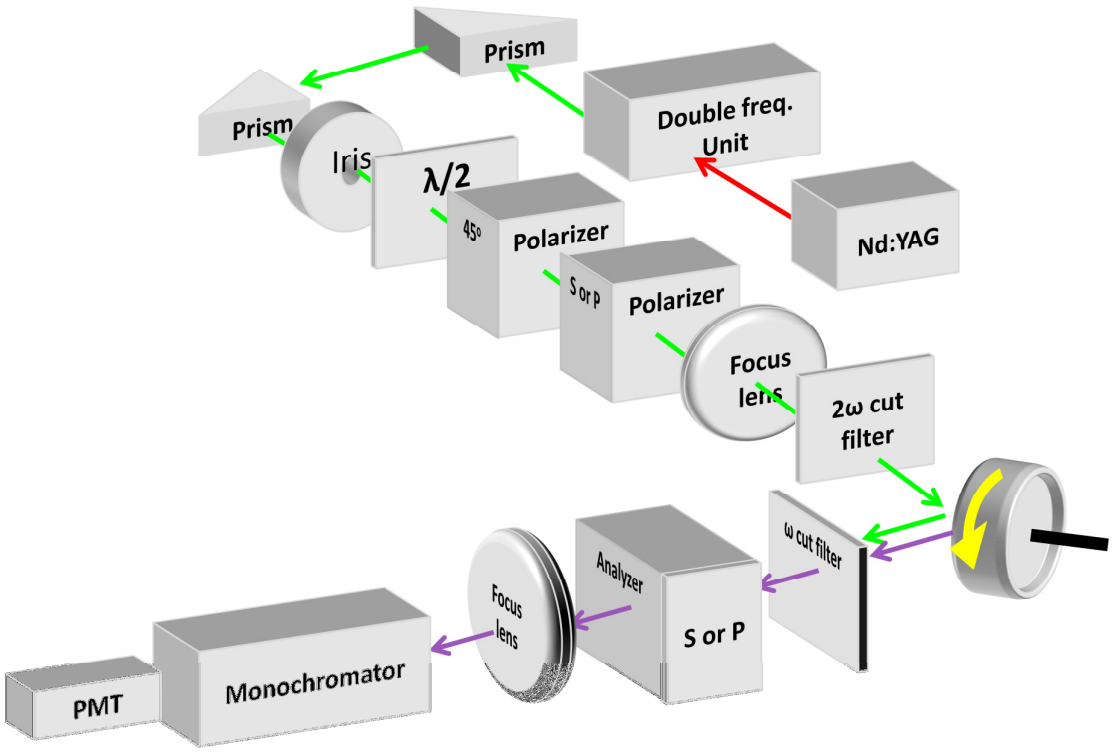

Fig. 4.3. Illustration of the SHG experimental setup.

After passing through a polarizer, a focusing lens, and a 2ω cut filter, a laser spot of 1mm diameter was focused on the V-shaped area. To ensure that the laser beam always illuminated the V-shaped nanoholes during the rotation of the stage, care was taken that both the laser spot and the V-shaped area were on the rotation axis (see Figs. 4.4 and 4.5). In order to ensure that the laser beam always impinges the sample surface at the same position during rotation of stage, I carefully found rotational axis of stage. A bottom-up stage cross section consists of a big-two axes stage, a rotation stage, and a small-two axes stage. First, by rotating the sample though four positions, I can easily find the rotation axis of the system where it is the intersection of the two diagonals in the rectangle. By exploiting the big-two axes stage, I can easily move the rotation axis toward the position where the laser spot hit on the sample surface. Then I can freely choose any array located on the sample to measure using the small-two axes stage. It took nearly one year to find and master this technique, I am very happy if you would say an acknowledgement to me when you use this setup in your experiment. Then, I deliberately focused the laser spot on the position where sample surface and rotation axis intersect together. The V-shaped domain was then shifted toward the laser spot position. To avoid damaging the sample, the average energy of the incoming beam was kept at about 30 μJ/pulse. The reflected radiation at the doubled frequency 2ω was passed through an ω cut filter, an analyzer, and a focus lens and was finally detected by a photomultiplier through a monochromator. SHG signals for 10^4 laser shots were accumulated for each data point in Fig. 5.4. All measurements were carried out at room temperature and in air.

.

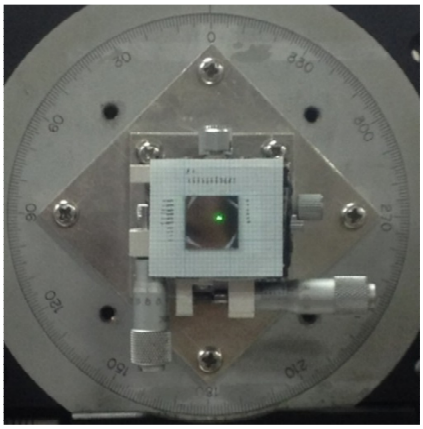

Fig. 4.4. Sample was mounted on a automatic rotation stage and a scale paper was used to estimate the arrays of V-shaped nanoholes.

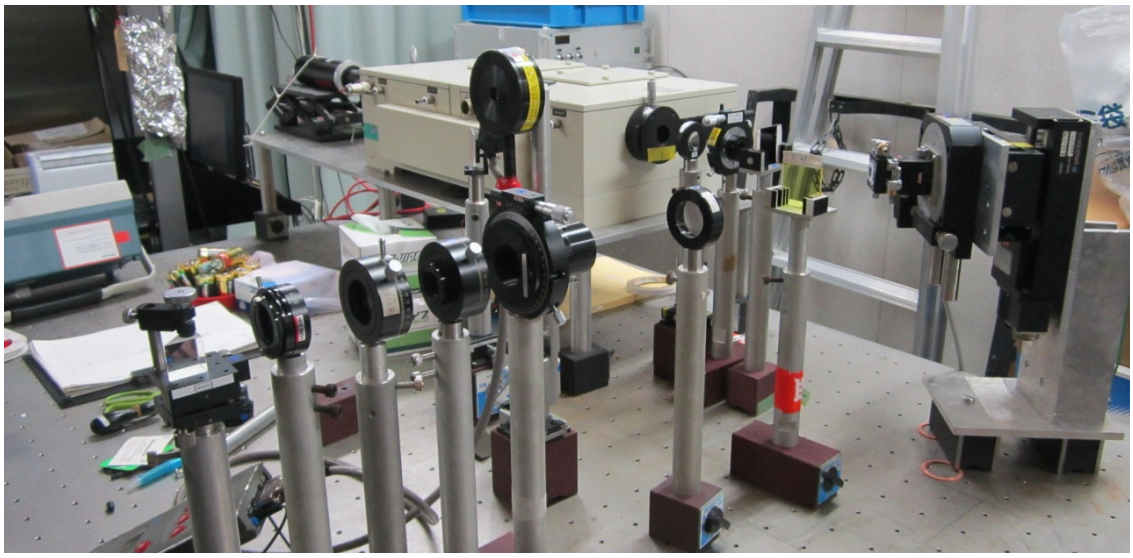

Fig. 4.5. Experimental apparatus used during azimuthal angle dependence measurement.

CHAPTER 5

RESULTS AND DISCUSSION

5.1. AFM observation of V-shaped nanohole arrays

V-shaped nanohole arrays was observed by using Atomic Force Microscopy (AFM, VN-8000; Keyence Instruments, Inc.). AFM image analysis was performed with the VN-Viewer analysis program. All images were analyzed with tapping mode using a silicon tip (DFM/SS Mode Cantilever-NPX1CTP004). Since a digital microscope is integrated into the AFM machine, I can easily define the zone where V-shaped nanoholes are located. I started the observation from a wide field of view. The optical microscope of the V-shaped array named R04C08 is shown in Fig. 5.1. The AFM equipment (KEYENCE VN-8000) used has a tip radius of curvature ~20 nm. AFM's resolution suggested to be the same order as this radius may have added the blur into the edges and corners of the V-shaped images.

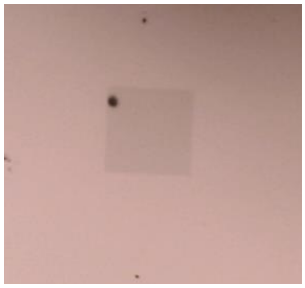

Fig. 5.1. Optical microscope image of the array named R04C8.

I also tried to observe the sample with SEM, the obtained images, however, is very obscure. At room temperature, the resistivity of chromium is ~one order of magnitude larger than that of copper [90]. Furthermore, calculating the resistivity of 15-nm-thick Cr film gives the value as much as 1.83×10^4 Ω nm. Because of its high resistivity, the charge up effect might cause the failure when I obtained the SEM image.

Here, the V-shaped apertures of the V-shaped arrays named R04C08 are schematically depicted in Fig. 5.2(a). The V-shaped apertures are 150 nm in length and 50

nm wide, have a 360 nm periodicity, and the angle of the apex is 120°. Indeed, V-shaped structural parameters such as arm length, arm width, apex angle, and periodicity were modified to probe the SHG response. The V-shaped nanohole structural parameters used in Fig. 5.2 produced the strongest anisotropic behavior in second harmonic generation response. The whole array covered an area of about 100 μm^2. An atomic force microscopy image of the fabricated structures is shown in Fig. 5.2(b).

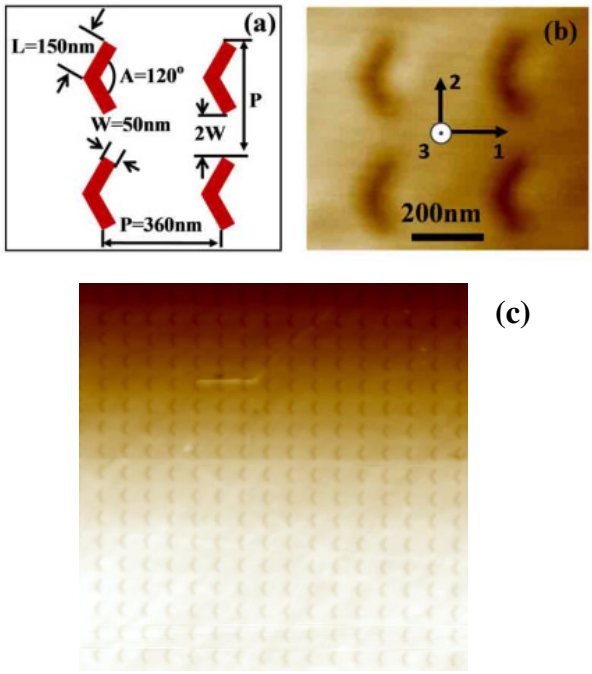

Fig. 5.2. Structure of V-shaped subwavelength nanohole array: (a) scheme of the designed parameters, (b) atomic force microscopy image, and (c) V-shaped nanoholes with 6μm scan area.

In section 5.2, I will attempt to examine the dependence of the SHG response on the structural parameters of V-shaped chromium nanoholes. Thus, three sets of the V-shaped nanoholes were fabricated. All arrays of V-shaped nanoholes were fabricated by electron beam lithography and are shown in Fig. 5.3. The apex angle A was set as 60°, 90°, or 120°. Since SHG intensity is sensitive to the broken symmetry, straining the V-shaped nanoholes until it becomes a straight rectangular hole is not my strategy. The apex angle was thus limited at 120° to keep the basic noncentrosymmetry of the V shape. The arm width W was 50nm. For each value of A, I fabricated nanoholes with arm lengths L = 2W,

3W, and 4W. All the arrays were created in a 15-nm-thick Cr film in the same batch to minimize the variation of the condition in the fabrication process. Each array covered an area of about 100μm^2. Atomic force microscopy images of the fabricated structures are shown in Figs. 5.3(b)-5.3(j). The arrays was named as R04C01 for (b), R04C02 for (c), R04C03 for (d), R04C04 for (e), R04C05 for (f), R04C06 for (g), R04C07 for (h), and R04C08 for (j).

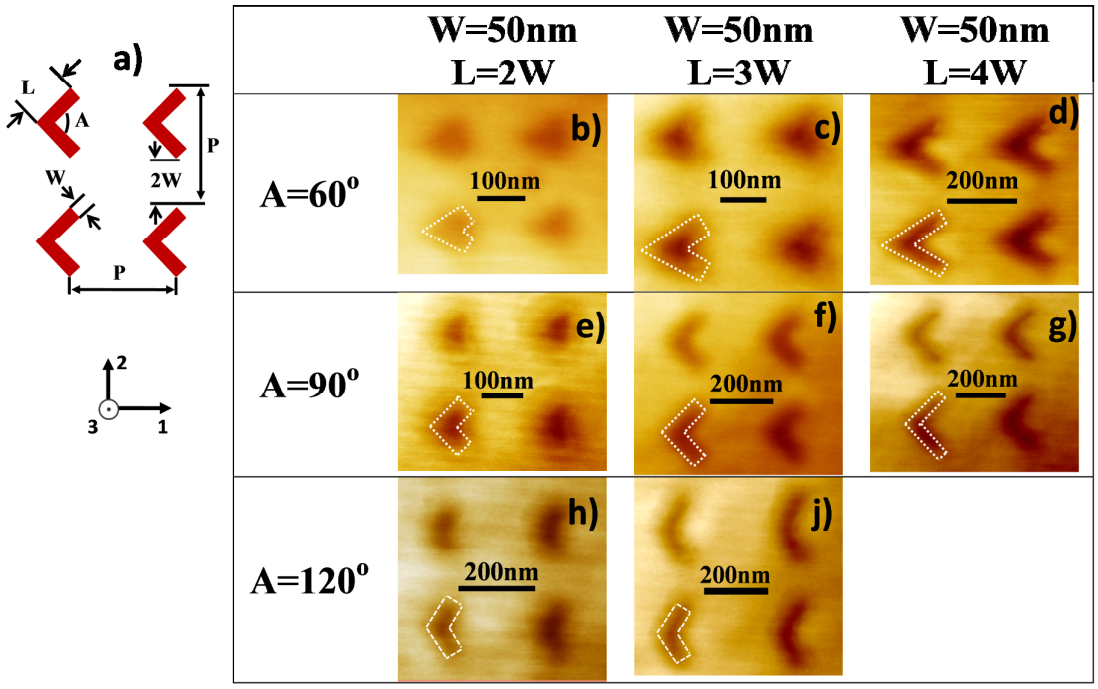

Fig. 5.3. Structure of V-shaped subwavelength nanohole array: (a) scheme of the designed parameters and atomic force microscopy image of the first set (b-d) of V-shaped arrays with 60° apex angle, the second set (e-g) of V-shaped arrays with 90° apex angle, and the third set (h-j) of V-shaped arrays with 120° apex angle. The dotted line shows the designed "V"-shapes.

5.2. Azimuthal angle dependence of SHG intensity of V-shaped nanohole arrays

Figures 5.4(a)-5.4(d) show the SHG signals from V-shaped subwavelength nanoholes shown in Fig. 5.2(b) (R04C08) for four different input and output polarization

combinations, Pin/Pout, Pin/Sout, Sin/Pout, and Sin/Sout, at the fundamental photon energy of 2.33 eV. The filled circles show the experimental data and the solid lines show the results calculated by a least-squares fitting program based on the model below. The relative scale is an arbitrary unit of SHG intensity and is shown at the upper right corner of

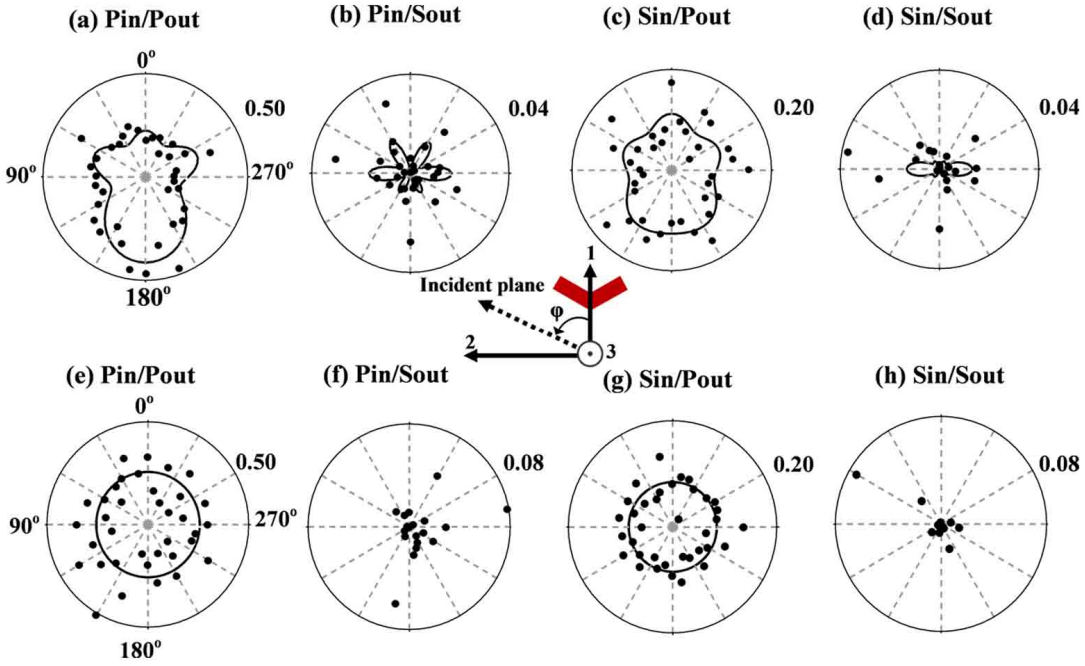

Fig. 5.4. Polar plots of second harmonic generation intensity (filled circles) versus azimuthal angle φ from V-shaped nanoholes (a-d) and bare Cr substrate (e-h) at the fundamental photon energy of 2.33 eV and an incident angle of 45°. The relative scale is an arbitrary unit of SHG intensity, shown at the upper right corner of each radar chart. The solid lines are the best-fit theoretical patterns calculated with nonlinear susceptibility $\chi^{(2)}_{ijk}$ elements as adjustable parameters. The inset at the center defines the azimuthal angle φ in relation to the coordinate. At zero degrees, the fundamental light illuminates the nanohole arrays at the valley between two arms of the V-shaped structure.

each "radar" chart. The anisotropy of the signal indeed reflects the structural anisotropy of the V-shaped nanohole arrays. Namely, both the SHG signal pattern shapes and the fabricated V-shapes show a mirror symmetry with respect to the line including the φ=0° and 180° directions. As a control, Figs. 5.4(e)-5.4(h) show SHG signals from a bare

chromium substrate. Only a weak dependence of SHG signal intensity on the rotation angle is seen in Figs. 5.3(e)-5.4(h).

To consider the dependence of the SHG response on the structural parameters

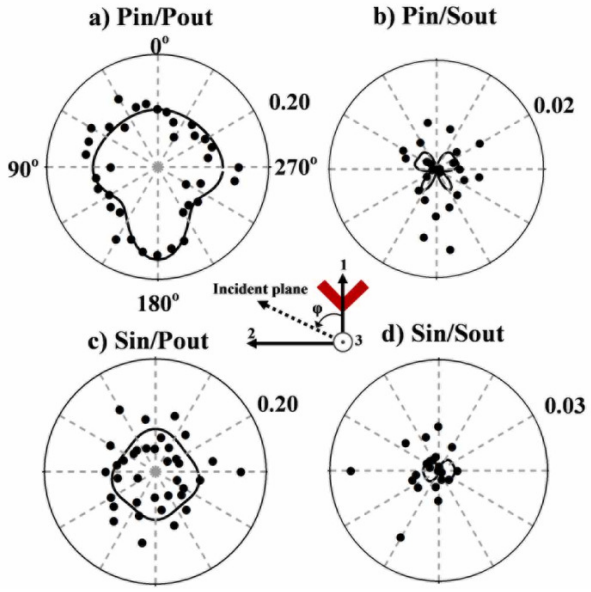

Fig. 5.5. (a-d) Polar plots of SHG intensity (filled circles) versus azimuthal angle φ from V-shaped nanoholes seen in Fig. 5.3(f). The solid lines are the best-fit theoretical patterns calculated with nonlinear susceptibility $\chi_{ijk}^{(2)}$ elements as adjustable parameters. (e) Decomposition of SHG intensity from V-shaped nanoholes when one of the nonlinear susceptibility elements $\chi_{ijk}^{(2)}$ is set equal to a calculated value and all the other elements are set equal to zero. The intensities are arbitrary but on a common scale. ijk are the suffices of the nonlinear susceptibility elements.

of V-shaped chromium nanoholes, I also performed azimuthal measurement for such V-shaped subwavelengh nanoholes as in Fig. 5.3(f). The result is presented in Figs. 5.5(a)-5.5(d). For the SHG intensity comparison, I performed azimuthal measurement of all arrays shown in Figs. 5.3(b)-5.3(j) in the same experiment condition. As a control, the SHG signal from a bare Cr substrate was measured. The experimental data of each array

were then added consecutively from 0^{o} to 350^{o} to make the comparison. The numbers of SHG photons in Pin/Pout configuration of all arrays are presented in Fig. 5.6(a). The character under each bar corresponds to the V-shaped array indicated in Figs. 5.3(b)-5.3(j). In Fig. 5.6(a), the number of SHG photons are around 9356, 10164, 10566, 8522, 9832, 10126, 11810, 12849, and 8110 photons for the arrays named as R04C01(column b), R04C02 (column c), R04C03 (column d), R04C04 (column e), R04C05 (column f), R04C06 (column g), R04C07 (column h), R04C08 (column j), and Bare Cr, respectively. The error bar was estimated based on the standard error. One can easily obtain the results using the functions in Excel.

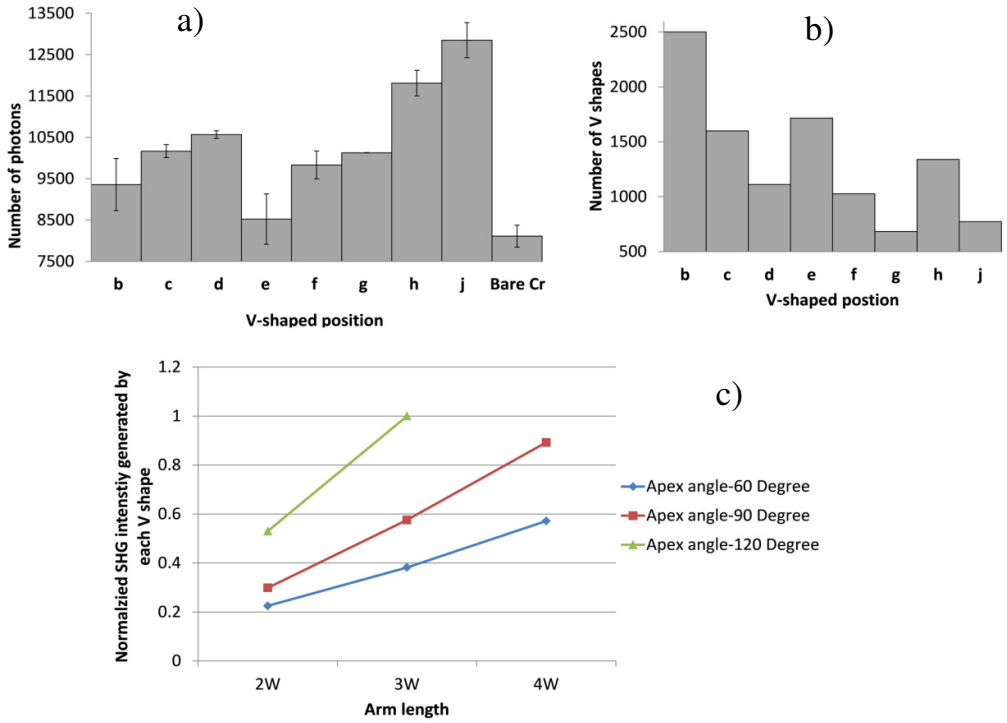

Fig. 5.6. (a) The summation of the consecutive SHG intensity of V-shaped nanohole arrays and bare chromium substrate from 0^{o} to 350^{o} in Pin/Pout configuration. The character under each bar corresponds to the V-shaped array indicated in Figs. 5.3(b)-5.3(j). (b) Number of V shaped nanoholes in each array. (c) The normalized SHG intensity emitted from each V shape calculated by dividing the total SHG intensity in (a) by the total V shaped nanoholes in (b).

5.3. Theoretical analysis

5.3.1. Optical second harmonic response of V-shaped chromium nanohole arrays

Before staring analysis process, I considered the chemical stability of Cr metal. Indeed, Ref. [91] confirms the stability of Cr metal at room temperature. Recall the work done by Shalabney [31], I found that SPRs signal of Cr was obtained in air as well as in water. This further proves the chemical stability of Cr and that the optical signal actually reflects the response of Cr. Therefore, discussion below was the optical response of Cr metal.

Following the theoretical approach performed by Omote et al. [92], I analyzed the SHG intensity patterns from the V-shaped holes in Figs. 5.4(a)-5.4(d). In doing so, the V-shaped nanohole array was treated as a flat thin dielectric slab with a thickness *d* of 5 nm since the AFM observation indicate the holes' depth is ~5nm. The dielectric constants of this slab was set equal to that of chromium with ω and 2ω frequencies quoted from Palik's handbook [35] (the detail calculation was presented in Appendix A). The induced nonlinear polarization in the second layer was defined as

$$\mathrm{P_i}(2\omega) = \varepsilon_o \chi^{(2)}_{\mathrm{ijk}} : \mathrm{E_j}(\omega)\mathrm{E_k}(\omega). \tag{141}$$

Here, ε_o is the permittivity of the vacuum, and $\mathrm{E_i}$ and $\mathrm{E_j}$ are the two applied electric fields at frequency ω. Since V-shaped nanoholes have $\mathrm{C_s}$ symmetry, ten independent nonlinear susceptibility elements, $\chi^{(2)}_{223}$, $\chi^{(2)}_{113}$, $\chi^{(2)}_{212}$, $\chi^{(2)}_{122}$, $\chi^{(2)}_{111}$, $\chi^{(2)}_{133}$, $\chi^{(2)}_{313}$, $\chi^{(2)}_{322}$, $\chi^{(2)}_{311}$, and $\chi^{(2)}_{333}$, are permitted [93]. The solid curves in Figs. 5.4(a)-5.4(d) show the calculated SHG intensity patterns. Pearson's correlation coefficients are r = 0.79 for (a), r = 0.28 for (b), r = 0.47 for (c), and r = 0.36 for (d). As mentioned in section 2.3.2 of chapter two, here $\chi^{(2)}_{\mathrm{ijk}}$ in Eq. (141), for sake of clarity, should be considered as the effective nonlinear susceptibility element in which the surface $\chi^{(2)}_s$ and the bulk Γ_s terms were incorporated. In order to visualize, one can mathematically rewrite the bulk term Γ_s in Eq.(62) as following,

$$\mathrm{P_i^Q}(2\omega) = \Gamma_{\mathrm{ijkl}} \vdots \mathrm{E_j}(\omega)\nabla_{\mathrm{k}}\mathrm{E_l}(\omega) = IK_{\mathrm{k}}\Gamma_{\mathrm{ijkl}} : \mathrm{E_j}(\omega)\mathrm{E_l}(\omega) \tag{142}$$

Here, complex number *I* and wave number *K* are in upper case to differentiate from the i and k indexes. With similar analogy, one can find that local surface and nonlocal bulk contribution exhibit a very similar way with respect to the total SHG signal.

Figure 5.7 shows the calculated SHG intensity patterns of V-shaped Cr nanoholes when one of the surface nonlinear susceptibility elements is set equal to the calculated value and all the other elements are set equal to zero. I consider in particular the Pin/Pout configuration because the r factor 0.79 shows a strong correlation [94] between the experimental data and the theoretical fit. The SHG intensities of the $\chi^{(2)}_{322}$ and $\chi^{(2)}_{333}$

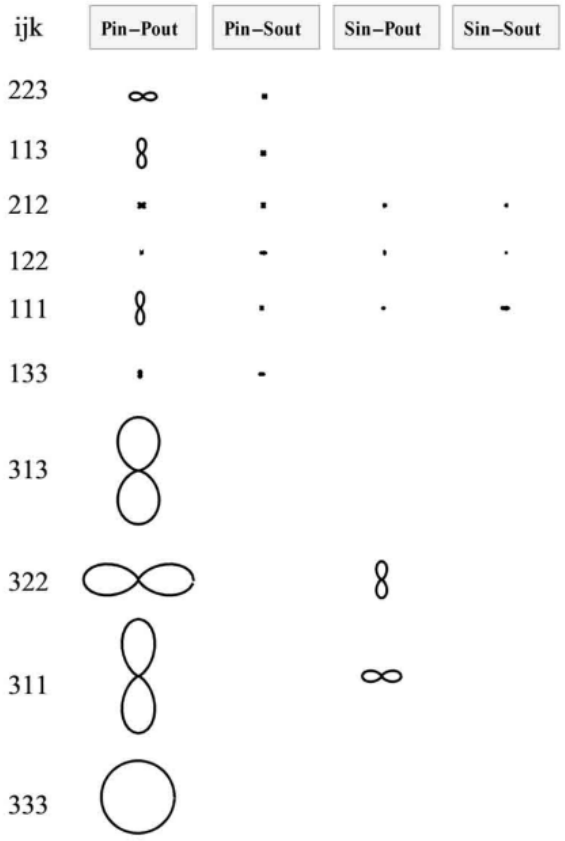

Fig. 5.7. Decomposition of SHG intensity from V-shaped nanoholes when one of the nonlinear susceptibility elements $\chi^{(2)}_{ijk}$ is set equal to a calculated value and all the other elements are set equal to zero. The intensities are arbitrary but on a common scale. ijk are the suffices of the nonlinear susceptibility elements.

elements exceed those of the others in the Pin/Pout configuration. The contribution of $\chi^{(2)}_{313}$ and $\chi^{(2)}_{311}$ components makes the intensity in the Pin/Pout configuration higher at an angle of $\varphi=180^{o}$, as shown in Figs. 5.7 and 5.4(a).

I also tried to fit the theoretical SHG intensity patterns to the experimental data in Figs. 5.4(e)-5.4(h) by assuming C_{∞} symmetry for the bare Cr substrate. Under the C_{∞} symmetry, there are three independent nonlinear susceptibility elements, $\chi^{(2)}_{113}$ ($=\chi^{(2)}_{223}$), $\chi^{(2)}_{311}$ ($=\chi^{(2)}_{322}$), and $\chi^{(2)}_{333}$. The SHG intensity contributions from $\chi^{(2)}_{311}$ and $\chi^{(2)}_{333}$ were predominant in the Pin/Pout configuration.

As for the origins of $\chi^{(2)}_{311}$ and $\chi^{(2)}_{333}$ elements, it is impossible to distinguish between the contribution of the V-shaped Cr nanoholes and the bare Cr substrate since these two susceptibility elements appear simultaneously under C_s (V-shaped hole) and C_{∞} (bare Cr substrate) symmetries. On the other hand, the contribution of the nonlinear susceptibility element $\chi^{(2)}_{313}$ in Fig. 5.7 should be purely from the nanoholes because it emerges owing to the symmetry breaking in direction 1 created by the V-shaped nanoholes.

To understand the physical origin of the large contribution of the $\chi^{(2)}_{313}$ element, I discuss several competing candidate origins including edge nonlinearity, plasmon exciation, "lightning rod effect" [95], and bulk quadrupoles. The first candidate origin is the contribution of the edge nonlinearity in the $\chi^{(2)}_{313}$ element. I define the edge nonlinearity as that from the vertical metallic sidewalls in each V-shaped hole. If the nonlinear polarization emitted from the metallic sidewalls is in direction 3, then it might contribute to the macroscopic $\chi^{(2)}_{313}$ element. In principle, the total nonlinear polarization $P(2\omega)$ must be proportional to the area of the vertical metallic sidewalls. However, my rough calculation shows that the area ratio between the exposed Cr metal of the sample surface to that of the vertical sidewalls in the nanoholes sample is 10^6:1. The SHG signal intensity of the sidewalls thus should be much lower. Consequently, the contribution of the edge nonlinearity is hardly feasible as the origin of the nonlinear susceptibility element $\chi^{(2)}_{313}$.

The next step is to discuss plasmon excitation and the "lightning rod effect" at the sharp apex [27] between two V-shaped arms. These two candidate origins should be considered together because the "lightning rod effect" and the localized field enhancement

by the surface plasmon resonances have similar behaviors [50]. When I consider the local field enhancement at the fundamental and second harmonic frequencies, the effective nonlinear susceptibility $\chi^{(2)}_{313,\mathrm{eff}}$ can be expressed as [96]

$$L_3(2\omega).\chi^{(2)}_{313}.L_1(\omega).L_3(\omega) \rightarrow \chi^{(2)}_{313,\mathrm{eff}} \tag{143}$$

Here, $L_1(\omega)$ and $L_3(\omega)$ are the local field factors at the fundamental frequency. $L_3(2\omega)$ indicates the local field factor at the second harmonic frequency. If the surface plasmon resonance or "lightning rod effect" contributes to Eq. (143), a large local field factor $L_1(\omega)$ or $L_3(\omega)$ is interpreted as making a strong nonlinear polarization in directions 1 and 3. If so, the contributions of the nonlinear susceptibility elements $\chi^{(2)}_{311}$ and $\chi^{(2)}_{322}$ in Fig. 5.7 would differ strongly because the nonlinear polarization caused by $\chi^{(2)}_{311}$ and $\chi^{(2)}_{322}$ elements is proportional to the second power of the local field factor $L_1(\omega)$ and $L_2(\omega)$, respectively. This is not the case because the ratio $I_{\chi^{(2)}_{311}}/I_{\chi^{(2)}_{322}}$ in Fig. 5.7 is 1.05. This implies that the local field enhancement at the apex is not significant.

Another noticeable feature of V-shaped Cr nanoholes is that nonlinear susceptibility elements $\chi^{(2)}_{122}$ and $\chi^{(2)}_{212}$ were absent. For V-shaped Au nanoparticles, these two nonlinear susceptibility elements presented a predominant enhancement caused by the plasmon resonance. More precisely, in the case of the $\chi^{(2)}_{122}$ element of Au nanoparticles, the applied electric field is in direction 2. High-order plasmonic waves were formed and propagated on the surface of these V-shaped gold nanoparticles. They created a strong electric field at the ends, at the middles, and at the intersection of the two arms. These "hot spots" act as the source of SHG and emit the nonlinear polarization in direction 1. In the same way, the applied electric field is in direction 1 in the case of the $\chi^{(2)}_{212}$ element. The "hot spot" was created at the intersection of the two arms and nonlinear polarization was emitted in direction 2 [39,97].

The last candidate origin is the contribution of the electric quadrupole and magnetic dipole to the second harmonic generation. In general, I can express this higher-order contribution to the nonlinear polarization at 2ω as [50,98]

$$P_i^{\mathrm{bulk}}(2\omega) \propto \Gamma_{ijkl} \vdots E_j(\omega)\nabla_k E_l(\omega) \tag{144}$$

Here, Γ_{ijkl} is the third rank susceptibility tensor. $E_j(\omega)$ and $E_l(\omega)$ are the two applied electric fields at frequency ω. Because the Cr metal was deposited by e-beam evaporation

on the silica substrate, it can be determined to have isotropic symmetry, and 21 nonzero bulk nonlinear susceptibility elements (Γ_{ijkl}) are permitted [57,58]. When the nonlinear polarization is along direction 3, the Γ_{ijkl} becomes Γ_{3jkl}. That is, Γ_{3333}, Γ_{3311} (=Γ_{3322}), Γ_{3131} (=Γ_{3232}), and Γ_{3113} (=Γ_{3223}) show the bulk nonlinear susceptibility elements.

It is often said that the bulk quadrupoles' contribution is weaker than the surface dipole contribution [45,64]. However, this is not the case for nanomaterials, because we cannot distinguish between their surface and bulk contributions. Thus, this candidate remains and there are similar examples [50,66]. As for the $\chi^{(2)}_{313}$ element, two applied electric fields are polarized in directions 1 and 3 and the higher-order contribution can be written as

$$P_3^{bulk}(2\omega) \propto \Gamma_{3311} E_3(\omega) \nabla_1 E_1(\omega) + \Gamma_{3113} E_1(\omega) \nabla_1 E_3(\omega) \quad (145)$$

As mentioned above, there are vertical metallic sidewalls contained within each V-shaped hole and they have air-chromium metal boundaries. This has a strong effect on the gradient operator ∇_1 because of the rate of spatial change of the field at the boundary of the nanohole surface. If I take the integration over the perimeter of all V-shaped holes, the nonlocal contribution thus may yield a considerable contribution.

I should also interpret the stronger contribution of the nonlinear susceptibility elements $\chi^{(2)}_{322}$, $\chi^{(2)}_{311}$, and $\chi^{(2)}_{333}$ in Fig. 5.7, which start with subscript number "3". This implies that the induced second-order polarization perpendicular to the metal surface occurs more efficiently than that parallel to the surface. This is because of the image dipole effect [99,100,101]. The dielectric function of Cr metal is -4.26+i 3.76 at 266 nm. Since the real part of the dielectric function is negative, the image dipole effect is possible.

The source of the fluctuation in Figs. 5.4 and 5.5 can be sample imperfections, such as fabrication errors, surface roughness, and dust. For e-beam lithography, there tends to be a small deviation from the ideal shape [102,103,104]. Owing to the surface roughness of Cr metal, the measured point by SHG on the substrate may microscopically move as the sample is rotated [105]. Tiny dust particles were probably attached on the sample surface during the measurements in air and are unavoidable. Most importantly, the $\chi^{(2)}_{313}$ element emerged only in the zone where the V-shaped nanoholes were located and not on the bare Cr substrate. This means that dust does not exert significant effects on the $\chi^{(2)}_{313}$ element because in the end the random dust effects tend to average out.

Considering the magnetic property of Cr, I found that at room temperature the bulk Cr shows the antiferromagnetic property [91]. Interestingly, Cr exhibits paramagnetism in the thin film case [106]. In general, using symmetric consideration, one can resolve the antiferromagnetism or paramagnetism at surfaces and in thin films by SHG [107,108]. Of course, quadrupole term usually accompanies magnetic term as regarded in section 3.4. Therefore, it should be difficult to resolve the magnetic property of Cr itself. This intriguing behavior of Cr metal could be further investigated in future works.

In conclusion, I fabricated V-shaped subwavelength slits formed in a 15-nm-thick chromium film and detected their SHG signal response. The V-shaped nanoholes were found to induce the nonlinear susceptibility element $\chi_{313}^{(2)}$. The observed SHG response was attributed to the nonlocal bulk contribution of the Cr metal.

5.3.2. Dependence of optical second harmonic of V-shaped chromium nanoholes on the structure parameters

In my previous study, I observed rotational anisotropy of the SHG from an array of V-shaped chromium nanoholes with 120^{o} apex angle A fabricated by electron beam lithography. The obtained nonlinear susceptibility element $\chi_{313}^{(2)}$ gave the information about the SHG response of V-shaped Cr nanoholes. I proposed that nonlocal bulk contribution is dominant in the case of V-shaped Cr nanoholes. The appearance of $\chi_{313}^{(2)}$ element caused by the broken symmetry in direction 1 and the strong field gradient at air-chromium metal boundaries along this direction yields a considerable SHG. Concerning the bulk contribution, the vicinity of nanostructures plays a very important role because it can result in a strong local field [109]. More recently, pioneering work of M. Zdanowiczet el al. showed that nonlocal bulk contribution is even up to ~50% of total SHG magnitude [88]. These results promoted us in further investigation of the issue.

In this work, I considered the dependence of the SHG response on the structural parameters of V-shaped chromium nanoholes. A simple model calculation was presented to deduce the experimental results. The work is therefore expected to provide new information in adjustment of the nonlinear optical behavior of metamaterial for functional applications.

I first discuss the nonlinear optical response in Fig. 5.8, showing the decomposed nonlinear susceptibly elements' contribution of theoretical curves in Figs. 5.5(a)-5.5(d). This result is similar to our previous report [110] for V nanohole named R04C08 in Fig. 5.7. The elements $\chi^{(2)}_{322}$, $\chi^{(2)}_{311}$, and $\chi^{(2)}_{333}$ show a predominant contribution as shown in Fig. 5.7. This is because of the image dipole effect [99,110]. More importantly, the essential

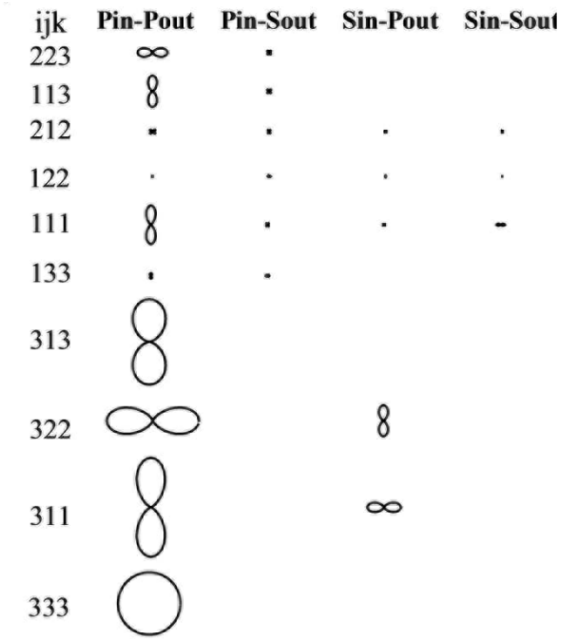

Fig. 5.8. Decomposition of SHG intensity from V-shaped nanoholes when one of the nonlinear susceptibility elements $\chi^{(2)}_{ijk}$ is set equal to a calculated value and all the other elements are set equal to zero. The intensities are arbitrary but on a common scale. ijk are the suffices of the nonlinear susceptibility elements.

feature of the V-shaped Cr nanoholes was characterized by the enlargement of the $\chi^{(2)}_{313}$ element in Pin/Pout configuration. In my previous work I concluded that the appearance of $\chi^{(2)}_{313}$ results from the Cr bulk contribution [111]. Second order nonlinear polarization in nanostructure can be expressed as a generalized polarization [52],

$$\mathbf{P}(2\omega) = \mathbf{P} - \nabla.\mathbf{Q} + \frac{\mu_0}{i\omega}\nabla \times \mathbf{M} + \cdots \tag{146}$$

On the right hand side, **P**, **Q**, and **M** present the electric dipole, electric quadrupole, and magnetic dipole, respectively. $\mu_0$is the permeability of the vacuum and ω is the

angular frequency of the incident laser. The second and the third terms can be rewritten in an isotropic medium as,

$$P_3^{bulk}(2\omega) \propto \Gamma_{3311} E_3(\omega) \nabla_1 E_1(\omega) + \Gamma_{3113} E_1(\omega) \nabla_1 E_3(\omega) \quad (147)$$

Here, Γ_{ijkl} is the third rank susceptibility tensor, and $E_j(\omega)$ and $E_l(\omega)$ are the two applied electric fields at frequency ω. The two terms in Eq. (147) give effectively the second order response to the electric field.

Next, I consider the bar chart in Fig. 5.6(a). Obviously, one can see that the SHG intensities from all V-shaped arrays are larger than that from the bare Cr substrate, meaning that the SHG response of V-shaped nanoholes is indeed significant. I further estimated tentatively the contribution of individual V shape by dividing the total SHG intensity in Fig. 5.6(a) by the corresponding total numbers of V shaped nanoholes in Fig. 5.6(b). The result is shown in Fig. 5.6(c). The reason for the word "tentatively" is that the SHG intensity emitted by each V shaped nanohole thus obtained may have error because the interference between the SHG from different nanoholes is not considered. Nevertheless, all sets of the V shape with A of 60^o, 90^o, and 120^o show enhancement in SHG intensity when L increases. Furthermore, for larger A, the SHG intensity per one V shape was stronger than for smaller A. A appears to affect the SHG intensity of V-shaped nanoholes.

I discuss the possible sources of the obtained SHG signal difference shown in Fig. 5.6(c). The plasmon excitation did not emerge in previous report [110], therefore the obtained SHG signal should result from the characteristic contribution of $\chi_{313}^{(2)}$ element of V-shaped nanoholes, resulting from the bulk contribution. As pointed out previously [110], there are vertical metallic sidewalls contained within each V-shaped hole and they have air-chromium metal boundaries. This has a strong effect on the gradient operator ∇_1 shown in Eq. (147).

Let me consider the simplest model as depicted in Fig. 5.9(b). Tentatively, three rectangular holes formed in Cr metal could make a model of V-shaped hole structure based on the process of approximation in Fig. 5.9(a). Here, the analysis methodology used to approach "three rectangular holes" shown in Fig. 5.9(b) is quite similar to that used in finite-difference time-domain method with the discretized spatial domain on the edges of a V-shaped hole. If I deliberately divide the boundary into the crude regions as shown in

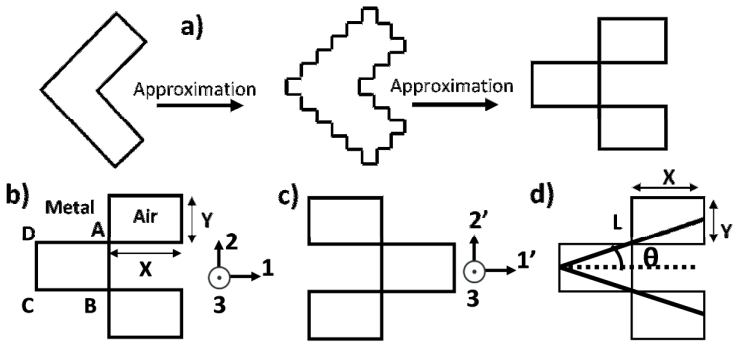

Fig. 5.9. Three rectangular holes formed in Cr metal could tentatively form a model of V-shaped hole structure: (a) Two-step approximation of a V-shaped hole by three rectangular holes; (b) initial and (c) final position of rectangular holes after rotating 180°. This model could easily visualize the field gradient in direction 1. (d) Definition of θ.

Fig. 5.9(a), the V-shaped hole could be judged as three rectangular holes. I assume that the spatial derivation have a minus sign if the coordinate runs from the metal to air side. The coordinate origin is on the AB segment. For the rectangular hole on the left side of AB segment, Eq. (147) can be rewritten as follows for the boundary along the the AB segment,

$$P_3^{AB}(2\omega) \propto (1/t)\Gamma_{3311}E_3(\omega)E_1(\omega)Y + (1/t)\Gamma_{3113}E_1(\omega)E_3(\omega)Y \quad (148)$$

I introduce the factor $1/t$ because, in principle, the rate of field gradient has to be inversely proportional to length of scope t. Here t should be understood as the depth in which the field penetrates into Cr. Since field gradient is along direction 1, the magnitude should be proportional to the length Y. For the boundary along CD segment, I obtained the following expression,

$$P_3^{CD}(2\omega) \propto -(1/t)\Gamma_{3311}E_3(\omega)E_1(\omega)Ye^{-ik_1X} - (1/t)\Gamma_{3113}E_1(\omega)E_3(\omega)Ye^{-ik_1X} \quad (149)$$

Here the phase factor e^{-ik_1X} was added because of the distance from the origin. The total nonlinear polarization created by this rectangular hole is,

$$P_3^{AB}(2\omega) + P_3^{CD}(2\omega) \propto (1/t)E_1(\omega)E_3(\omega)Y[\Gamma_{3311} + \Gamma_{3113}]\left[1 - e^{-ik_1X}\right] \quad (150)$$

After similar operation for the two rectangular holes to the right of the AB segment, the total nonlinear polarization created by the three holes will be,

$$P_3^{total}(2\omega) \propto (1/t)E_1(\omega)E_3(\omega)Y[\Gamma_{3311} + \Gamma_{3113}]\left[\left(1 - e^{-ik_1X}\right) + 2\left(e^{ik_1X} - 1\right)\right] \quad (151)$$

To simplify Eq. (151), I expand e^{-ik_1X} and e^{ik_1X} up to second order polynomial approximation of Taylor series. Then Eq. (151) becomes,

$$P_3^{total}(2\omega) \propto (1/t)E_1(\omega)E_3(\omega)[\Gamma_{3311} + \Gamma_{3113}]\left[3ik_1XY - (1/2){k_1}^2X^2Y\right] \quad (152)$$

I did the similar calculation for the holes in Fig. 5.9(c) and the result is as following,

$$P_3^{total}(2\omega) \propto (1/t)E_1(\omega)E_3(\omega)[\Gamma_{331'1'} + \Gamma_{31'1'3}]\left[3ik_{1'}XY + (1/2){k_{1'}}^2X^2Y\right] \quad (153)$$

The detail calculation is explained in Appendix C. In Eqs. (152) and (153), the terms proportional to $3ik_1XY$ and $3ik_{1'}XY$ should cancel with the terms from other Γ_{ijkl} elements since these terms do not behave like the tensor $\chi^{(2)}_{313}$. The term proportional to $-(1/2){k_1}^2X^2Y$ in Eq. (152) changes sign in Eq. (153) and behaves like $\chi^{(2)}_{313}$. Hence, Eq. (152) becomes,

$$P_3^{total}(2\omega) \propto -(1/2t)E_1(\omega)E_3(\omega)[\Gamma_{3311} + \Gamma_{3113}]{k_1}^2X^2Y \quad (154)$$

Since Eq. (154) results from the approximation of Tayler series of exponential functions, e^{-ik_1X} and e^{ik_1X}, the smaller the exponent is, the more precise the result will be. Therefore, it would be a good approximation if X is smaller than the wavelength.

I now try to interpret the effect of the arm length as well as the apex angle, by seeing Eq. (154) and Fig. 5.9 (b). Here, increasing the arm length corresponds to increasing X and Y values in the same rate. Making a larger apex with constant arm length L means increasing the Y and decreasing the X values at the same time. Using the angle θ, a half of apex angle A seen in the simple model shown in Fig. 5.9 (d), the X and Y values are expressed as $X = \frac{1}{2}Lcos\theta$ and $Y = Lsin\theta$, respectively. Then, the nonlinear polarization has the form

$$P_3^{total}(2\omega) \propto \frac{1}{4}L^3 sin\theta cos^2\theta \quad (155)$$

According to Eq. (154), $P_3^{total}(2\omega)$ increases as X and Y increases or the arm length L increases as deduced in Eq. (155). In Fig. 3(c), the SHG intensity increases as the arm length L is increased and it is consistent with this prediction. On the other hand, $\frac{1}{4}L^3 sin\theta cos^2\theta$ in Eq. (155) is numerically calculated as $\sim 0.094L^3$ at θ = 30° and $\sim 0.088L^3$ at θ = 45°. The result obtained in Fig. 5.6 (c), however, indicated that SHG intensity increased together with the enlargement of the apex angle. The discrepancy

between the model and the experimental data might result from the complexity of the other parameters not incorporated into this simple model. In addition, in Fig. 5.3 the shapes of the nanoholes are more obscure when the apex angle A reduces. Since the shapes are less perfect, the SHG intensity is reduced accordingly.

Again, I should mention the interference effect among these V holes. Since all the V-shaped nanohole domains have the periodicity equal or larger than 200nm, the strong near-field coupling or grating effect should be ignored [28]. Furthermore, since the periodicity P changed together with the shape of the V holes, it would be complicated to estimate the role of the interference for a specific V-shaped parameters. In future works, keeping an invariable V shape and changing the periodicity P should produce such interference.

In conclusion, in previous work, nonlinear optical response of V-shaped Cr nanohole arrays was reported. The SHG was attributed to the bulk quadrupoles from the azimuthal angle dependence analysis of the SHG for Pin/Pout polarization combination. In this work, I have shown that there is a systematic dependence of the SHG intensity on the designed parameters of Cr nanoholes, especially on the arm length. The V-shaped nanoholes were found to induce the effective nonlinear susceptibility element $\chi_{313}^{(2)}$ owing to the artificial broken symmetry in the direction between its two arms. Simple model was given and its limitation was also clarified. From the consistency between the experiment and the model, the contribution of the bulk quadrupoles in the second order optical response of Cr metal was confirmed. In particular, the strong field gradient at the boundaries of the holes gives rise to the nonlinear response. For favorable material exploited for artificial nanostructures such as gold, plasmon exciation enhancing nonlinear optical effect could be accomplished. However, in the case of Cr metal plasmon was silent and the nonlinear optical behavior results from the bulk contribution of Cr electrons. This can be useful for designing artificial nonlinear optical materials with different properties from those made of plasmonic materials.

CHAPTER 6
GENERAL CONCLUSION

The field of plasmonics has great achievements during the recent years. The development of nanoscience technology allows scientists to tailor several new materials with various characterizations. A new term of materials named "plasmonics" thus was born with properties and functionalities that cannot be found in natural materials. In nonlinear optics, plasmonics could expectedly enhance the nonlinear efficiency as well as reduce the nonlinear components in size. When the metallic structures go down to nanoscale, their second order optical response becomes more intriguing. Especially, surface (dipole) and bulk (higher multipole) terms accompany each other in the total SHG signal. Thus, proper estimation of dipole and higher multipole (magnetic dipole and electric quadrupole) terms in the surface second harmonic generation signal should be addressed in order to understand how the nonlinear responses could be improved.

Within the general purpose, this work focused on examination of both surface and multipolar bulk effects by clarifying the microscopic origin of nonlinear susceptibility element of Cr nanohole structure. The V-shaped nanohole arrays were fabricated by electron beam lithography and investigated by observing surface second harmonic generation and analyzing nonlinear susceptibility elements. Furthermore, in order to estimate the role of designed parameters, I have systematically investigated the dependence of SHG intensity when the apex angles and arm lengths of studied structures were modified.

In this project, V-shaped subwavelength slits formed in a 15-nm-thick chromium film was fabricated by electron beam lithography. The V-shaped nanohole arrays' nonlinear optical response was detected by surface second harmonic generation method. As V shape belongs to C_s symmetry, ten independent nonlinear susceptibility elements, $\chi^{(2)}_{223}$, $\chi^{(2)}_{113}$, $\chi^{(2)}_{212}$, $\chi^{(2)}_{122}$, $\chi^{(2)}_{111}$, $\chi^{(2)}_{133}$, $\chi^{(2)}_{313}$, $\chi^{(2)}_{322}$, $\chi^{(2)}_{311}$, and $\chi^{(2)}_{333}\chi^{(2)}_{333}$ were introduced into the fitting program. The results have shown the crucial feature of the V-shaped Cr nanoholes caused by the enlargement of the $\chi^{(2)}_{313}$ element in Pin/Pout configuration. The plasmon effect was discussed owing to the basis of the obtained susceptibility elements.

Actually, Shalabney et al. found surface plasmon resonance in Cr columnar thin film in the Kretschmann configuration. The present study, however, did not noticeably detected surface plasmon resonance from V-shape Cr nanoholes.

Note that the high imaginary part of the refractive indexes of Cr at 532 nm wavelength (see Appendix A) could make the strong absorption loss in Cr metal. This feature was already mentioned in Shalabney's work where the broadening of the surface plasmon resonance dip can be seen. Furthermore, the damping coefficient Γ of Cr gives a large value compared with Ag and Au. It could prevent the electron oscillations. Generally, the damping coefficient is considered to be invariable for a given metal at a given temperature. However, when one tailors the artificial structures down to nanoscale, the movement of the electron is confined owing to the size reduction. The electron mean free path is therefore reduced by the physical boundary of the metal structure. The features could further modify and enlarge the damping coefficient. I suggested that these effects, absorption loss and large damping coefficient could result in the inactive plasmon resonance in the case of Cr nanoholes. The nonlinear optical behavior thus appears by the bulk contribution of Cr electrons. It is intriguing behavior of the V-shaped Cr nanohole arrays since higher multipole effects, instead of electric dipole, are dominant. The result therefore is particularly important to explain the nonlinear optical response of metal nanostructures and metamaterials since from the early development of nonlinear optics, estimating the role of the electric dipole and the higher multipole effects is still under investigation.

I have attempted to demonstrate the SHG dependence on the structure parameters of the nanoholes. Thus, three sets of V-shaped subwavelength slits formed in a 15-nm-thick Cr film were fabricated and their SHG signal responses were detected. The SHG intensity in Pin/Pout configuration was enhanced when the arm length was enlarged. Furthermore, for larger apex angle, the SHG intensity was stronger. In this work, I have presented a three-rectangular-holes model to figure out the influence of V shape's structural parameters on the nonlinear response. This concept qualitatively explained the systematic dependence of the SHG intensity on the designed parameters of Cr nanoholes, especially on the arm length. Its limitation was also clarified.

In conclusion, this thesis has shown that V-shaped Cr nanohole arrays did not remarkably create surface plasmon resonance. The nonlinear optical behavior results from

the bulk contribution of Cr electrons where the field gradient at the boundary plays a major role. I have shown how the SHG intensity alters when the arm length and apex angle are changed.

In future work, it would be interesting to further address plasmon excitation of Cr. To do that, the role of phase matching should be considered in detail since it strongly affects the efficient coupling between electron oscillation and the electromagnetic field. Some changes to the designed parameters should be made. At first, two specific values of the periodicity at 310.47nm and 743.05nm are the open strategies and these parameters could further be investigated. Here, I obtained these two P values by exploiting Eqs. (40) and (41). Instead of V-shaped holes, the second layer (V hole layer) was assumed as the grating (simplest case) with the periodicity P. I found that at incident angle of 45^{o}, excitation wavelength of 532nm, and the periodicity P of 310.47nm or 743.05nm the wave vector k of incident wavelength should strongly match that of plasmon wave at the interface. An enhancement of SHG intensity, therefore, is expected at these specific values.

APPENDIX A

CALCULATION OF CR DIELECTRIC FUNCTION

Chromium in evaporation is performed by heating Cr directly in vacuum using a conical basket of W [112]. Chromium is used as anticorrosion plating of devices, such as spectrometers [112]. It is quite stable at room temperature [112]. The reflectance spectra of Cr are shown in Fig. A1.

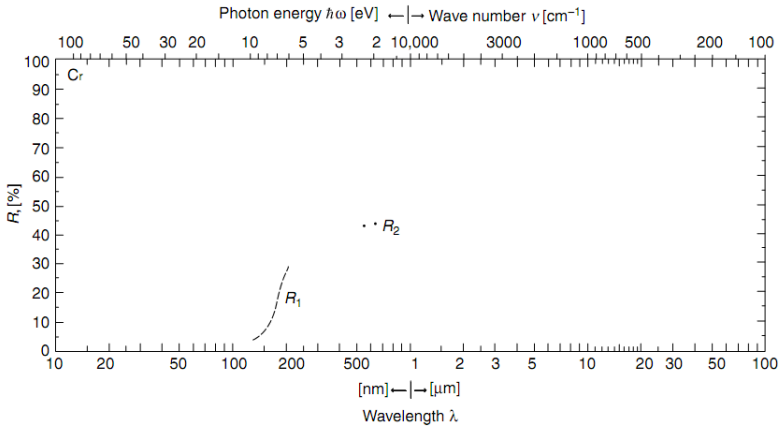

Fig. A1. Reflectance spectra of Cr. R_1: obtained from n_1 and k_1 of evaporated film, R_2: obtained from n_2 and k_2 of evaporated film [112].

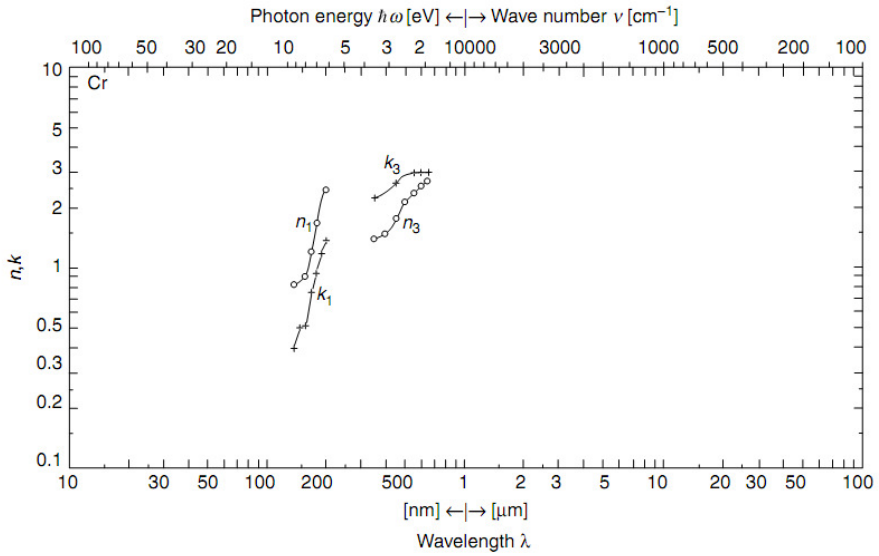

Fig. A2. Optical constants (n_i, k_i: i = 1, 3) of Cr [112].

In practically, the precise value of Cr dielectric function at 523nm and 266nm was found by assuming some high-order polynomials. The fitting results shown in Fig. A.3 indicate the real part and imaginary of the refractive index of Cr metal. Here, the solid lines are least-squares fit to a list of data (filled circles). The real and imaginary parts of Cr dielectric function was found by following equations

$$\varepsilon' = n^2 - \kappa^2 \tag{A1}$$

$$\varepsilon'' = 2n\kappa \tag{A2}$$

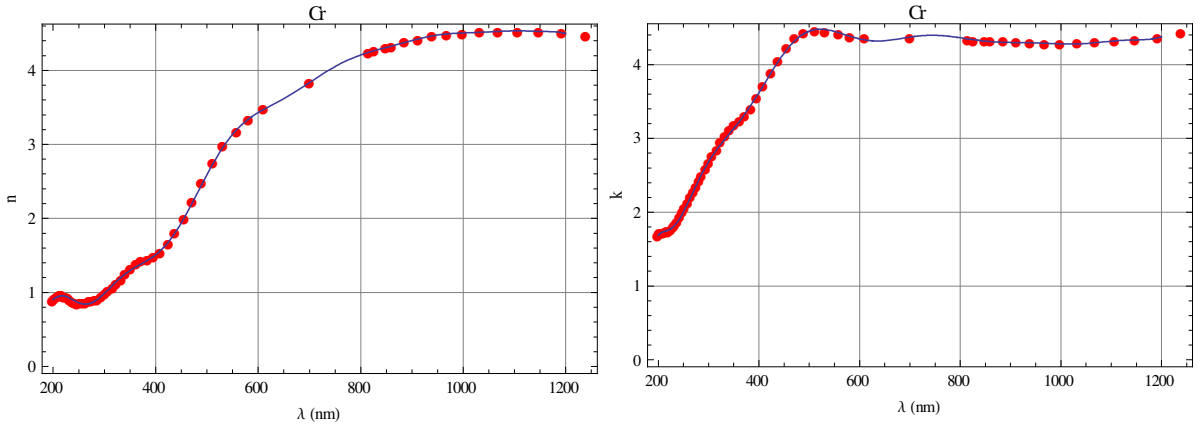

Fig. A3. Cr dielectric function as function of wavelength. The solid lines are least-squares fit to a list of data (filled circles): (a) real part of the refractive index n of Cr; (b) imaginary part of the refractive index κ of.

APPENDIX B

REFRACTIVE INDEX OF FUSED SILICA

Fused silica forms the amorphous phase and is not crystalline [112]. It is known as quartz glass, fused glass, silicate glass, or fused quartz. Typical values of the index of refraction vary among type of each glass. Here I show the refractive index of fused silica at several wavelengths, 1.44968 at 1064 nm, 1.46008 at 546.1 nm, 1.47435 at 365.0 nm, and 1.53430 at 312.6 nm [90].

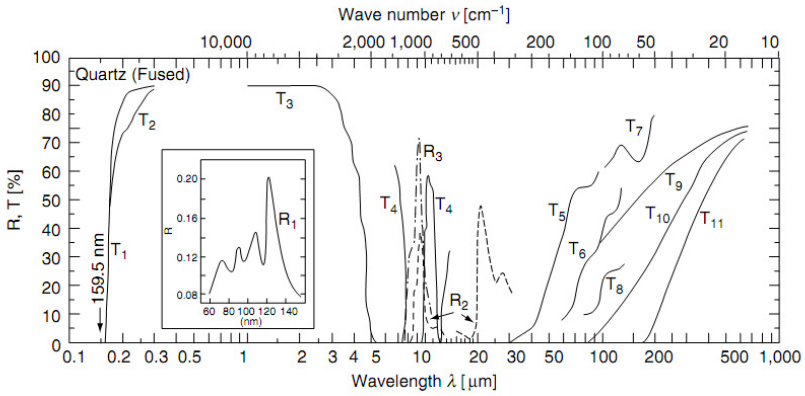

Fig. B1. Transmittance and reflectance spectra of fused quartz [112].

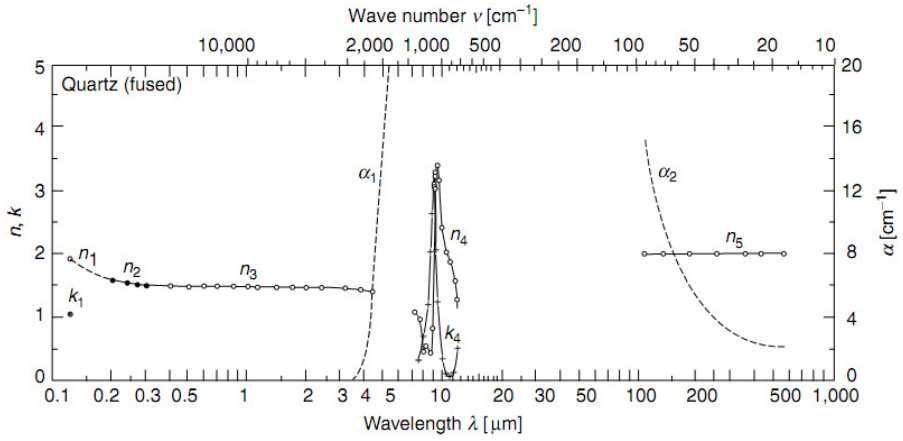

Fig. B2. Optical constants (n_i: i = 1–5, k_i; i = 1, 4) and absorption coefficient (a_i: i = 1, 2) of fused quartz [112].

APPENDIX C

CALCULATION OF THREE RECTANGULAR HOLES

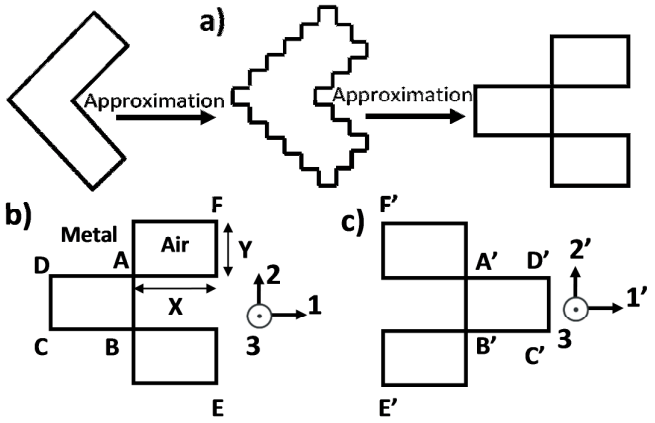

Fig. B1. Three rectangular holes formed in Cr metal could tentatively form a model of V-shaped hole structure: (a) Two-step approximation of a V-shaped hole by three rectangular holes; (b) initial and (c) final position of rectangular holes after rotating 180°. This model could easily visualize the field gradient in direction 1.

In the case of Fig. B1 (b), as I assumed that the spatial derivation had a minus sign if the coordinate runs from the metal to air side. The coordinate origin is on the AB segment. For the rectangular hole on the left side of AB segment, Eq. (147) can be rewritten as follows for the boundary along the the AB segment,

$$P_3^{AB}(2\omega) \propto \left(\frac{1}{t}\right)\Gamma_{3311}E_3(\omega)E_1(\omega)Y + \left(\frac{1}{t}\right)\Gamma_{3113}E_1(\omega)E_3(\omega)Y \qquad (B1)$$

I introduced the factor $1/t$ because, in principle, the rate of field gradient has to be inversely proportional to length of scope t. Since field gradient is along direction 1, the magnitude should be proportional to the length Y. For the boundary along CD segment, I obtained the following expression,

$$P_3^{CD}(2\omega) \propto -\left(\frac{1}{t}\right)\Gamma_{3311}E_3(\omega)E_1(\omega)Ye^{-ik_1X} - \left(\frac{1}{t}\right)\Gamma_{3113}E_1(\omega)E_3(\omega)Ye^{-ik_1X} \qquad (B2)$$

Here the phase factor e^{-ik_1X} was added because of the distance from the origin. The total nonlinear polarization created by this rectangular hole is,

$$P_3^{AB}(2\omega) + P_3^{CD}(2\omega) \propto \left(\frac{1}{t}\right) E_1(\omega) E_3(\omega) Y[\Gamma_{3311} + \Gamma_{3113}]\left[1 - e^{-ik_1 X}\right] \tag{B3}$$

For the two rectangular holes to the right of the AB segment, I first estimate Eq. (147) along the AB segment,

$$P_3^{AB}(2\omega) \propto -2\left(\frac{1}{t}\right)[\Gamma_{3311} + \Gamma_{3113}] E_3(\omega) E_1(\omega) Y \tag{B4}$$

The formula for two segments along EF direction would be,

$$P_3^{EF}(2\omega) \propto 2\left(\frac{1}{t}\right)[\Gamma_{3311} + \Gamma_{3113}] E_3(\omega) E_1(\omega) Y\left[e^{-ik_1 X}\right] \tag{B5}$$

The total nonlinear polarization created by the three holes would be,

$$P_3^{total}(2\omega) \propto \left(\frac{1}{t}\right) E_1(\omega) E_3(\omega) Y[\Gamma_{3311} + \Gamma_{3113}]\left[\left(1 - e^{-ik_1 X}\right) + 2\left(e^{ik_1 X} - 1\right)\right] \tag{B6}$$

To simplify Eq. (B6), I expanded $e^{-ik_1 X}$ and $e^{ik_1 X}$ up to second order polynomial approximation of Taylor series. Then Eq. (B6) became,

$$\begin{aligned} P_3^{total}(2\omega) &\propto \left(\frac{1}{t}\right) E_1(\omega) E_3(\omega) Y[\Gamma_{3311} + \Gamma_{3113}]\left[2e^{ik_1 X} - e^{-ik_1 X} - 1\right] \\ &\propto \left(\frac{1}{t}\right) E_1(\omega) E_3(\omega) Y[\Gamma_{3311} + \Gamma_{3113}]\left[2\left(1 + ik_1 X - \frac{(k_1 X)^2}{2}\right)\right. \\ &\left. - \left(1 - ik_1 X - \frac{(k_1 X)^2}{2}\right) - 1\right] \\ &\propto \left(\frac{1}{t}\right) E_1(\omega) E_3(\omega) Y[\Gamma_{3311} + \Gamma_{3113}]\left[\left(3ik_1 X - \frac{(k_1 X)^2}{2}\right)\right] \end{aligned} \tag{B7}$$

For the rectangular hole on the right side of A'B' segment shown in Fig. B1(c), the result was as follow,

$$P_3^{A'B'}(2\omega) + P_3^{C'D'}(2\omega) \propto \left(\frac{1}{t}\right) E_1(\omega) E_3(\omega) Y[\Gamma_{3311} + \Gamma_{3113}]\left[1e^{ik_1 X} - 1\right] \tag{B8}$$

For the two rectangular holes on the left of the A'B' segment, I had

$$P_3^{total}(2\omega) \propto 2\left(\frac{1}{t}\right) E_1(\omega) E_3(\omega) Y[\Gamma_{3311} + \Gamma_{3113}]\left[\left(1 - e^{-ik_1' X}\right)\right] \tag{B9}$$

The result after adding Eqs. (B8) and (B9) and expanding Taylor series leads

$$
\begin{aligned}
P_3^{\text{total}}(2\omega) &\propto \left(\frac{1}{t}\right) E_{1'}(\omega) E_3(\omega) Y[\Gamma_{331'1'} + \Gamma_{31'1'3}]\left[1 - 2e^{ik_{1'}X} e^{ik_{1'}X}\right] \\
&\propto \left(\frac{1}{t}\right) E_{1'}(\omega) E_3(\omega) Y[\Gamma_{331'1'} + \Gamma_{31'1'3}]\left[1 \right. \\
&\left. - 2\left(1 - ik_{1'}X - \frac{(k_{1'}X)^2}{2}\right) + \left(1 + ik_{1'}X - \frac{(k_{1'}X)^2}{2}\right)\right] \\
&\propto \left(\frac{1}{t}\right) E_{1'}(\omega) E_3(\omega) Y[\Gamma_{331'1'} + \Gamma_{31'1'3}]\left[\left(3ik_{1'}X + \frac{(k_{1'}X)^2}{2}\right)\right]
\end{aligned}
\tag{B10}
$$

APPENDIX D

PEARSON'S CORRELATION COEFFICIENT

Considering two data sets, $\{a_1, a_2, a_{3...} a_n\}$ and {b1, b2… bn}, Pearson's correlation coefficients r is:

$$\frac{[(n-1)a_1 - a_2 - \cdots - a_n]b_1 + [(n-1)a_2 - a_1 - \cdots - a_n]b_2 + [(n-1)a_n - a_1 - \cdots - a_{n-1}]b_2}{\left[\begin{array}{c}\sqrt{[(n-1)a_1 - a_2 - \cdots - a_n]a_1 + [(n-1)a_2 - a_1 - \cdots - a_n]a_2 + \cdots + [(n-1)a_n - a_1 - \cdots - a_{n-1}]a_n} \cdot \\ \sqrt{[(n-1)b_1 - b_2 - \cdots - b_n]b + [(n-1)b_2 - b_1 - \cdots - b_n]b_2 + \cdots + [(n-1)b_n - b_1 - \cdots - b_{n-1}]b_n}\end{array}\right]}$$

APPENDIX E

ABSTRACT OF SUBTHEME RESEARCH

Epitaxial growth of ZrB_2 thin film on Ge(111) substrate

For the application in light emitting diodes (LEDs), the semiconducting group III nitrides including GaN, AlN and InN with direct bandgaps ranging from 0.7 eV to 6.0 eV are the excellent materials. Among them, GaN has been considered as the most interesting material for LEDs with blue, violet and ultraviolet light emitting. Commonly, α-Al_2O_3 and SiC act as substrate to grow GaN layer however, the issues such as lattice constant and thermal expansion coefficients misfit have prevented a good epitaxial growth of GaN on them.

To grow epitaxial gallium nitride on a foreign substrate, the availability of large size Si wafer is very interesting for application in optoelectronic devices and Si(111) plane is preferred because of the hexagonal symmetry with respect to thin film. Nevertheless, the large thermal expansion coefficients and lattice mismatch with GaN make Si(111) not an optimal substrate to directly grow GaN. A buffer layer, therefore, is the choice to reduce high defect density.

To overcome this issue, Ge(111) wafers have been recently tried as a substrate for epi film GaN(0001) layer because of the good matching in thermal expansion coefficient. Ge has the same crystal structure as Si: the diamond structure (Si and Ge with lattice constant of 5.431 and 5.658 Å respectively). The thermal expansion coefficients mismatch of Ge, -5,5% with respect to GaN, is an advantage when comparing with that of Si (54%) as well as other substrates. Nevertheless, the harm in lattice spacing mismatch of 20% makes it discouraging to deposit GaN on Ge substrate with perfect quality. Growing a ZrB_2 buffer layer is the method to diminish the dislocation density due to lattice mismatch.

In the role of a buffer layer, zirconium diboride bring out a smooth transition between the film and substrate to reduce a huge lattice constant mismatch. Moreover, because of the high reflection of 100% from the ultraviolet to visible range, ZrB_2 will

reinforce the Ge substrate with reflection varying from 40% to 70% in the range 200nm to 1000nm. Thus, when using ZrB_2 as a buffer layer, the efficiency is expected to increase significantly for those applications in efficient light sources. This motivates us in the growth of ZrB_2(0001) buffer layer on Ge(111).

We grew ZrB_2(0001) thin films on Ge (111) substrate. The effect of the growth temperature was investigated. The RHEED patterns and AFM images strongly exhibit the effect of temperature with respective to the ZrB_2 film quantity. From the AFM images, we can found that at a higher growth temperature, ZrB_2 give a better morphology. The XRD results indicate the (0001) plane of ZrB_2 film is parallel to the (111) plane of Ge.

The subtheme project was conducted under the guidance of Associate Professor YukikoYamada-Takamura.

APPENDIX F

LIST OF PUBLICATION AND CONFERENCE PARTICIPATION

Publication

1. Ngo Khoa Quang, Yoshihiro Miyauchi, Goro Mizutani, Martin D. Charlton, Ruiqi Chen, Stuart Boden, and Harvey Rutt, "Optical second harmonic generation from V-shaped chromium nanohole arrays", Jpn. J. Appl. Phys. **53**, 02BC11 (2014).
2. Ngo Khoa Quang, Yoshihiro Miyauchi, Goro Mizutani, Martin D. Charlton, Ruiqi Chen, Stuart Boden, and Harvey Rutt, "Optical second harmonic generation of V-shaped chromium nanoholes---dependence on the structure parameters of the nanoholes", accepted for publication.

Conference participation

1. Ngo Khoa Quang, Yoshihiro Miyauchi, Goro Mizutani, Martin D. Charlton, Ruiqi Chen, Stuart Boden, and Harvey Rutt, "Apex angle dependence of optical second harmonic response of V-shaped Chromium nanohole arrays", 9th International Symposium on Atomic Level Characterizations for New Materials and Devices '13, Sheraton Kona, The Big Island, Hawaii, USA, December 2^{th} -6^{th}, 2013.
2. Ngo Khoa Quang, Yoshihiro Miyauchi, Goro Mizutani, Martin D. Charlton, Ruiqi Chen, Stuart Boden, and Harvey Rutt, "Optical Second Harmonic Response from V-shaped Chromium Nanohole Arrays", The 57^{th} Japan Congress on Materials Research, Kyoto Terrsa, Kyoto, Japan, November 25^{th} -26^{th} , 2013.
3. Ngo Khoa Quang, Yoshihiro Miyauchi, Goro Mizutani, Martin D. Charlton, Ruiqi Chen, Stuart Boden, and Harvey Rutt, "Nonlinear optical examination of V-shaped Chromium nanohole arrays", JSPS HOKURIKU-SHINETSU branch meeting, Kanazawa Institute of Technology, Nonoichi, Ishikawa Prefecture, Japan, November 22^{th} -23^{th}, 2013.
4. Ngo Khoa Quang, Yoshihiro Miyauchi, Goro Mizutani, Martin D. Charlton, Ruiqi Chen, Stuart Boden, and Harvey Rutt, "Characterization of V-shaped Chromium

nanoholes using surface second harmonic generation method", International Symposium on Advanced Materials, Japan Advanced Institute of Science and Technology 1-1 Asahidai, Nomi, Ishikawa 923-1292 Japan, October 17th-18th, 2013.

5. Ngo Khoa Quang, Yoshihiro Miyauchi, Goro Mizutani, Martin D. Charlton, Ruiqi Chen, Stuart Boden, and Harvey Rutt (2013), "Optical Second Harmonic Generation from V-shaped Chromium Nanohole Arrays", The 4th International Symposium on Organic and Inorganic Electronic Materials and Related Nanotechnologies (EM-NANO 2013), Kanazawa, Japan, June 17th-20th , 2013.

REFERENCES

[1] L. Novotny and B. Hecht, *Principles of Nano-Optics* (Cambridge University Press, New York, 2006).

[2] H. Husu, B. K. Canfield, J. Laukkanen, B. Bai, M. Kuittinen, J. Turunen, and M. Kauranen, Metamaterials **2**, 155 (2008).

[3] E. Hecht, *Optics* (Addison Wesley, CA, 2002).

[4] W. Cai and V.Shalaev, *Optical Metamaterials Fundamentals and Applications* (Springer, NY, 2009).

[5] M. Michailov, *Nanophenomena at Surfaces: Fundamentals of Exotic Condensed Matter Properties* (Springer-Verlag Berlin Heidelberg, 2011).

[6] J. Z. Zhang, *Optical Properties and Spectroscopy of Nanomaterials* (World Scientific Publishing, Singapore, 2009).

[7] H. Husu, B. K. Canfield, J. Laukkanen, B. Bai, M. Kuittinen, J. Turunen, and M. Kauranen, Metamaterials **2**, 155 (2008).

[8] S. A. Maier, *Plasmonics: Fundamentals and Applications* (Springer Science, NY, USA, 2007).

[9] V. K. Valev, Langmuir **28**, 15454 (2012).

[10] J. A. H. van Nieuwstadt, M. Sandtke, R. H. Harmsen, F. B. Segerink, J. C. Prangsma, S. Enoch, and L. Kuipers, Phys. Rev. Lett. **97**, 146102 (2006).

[11] B. K. Canfield, S. Kujala, K. Jefimovs, J. Turunen, and M. Kauranen, Opt. Express **12**, 5418 (2004).

[12] A. Boltasseva and V. M. Shalaev, Metamaterials **2**, 1 (2008).

[13] W. Cai, U. K. Chettiar, A. V. Kildishev, and V. M. Shalaev, Nat. Photonics **1,** 24 (2007).

[14] P. Biagioni, J. Huang, and B. Hecht, Rep. Prog. Phys. **75**, 024402 (2012).

[15] M. Gentile, M. Hentchel, R. Taubert, H. Guo, H. Giessen, and M. Fiebig, Appl. Phys. B **105,** 149 (2011).

[16] V. K. Valev, A. V. Silhanek, N. Smisdom, B. De Clercq, W. Gillijns, O. A. Aktsipetrov, M. Ameloot, V. V. Moshchalkov, and T. Verbiest , Opt. Express **18,** 8286 (2010).

[17] A. D. Mc Farland and R. P. Van Duyne, Nano Lett. **3**, 1057 (2003).

[18] N. Liu, M. L. Tang, M. Hentschel, H. Giessen, and A. P. Alivisatos, Nat. Mater. **10**, 631 (2011).

[19] J. B. Pendry, Phys. Rev. Lett. **85**, 3966 (2000).

[20] N. Yu, P. Genevet, M. A. Kats, F. Aieta, J. P. Tetienne, F. Capasso, and Z. Gaburro, Science **334**, 333 (2011).

[21] X. Ni, N. K. Emani, A. V. Kildishev, A. Boltasseva, and V. M. Shalaev, Science **335,** 427 (2012).

[22] T. Wang, P. Narayanan, M. Leuchtenburg, C. A. Moritz, C.A. Nanoelectronics Conference (2nd IEEE International), 2008, p. 989.

[23] E. Ozbay, Science **311**, 13 (2006).

[24] N. Srivastava and K. Banerjee, JOM **56**, 30 (2004).

[25] R. Zia, J. A. Schuller, A. Chandran, M. L. Brongersma, Materialstoday **9,** 20 (2006).

[26] V. M. Shalaev, Nat. Photonics **1**, 41 (2007).

[27] A. Lesuffleur, L. K. S. Kumar, and R. Gordon, Phys. Rev. B **75**, 045423 (2007).

[28] C. Hubert, L. Billot, P.-M. Adam, R. Bachelot, and P. Royer, Appl. Phys. Lett. **90**, 181105 (2007).

[29] B. K. Canfield, S. Kujala, M. Kauranen, K. Jefimovs, T. Vallius, and J. Turunen, Appl. Phys. Lett. **86**, 183109 (2005).

[30] M. Sukharev, J. Sung, K. G. Spears, and T. Seideman, Phys. Rev. B **76,** 184302 (2007).

[31] A. Shalabney, A. Lakhtakia, I. Abdulhalima, A. Lahav, Christian Patzig, I. Hazek, A. Karabchevsky, Bernd Rauschenbach, F. Zhang, and J.Xu: Photonics Nanostruct.: Fundam. Appl. **7** (2009) 176.

[32] A. D. Rakic, A. B. Djurišic, J. M. Elazar, and M. L. Majewski, Appl. Opt. **37**, 5271 (1998).

[33] D. Sarid and W. A. Challener, *Modern Introduction to Surface Plasmons Theory, Mathematica Modeling and Applications* (Cambridge University Press, New York, 2010).

[34] N. W. Ashcroft and N. D. Mermin, *Solid State Physics* (Cengage Learning, Orlando, US, 1976).

[35] D. Edwards: in *Handbook of Optical Constants of Solids*, ed. E. Palik (Academic Press, New York, 1985).

[36] L. Novotny and B. Hecht, *Principles of Nano-Optics* (Cambridge University Press, New York, 2006).

[37] J. R. Sambles, G. W. Bradbery, and F. Yang, Contemp. Phys. **32**, 173 (1991).

[38] M. Sukharev, J. Sung, K. G. Spears, and T. Seideman, Phys. Rev. B **76**, 184302 (2007).

[39] H. Husu, J. Mäkitalo, J. Laukkanen, M. Kuittinen, and M. Kauranen, Opt. Express **18**, 16601 (2010).

[40] D. Sinton, R. Gordon, and A. G. Brolo, Microfluid Nanofluid **4**, 107 (2008).

[41] O. Pluchery, R. Vayron, and K. M. Van, Eur. J. Phys. **32,** 585 (2011).

[42] R. D. Guenther, *Modem Optics* (John Wiley & Sons, USA, 1990).

[43] W. T. Silfvast, *Laser Fundamentals* (Cambridge University Press, New York, 2004).

[44] D. K. Gramotnev and S. Bozhevolnyi, Nat. Photonics **4,** 83 (2010).

[45] H. Tuovinen, M. Kauranenj, K. Jefimovs, P. Vahimaa, T. Vallius, J. Turunen. N. V. Tkachenko, and H. Lemmetyinen, Nonlinear Optic. Phys. Mat. **11,** 421 (2002).

[46] R. Czaplicki, M. Zdanowicz, K. Koskinen, J. Laukkanen, M. Kuittinen, and M. Kauranen, Opt. Express **19**, 26866 (2011).

[47] M. Gentile, M. Hentchel, R. Taubert, H. Guo, H. Giessen, and M. Fiebig, Appl. Phys B. **105**, 149 (2011).

[48] M. Zdanowicz, S. Kujala, H. Husu, and M. Kauranen, New J. Phys. **13**, 023025 (2011).

[49] M. Kauranen and A. V. Zayats, Nat. Photonics **6**, 737 (2012).

[50] V. K. Valev, X. Zheng, C. G. Biris, A. V. Silhanek, V. Volskiy, B. De Clercq, O. A. Aktsipetrov, M. Ameloot, N. C. Panoiu, G. A. E. Vandenbosch, and V. V. Moshchalkov, Opt. Mater. Express **1**, 36 (2011).

[51] H. Sano and G. Mizutani, e-J. Surf. Sci. Nanotechnol. **1**, 57 (2003).

[52] P. F. Brevet, *Surface Second Harmonic Generation* (Presses Polytechniques Universitaires Romandes, Lausanne, 1997).

[53] S. Kujala, B. K. Canfield, and M. Kauranen, Phys. Rev. Lett. **98,** 167403 (2007).

[54] B. Koopmans, A. M. Janner, H. A. Wierenga, Th. Rasing, G. A. Sawatzky, and F. van der Woude, Appl. Phys. A **60**, 103 (1995).

[55] G. Lupke, D. J. Bottomley, and H. M. van Driel, J. Opt. Soc. Am. B **11**, 33 (1994).

[56] F. J. Rodriguez, F. W. Wang, and M. Kauranen, Opt. Exp. **16**, 8704 (2008).

[57] R. L. Sutherland, *Handbook of Nonlinear Optics* (Marcel Dekker, New York, 2003) 2nd ed.

[58] R. W. Boyd, *Nonlinear Optics* (Academic Press, San Diego, 2003) 2nd ed.

[59] W. L. Mochán, J. A. Maytorena, Proceedings of the 33rd Course of the International School of Solid State Physics. EPIOPTICS-8, 2004, p.17.

[60] A. G. Lambert, P. B. Davies, and D. J. Neivandt, Appl. Spectrosc. Rev. **40,** 103 (2005).

[61] J. Butet, K. Thyagarajan, and O. J. F. Martin, Nano Lett. **13**, 1787 (2013).

[62] B. Koopmans, A. M. Janner, H. A. Wierenga, T. Rasing, G. A. Sawatzky, and F. van der Woude, Appl. Phys. A **60**, 103 (1995).

[63] Y. R. Shen, Appl. Phys. B **68**, 295 (1999).

[64] F. X. Wang, F. J. Rodríguez, W. M. Albers, R. Ahorinta, J. E. Sipe, and M. Kauranen Phys. Rev. B **80**, 233402 (2009).

[65] G. Bachelier, J. Butet, I. Russier-Antoine, C. Jonin, E. Benichou, and P.-F. Brevet Phys. Rev. B **82**, 235403 (2010).

[66] R. Zhou, H. Lu, X. Liu, Y. Gong, and D. Mao, J. Opt. Soc. Am. B **27,** 2405 (2010).

[67] J. J. H. Gielis, P. M. Gevers, I. M. P. Aarts, M. C. M. van de Sanden, and W. M. M. Kessels, J. Vac. Sci. Technol. A **26**, 1519 (2008).

[68] M. B. Feller, W. Chen, and Y. R. Shen, Phys. Rev. A **43,** 6778 (1991).

[69] H. L. Dai and W. Ho, *Laser Spectroscopy and Photochemistry on Metal Surfaces*, Part 1 (World Scientific Pub Co Inc, Singapore, 1995).

[70] T. J. Sono, J. G. Scott, C. L. Sones, C. E. Valdivia, S. Mailis, and R. W. Eason, Phys. Rev. B **74**, 205424 (2006).

[71] P. Spitzer, C. Zierhofer, and E. Hochmair, Biomed. Eng. Online **5**, 13 (2006).

[72] J. J. H. Gielis, P. M. Gevers, I. M. P. Aarts, M. C. M. van de Sanden, and W. M. M. Kessels, J. Vac. Sci. Technol. A **26**, 1519 (2008).

[73] R. J. Pressley, *Handbook of Lasers* (Chemical Rubber Co., Cleveland, 1971).

[74] F. Capolino, *Applications of Metamaterials* (CRC Press, USA, 2009).

[75] I. Utke, S. Moshkalev, and P. Russell, *Nanofabrication Using Focused Ion and Electron Beams: Principles and Applications* (Oxford University Press, New York, 2012).

[76] A. Dąbrowski, *Applications in Industry*, Volume I (Elsevier Science, Netherland, 1999).

[77] A. M. Baró and R. G. Reifenberger, *Atomic Force Microscopy in Liquid: Biological Applications* (Wiley-VCH, Germany, 2012).

[78] J. C. Vickerman and I. Gilmore, *Surface Analysis: The Principal Techniques* (John Wiley & Sons Ltd, UK, 2009).

[79] http://www.doitpoms.ac.uk/tlplib/afm/modes_operation.php.

[80] W. Zhou, M. Dridi, J. Y. Suh, C. H. Kim, D. T. Co, M. R. Wasielewski, G. C. Schatz, and T. W. Odom, Nat. Nanotechnol. **8**, 506 (2013).

[81] J. Stadler, B. Oswald, T. Schmida, and R. Zenobi, J. Raman Spectrosc. **44**, 227 (2013).

[82] J. M. Klingsporn, M. D. Sonntag, T. Seideman, and R. P. Van Duyne, J. Phys. Chem. Lett. **5**, 106 (2014).

[83] B. K. Canfield, S. Kujala, K. Jefimovs, T. Vallius, J. Turunen, and M. Kauranen, J. Opt. A **7**, S110 (2005).

[84] M. Airola, Y. Liu, and S. Blair, J. Opt. A, S118 (2005).

[85] A. Lesuffleur, L. K. S. Kumar, and R. Gordon, Appl. Phys. Lett. **88**, 261104 (2006).

[86] F. Eftekhari and R. Gordon, IEEE J. Sel. Top. Quantum Electron. **14**, 1552 (2008).

[87] R. Zhou, H. Lu, X. Liu, Y. Gong, and D. Mao, J. Opt. Soc. Am. B 27, 2405 (2010).

[88] M. Zdanowicz, S. Kujala, and H. Husu, New J. Phys. **13**, 023025 (2011).

[89] R.Czaplicki, M. Zdanowicz, K. Koskinen, J. Laukkanen, M. Kuittinen, and M. Kauranen: Opt. Express **19**, 26866 (2011).

[90] M. D. R. Lide, *CRC Handbook of Chemistry and Physics*, (CRC Press, 2010).

[91] M. Wakaki, K. Kudo, and T. Shibuya, *Physical Properties and Data of Optical Materials*, (CRC Press, 2007).

[92] M. Omote, H. Kitaoka, E. Kobayashi, O. Suzuki, K. Aratake, H. Sano, G. Mizutani, W. Wolf, and R. Podloucky, J. Phys.: Condens. Matter **17**, S175 (2005).

[93] P. Guyot-Sionnest, W. Chen, and Y. R. Shen, Phys. Rev. B **33**, 8254 (1986).

[94] O. Wälder, *Mathematical Methods for Engineers and Geoscientists* (Springer, Berlin/Heidelberg, 2008).

[95] D. P. Fromm, A. Sundaramurthy, P. J. Schuck, G. Kino, and W. E. Moerner, Nano Lett. **4**, 957 (2004).

[96] T. Kitahara, A. Sugawara, H. Sano, and G. Mizutani, Appl. Surf. Sci. **219**, 271 (2003).

[97] B. K. Canfield, S. Kujala, K. Jefimovs, Y. Svirko, J. Turunen, and M. Kauranen, J. Opt. A **8**, S278 (2006).

[98] E. Kobayashi, G. Mizutani, and S. Ushioda, Jpn. J. Appl. Phys. **36**, 7250 (1997).

[99] S. F. A. Kettle, Spectrochim. Acta, Part A **54**, 1639 (1998).

[100] K. G. Lee, K. J. Ahn, H. W. Kihm, J. S. Ahn, T. K. Kim, S. Hong, Z. H. Kim, and D. S. Kim, Opt. Express **16**, 10641 (2008).

[101] A. Kudelski, Vib. Spectrosc. **39**, 200 (2005).

[102] B. K. Canfield, S. Kujala, K. Jefimovs, Y. Svirko, J. Turunen, and M. Kauranen, J. Opt. A **8**, S278 (2006).

[103] N. Meinzer, M. Wegener, M. F. G. Klein, P.-J. Jakobs, H. Hein, M. Konig, J. Niegemann, K. Busch, N. Feth, and S. Linden, Conference on Quantum Electronics and Laser Science. CLEO/QELS, 2008, p. 1.

[104] M. F. G. Klein, H. Hein, P.-J. Jakobs, S. Linden, N. Meinzer, M. Wegener, V. Saile, and M. Kohl, Microelectron. Eng. **86**, 1078 (2009).

[105] N. A. Tuan and G. Mizutani, e-J. Surf. Sci. Nanotechnol. **7**, 831 (2009).

[106] Prof. M. Koyano (private communication).

[107] A. Dähn, W. Hübner, and K.H. Bennemann, Phys. Rev. Lett. **77**, 3929, 1996.

[108] M. Trzeciecki, Dähn, W. Hübner, Phys. Rev. B. **60**, 1144, 1999.

[109] S. Kujala, B. K. Canfield, and M. Kauranen, Phys. Rev. Lett. **98**, 167403 (2007).

[110] N. K. Quang, Y. Miyauchi, G. Mizutani, M. D. Charlton, R. Chen, S. Boden, and H. Rutt, Jpn. J. Appl. Phys. **53**, 02BC11 (2014).

[111] J. E. Sipe, D. J. Moss, and H. M. van Driel, Phys. Rev. B **35**, 1129 (1987).

[112] M. Wakaki, K. Kudo, T. Shibuya, *Physical Properties and Data of Optical Materials*, (CRC Press, 2007).